Glacier dynamics, ice mass unloading and bedrock response in the southern Antarctic Peninsula

by

Chen Zhao

Grad. Dip. Mar. Sci., B.Eng., M.Sci.

School of Technology, Environments and Design

University of Tasmania

Submitted in fulfilment of the requirements for the degree of Doctor of Philosophy

Sep 2018

UNIVERSITY *of* TASMANIA

Abstract

Rapid regional warming in the Antarctic Peninsula led to significant retreat and eventual collapse of several major ice shelves since the 1970s, followed by the subsequent acceleration and thinning of their feeding glaciers. The Wordie Ice Shelf, lying off the west coast of the southern Antarctic Peninsula, has undergone long-term disintegration since the 1960s with a substantial calving event occurring around 1989, followed by continuous steady retreat and its almost-complete disappearance by 2008. The dynamic response of the upstream glaciers to the ice shelf collapse and the response of the solid Earth to the associated mass loss are not fully understood.

To quantify the mass loss from the catchment region of the Wordie Ice Shelf, a digital elevation model (DEM) was generated using airborne vertical and oblique imagery from 1966 and compared to a DEM derived from 2008 SPOT satellite data. This analysis reveals lowering over that time of approximately 60 m at the front of Fleming Glacier, the major glacier feeding the former ice shelf. Using IceBridge and ICESat-1/GLAS data spanning 2002-2014, the mean elevation change rate was estimated. The rates post-2008 (-6.25 ± 0.20 m yr^{-1}) were more than twice those of 2002-2008 (-2.77 ± 0.89 m yr^{-1}) near the ice front. These data quantify the change in mass load that is subsequently used as a basis for the simulation of viscoelastic solid Earth deformation.

To infer properties of Earth rheology, modelled elastic deformation rates, and a suite of modelled viscous rates, were subtracted from GPS-derived three-dimensional bedrock velocities at GPS sites to the south of Fleming Glacier. Assuming the pre-breakup bedrock uplift was positive due to post-Last Glacial Maximum (LGM) ice retreat, the derived viscoelastic-corrected GPS uplift rates suggest upper mantle viscosities are $> 2 \times 10^{19}$ Pa s and likely $> 1 \times 10^{20}$ Pa s in this region, 1-2 orders of magnitude greater than previously found ~500 km further north in the Antarctic Peninsula. After the application of elastic and plate-tectonic corrections, horizontal bedrock velocities at the GPS site nearest the Fleming Glacier, point away from Marguerite Bay rather than away from the present glacier front. This suggests that horizontal bedrock motion in the region reflects the earlier retreat of the glacier system following the LGM, compatible with a relatively strong mantle in this region. These findings highlight the need for improved understanding of ice load changes in this region through the late Holocene in order to accurately model present-day glacial isostatic adjustment.

The observed thinning of Fleming Glacier over five decades represents an opportunity to further understand glacier responses to ice shelf disintegration. Understanding of the dynamics of fast-flowing glaciers such as the Fleming Glacier, and their potential future behavior, can be improved through ice sheet modelling studies. Here, the Stokes model Elmer/Ice was used to simulate the Wordie Ice Shelf-Fleming Glacier system.

Inverse methods are commonly used in ice sheet models to infer the spatial distribution of a basal friction coefficient, which has a large effect on the basal velocity and ice deformation. Using an inverse method in Elmer/Ice, the basal friction coefficients were inferred from the surface velocities observed in 2008. A multi-cycle spin-up scheme was developed to reduce the influence of initial temperature assumptions on the final inversion. This is particularly important for glaciers like the Fleming Glacier, which have areas of strongly temperature-dependent, deformational flow in the fast-flowing regions. Sensitivity tests using various bed elevation datasets, ice front positions and boundary conditions demonstrate the importance of high-accuracy ice thickness/bed geometry data and precise location of the ice front boundary.

Recent observational studies have suggested the 2008-2015 velocity change and the dynamic thinning of the Fleming system was due to the ungrounding of the Fleming Glacier front. It is important to know whether the substantial additional speed-up and surface draw-down of the glacier since 2008 is a direct response to increasing ocean forcing or driven by the feedback within the grounded glacier system or a combination of both. To explore the mechanism underlying the changes, the Elmer/Ice model was used to simulate the basal shear stress of the Fleming system in 2008 and 2015. High-resolution modelling reveals that the ungrounding process of the Fleming Glacier might not have started in Jan 2008, which is consistent with a height above buoyancy calculation for 2008. Comparison of the inversions for basal shear stresses for 2008 and 2015 suggests upstream migration of the grounding line by ~9 km by 2015, while the 2008 ice front/grounding line positions virtually coincided with the 1996 grounding line position. This shift is consistent with the change in floating area deduced from the height above buoyancy in 2015. The retrograde bed underneath the Fleming Glacier has likely promoted the significant migration of its grounding line. The increase in basal sliding and grounding line retreat might be caused by increased subglacial water volume and/or pressure through greater frictional heating at the bed further upstream in the fast-flowing region as a result of acceleration. Improved knowledge of bed topography near the grounding line and further transient simulations with oceanic forcing are required to predict accurately the future movement of the Fleming system grounding line and better understand its ice dynamics and contribution of freshwater flux into the ocean.

The Fleming system now represents one of the best observed examples of multi-decadal glacier change following ice shelf disintegration; combination of various observational datasets (including those presented here) with the new Stokes model provides a much-improved capability to understand the future of this glacier system.

Declaration of Originality

This thesis contains no material, which has been accepted for a degree or diploma by the University or any other institution, except by way of background information and duly acknowledged in the thesis, and to the best of my knowledge and belief no material previously published or written by another person except where due acknowledgement is made in the text of the thesis, nor does the thesis contain any material that infringes copyright.

Signed: _____

Chen Zhao

Date: Sep 07, 2018

Acknowledgements

First and foremost, I would love to express my sincerest thanks to my supervisor team, Matt A. King, Rupert M. Gladstone, Roland C. Warner, and Christopher S. Watson for their continued support and critical review. The completion of this thesis would not have been possible without their help. Each of them has provided me with considerable time and attention. Without their guidance, patience, ideas and advice, this thesis would not have been completed. I appreciate their differences in their approach to research and writing. They have provided me with well-rounded feedback, which greatly balanced my manuscripts and thesis, in addition to expanding my perspective on how to approach research.

This research was supported by the School of Technology, Environments and Design (STED), University of Tasmania (UTAS), and the Australian Antarctic Division through the Australian Postgraduate Awards (APA) for the first two years, the Research Training Program (RTP) for the rest of the time, and AAD-UTAS PhD program in Quantitative Antarctic Science (QAS). I would like to thank the STED of UTAS for managing my candidature and with the financial travel support they have provided me. I would also like to thank my PhD graduate research coordinators, Lorne Kriwoen and Arko Lucieer, for coordinating my PhD project, which helped me make progress as planned.

Thanks to the Chair of Examiners, Professor James Kirkpatrick, and two examiners, Dr. Stephen Price and Dr. Roderik Van der Wal, for their very helpful comments and suggestions on my thesis.

Thanks to the ACE CRC and IMAS Ice Sheet group for their kind help, suggestions, and support during the PhD. Special thanks to Prof. Ian Allison for helping me to write a review article (not included in this thesis) about the Chinese-Australian cooperation in Antarctic Research over the past forty years. The publication of this article opened my mind as a Chinese glaciologist and encouraged me to devote myself to contributing to the future cooperation between both countries.

Thanks to Quark Expeditions and the Quark Team for providing me with valuable chances to visit both the Antarctic and Arctic as a glaciologist, a mandarin guide, and a Zodiac driver. The experiences working with wonderful people from around the world opened my mind to this amazing planet, guided me to feel the nature from deep heart, and inspired me to keep challenging the impossible.

The thesis would not be possible without the support from my friends from China and Australia. Thanks to all my close friends in China: Jixin, Dr. Jing Kang, Fangzhou, Fanfan, Yuanyuan, Huiyong. Thanks to the forever 8 group: Shuai Ge, Shi Fu, Zhu, Huan, Meng, Duo, and Bing Gege. Thanks to the IMAS lunch group (Jiale, Luwei, Tze) for keeping me company during the lunchtime of each working day. Thanks to the Tasmanian Chinese Art and Communication Society (special thanks to Youyou Pan and Ziqing Yuan), the Tasmanian Chinese School (special thanks to Kim Phong) and all my friends in Hobart for creating such a colorful and meaningful life in

Tasmania for me. It’s hard to name all of you here but your big smiles are all captured on the wall of our house.

Special thanks to this beautiful and peaceful place, Tasmania, for pointing me to my love and showing me what a beautiful life could be.

Last but not the least, I would like to thank all my family: my husband (Fan Hu), my parents, my grandparents, my mother in law, my little brother, my nieces (Anan and Xuanxuan), my uncles and aunts, my cousins (special thanks to Jingjing) for their love and spiritual support throughout this long but enjoyable PhD period. I love you all forever!

Statement of Co-Authorship

The following people and institutions contributed to the publication of work undertaken as part of this thesis:

Chen Zhao (Candidate)

School of Technology, Environments and Design, University of Tasmania

Matt A. King (Primary Supervisor)

School of Technology, Environments and Design, University of Tasmania

Rupert G. Gladstone (Supervisor)

Arctic Centre, University of Lapland

Roland C. Warner (Supervisor)

Antarctic Climate & Ecosystems Cooperative Research Centre, University of Tasmania

Christopher S. Watson (Supervisor)

School of Technology, Environments and Design, University of Tasmania

Thomas Zwinger (Co-author)

CSC-IT Center for Science Ltd.

Valentina R. Barletta (Co-author)

DTU Space, Technical University of Denmark

Andrea Bordoni (Co-author)

DTU Compute, Technical University of Denmark

Matthew Dell (Co-author)

School of Technology, Environments and Design, University of Tasmania

Pippa L. Whitehouse (Co-author)

Department of Geography, Durham University

Mathieu Morlighem (Co-author)

Department of Earth System Science, University of California Irvine

Paper 1, Rapid ice unloading in the Fleming Glacier region, southern Antarctic Peninsula, and its effect on bedrock uplift rates

Zhao (70%), King (12%), Watson (8%), Barletta (3%), Bordoni (3%), Dell (2%), Whitehouse (2%)

Zhao and King collected and processed the datasets together. Zhao ran the solid Earth model and drafted the paper. All authors contributed to the refinement of the experiments, the interpretation of the results and the final manuscript.

Paper 2, Basal friction of Fleming Glacier, Antarctica – Part 1: Sensitivity of inversion to temperature and bedrock uncertainty

Zhao (70%), Gladstone (15%), Warner (7%), King (3%), Zwinger (3%), Morlighem (2%)

Zhao and Gladstone set up the model and designed the experiments together with Warner. Zhao collected the datasets, ran the simulations, and drafted the paper. All authors contributed to the refinement of the experiments, the interpretation of the results and the final manuscript. Morlighem generated the bedrock data.

Paper 3, Basal friction of Fleming Glacier, Antarctica – Part 2: Evolution from 2008 to 2015

Zhao (70%), Gladstone (15%), Warner (7%), King (3%), Zwinger (3%), Morlighem (2%)

Zhao and Gladstone set up the model and designed the experiments together with Warner. Zhao collected the datasets, ran the simulation, and drafted the paper. All authors contributed to the refinement of the experiments, the interpretation of the results and the final manuscript.

We the undersigned agree with the above stated "proportion of work undertaken" for each of the above published peer-reviewed manuscripts contributing to this thesis:

Signed:

Signed:_____

Professor Matt A. King

Supervisor

School of Technology, Environments and Design

University of Tasmania

Date: Sep 03, 2018

Authority of Access

The publishers of the papers comprising Chapters 2, 3 and 4 hold the copyright for that content, and access to the material should be sought from the respective journals:

The Chapter 2 is an edited version published by © 2017 Elsevier B.V. Reprinted with permission from Zhao, C., King, M. A., Watson, C. S., Barletta, V. R., Bordoni, A., Dell, M., and Whitehouse, P. L. (2017), Rapid ice unloading in the Fleming Glacier region, southern Antarctic Peninsula, and its effect on bedrock uplift rates, in *Earth and Planetary Science Letters*, 473, 164-176.

The Chapter 3 is an edited version published by © 2018 The Cryosphere. Reprinted with permission from Zhao, C., Gladstone, R. M., Warner, R. C., King, M. A., Zwinger, T., and Morlighem, M. (2018): Basal friction of Fleming Glacier, Antarctica - Part 1: Sensitivity of inversion to temperature and bedrock uncertainty, *The Cryosphere*, 12, 2637-2652, https://doi.org/10.5194/tc-12-2637-2018, 2018.

The Chapter 4 is an edited version published by © 2018 The Cryosphere. Reprinted with permission from Zhao, C., Gladstone, R. M., Warner, R. C., King, M. A., Zwinger, T. and Morlighem, M. (2018): Basal friction of Fleming Glacier, Antarctica - Part 2: Evolution from 2008 to 2015, *The Cryosphere*, 12, 2653-2666, https://doi.org/10.5194/tc-12-2653-2018, 2018.

Appendices A-C contain the supplementary materials for each of the corresponding papers.

The remaining non-published content of the thesis may be made available for loan and limited copying and communication in accordance with the Copyright Act 1968.

Signed: _____

Chen Zhao

Date: Sep 07, 2018

Content

Chapter 1

Introduction

Chapter 1 presents general background information on the rapid climate change in Antarctic Peninsula, significant changes to the ice shelves and their feeding glaciers, the Solid Earth response to ice unloading and introduces the research area – the Wordie Ice Shelf – Fleming Glacier (WIS-FG) system.

Rapid regional climate change has caused several ice shelves on the Antarctic Peninsula (AP) to retreat and collapse in the past several decades. As a response, the glaciers feeding them have accelerated and thinned, and this ice mass unloading has induced a solid Earth uplift, which is observed in GPS records. The Wordie Ice Shelf (WIS) on the west coast of the southern AP has been observed to retreat since the 1960s and the majority of the ice shelf has been lost. The Fleming Glacier (FG), as its main feeding glacier, has shown rapid acceleration and increased dynamic thinning in recent decades. This thesis combines a numerical glacier model and glacial isostatic adjustment (GIA) models with remote sensing observations to improve estimates of the mass loss from the feeding glaciers, the solid Earth response to this mass loss, and the mechanisms that drives the substantial acceleration and surface thinning.

1.1 Rapid climate change in the Antarctic Peninsula

The Antarctic Ice Sheet has experienced increasing mass loss over the past two decades (Shepherd et al. 2012, Sutterley et al. 2014, Harig and Simons 2015, Martín-Español et al. 2016a, Gardner et al. 2018). The largest ice discharge occurred in the Amundsen and Bellingshausen seas and the southern AP (Fig. 1.1) following ice shelf retreat and collapse (Harig and Simons 2015, Wouters et al. 2015, Gardner et al. 2017), as a response to both atmospheric and oceanic warming and the influence of significant circulation changes in these two systems (Carrasco 2013, Li et al. 2014, Cook et al. 2016, Turner et al. 2016).

Globally, over the second half of the 20th Century, the largest increases in surface air temperature were reported in the AP and especially on its west coast (Turner et al. 2005, Carrasco 2013). Station records on the western AP include a large regional warming between 1951 and 2000, with the largest increase in annual mean surface air temperature of 2.8 ℃ occurring at Vernadsky/Faraday Station, followed by a decreased warming trend or even slight cooling from 2001 to 2010 (Carrasco 2013, Turner et al. 2016). The decadal reversal of the warming process in the first part of the 21st century is thought to be due to extreme natural internal variability in regional atmospheric circulation, rather than a change in global temperature trend (Turner et al. 2016).

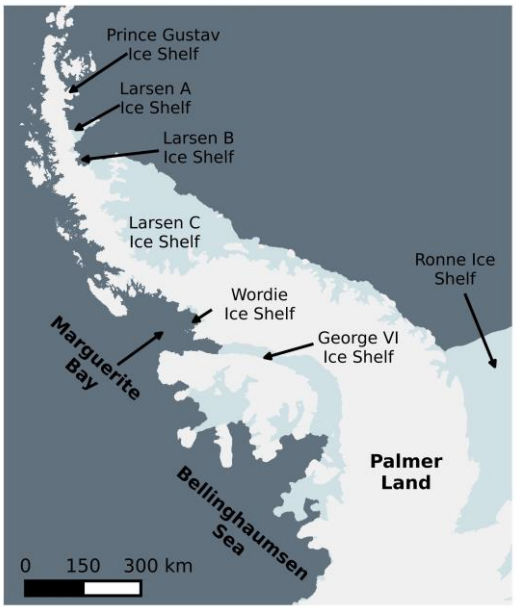

Figure 1.1 Locations of Antarctic Peninsula, Weddell Sea, Bellingshausen Sea, Palmer Land, Marguerite Bay, and some ice shelves. Wordie Ice Shelf is located on the western Antarctic Peninsula.

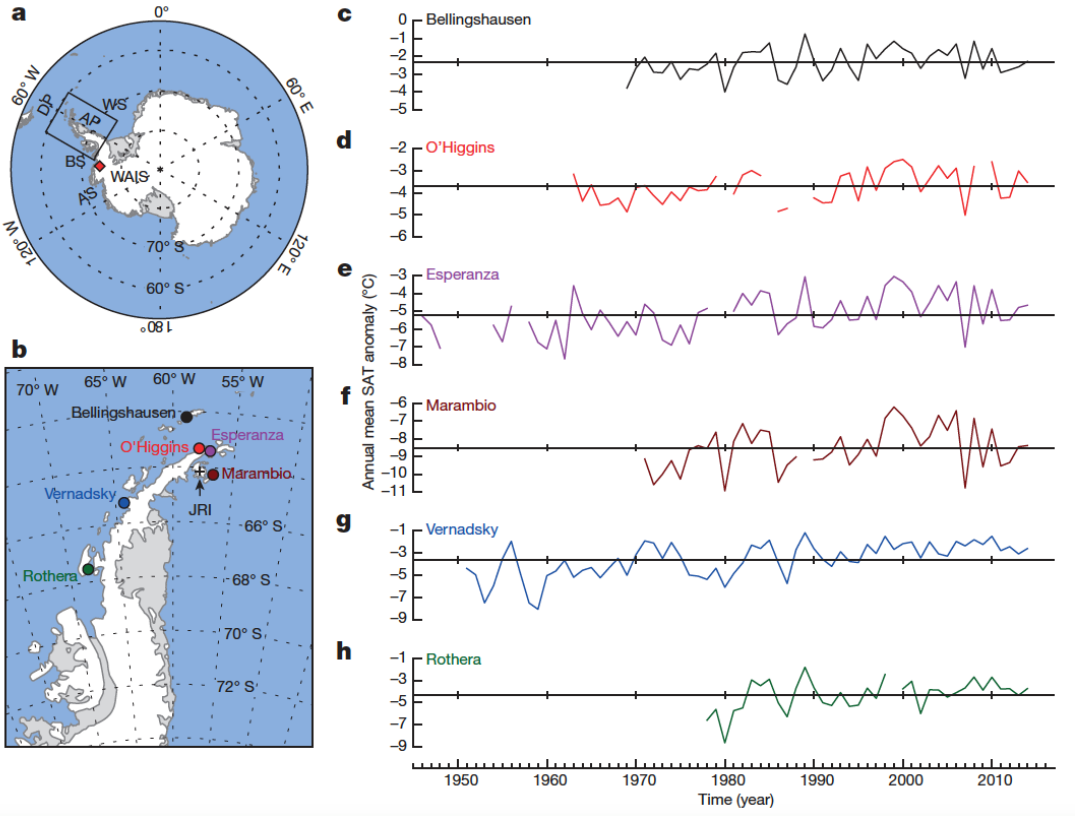

Figure 1.2 Surface air temperature changes at six Antarctic Peninsula (AP) stations with map of the Antarctic (a) and the AP showing the locations of stations (b). c–h, the time series of annual mean surface air temperature anomalies are shown for Bellingshausen (c), O'Higgins (d), Esperanza (e), Marambio (f), Vernadsky (g) and Rothera (h), with each horizontal line indicating the mean temperature for the whole time series. Reproduced from Turner et al. (2016).

The WIS is located further south than the Vernadsky/Faraday Station, in a region where no long-term temperature records exist (Fig 1.2). The major WIS break-up occurred in the last half-century and was likely triggered by one or more of surface melting due to rising air temperatures (Doake and Vaughan 1991b), enhanced tidal action as a result of relaxed sea-ice conditions in Marguerite Bay (Reynolds 1988) and the ocean-warming driven sub-shelf melting in Wordie Bay (Holland et al. 2010, Pritchard et al. 2012, Depoorter et al. 2013, Walker and Gardner 2017).

Coincident oceanographic changes have occurred over the continental shelf in the adjacent Bellingshausen and Amundsen seas (Fig. 1.3), with coastal ocean warming of 0.1-0.3 ℃ decade^{-1} since the 1990s (Schmidtko et al. 2014). This warming is associated with a shoaling of the mid-depth temperature maximum over the continental slope and shelf, which allows intrusions of warmer and saltier Circumpolar Deep Water (CDW) into the continental shelf. In the eastern AP, a warming trend has also been observed in intermediate and deep water in the Weddell Sea (Fig. 1.1) with a rate of ~0.012±0.007 ℃ yr^{-1} from the 1970s to 1990s (Robertson et al. 2002). Coincident with the ocean warming in the western AP is a reduction in sea ice extent on the western side of the AP (Stammerjohn et al. 2008). Little is known about ocean-temperature change in the period before 1960s in the southern AP.

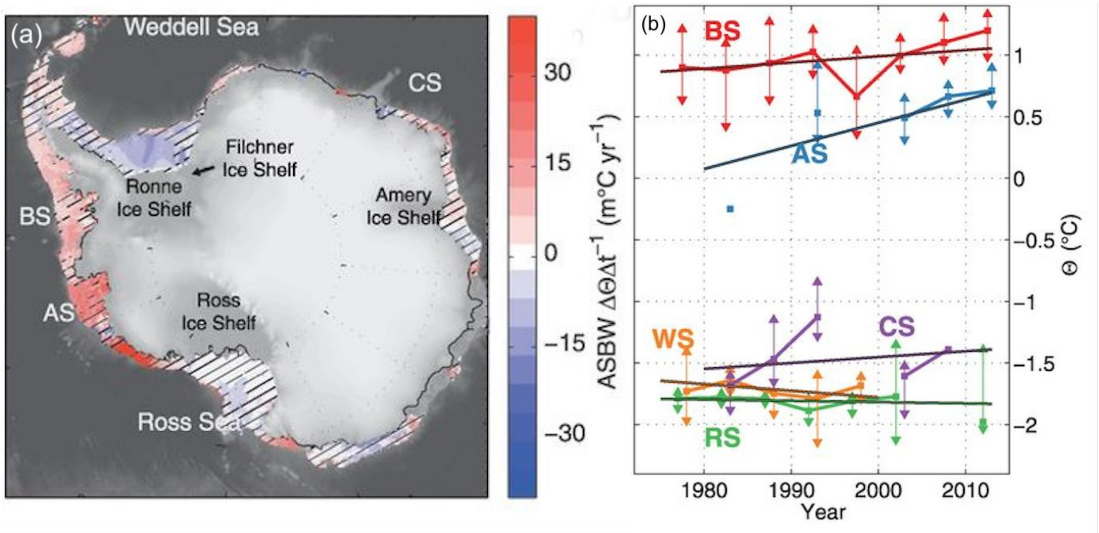

Figure 1.3 (a) Conservative temperature linear trends at the seabed for the period 1975 to 2012 (b) Multiannual variability as shown by 5-year median properties since 1975. Abbreviations for surrounding seas: BS, Bellingshausen Sea; AS, Amundsen Sea; CS, Cosmonaut Sea; WS, Weddell Sea (excluding the Antarctic Peninsula). Reproduced from Schmidtko et al. (2014).

Additionally, a medium depth ice core drilled on Gomez Plateau in the south-western AP during 2007 revealed a doubling of snow accumulation since the 1850s, accelerating from a decadal average of 0.49 m yr^{-1} in 1855-1864 to 1.10 m yr^{-1} (water equivalent metres per year) in 1997-2006 (Thomas et al. 2008). Recent positive trends in the Southern Annular Mode since 1957 and the resultant increasing westerlies are

argued as the principal factor governing the decadal variability of accumulation at this ice core site (Thomas et al. 2008).

Rapid climate change in the AP has had a remarkable influence on the ice shelves, their feeding glaciers, and consequently solid Earth dynamics, which is further discussed in Sec. 1.2 and 1.3.

1.2 Significant retreat, thinning and collapse of ice shelves

These dramatic changes in climate have likely led to the observed rapid thinning and eventual retreat and collapse of ice shelves surrounding the AP (Liu et al. 2015, Paolo et al. 2015). Most of the ice shelves in the AP have shown significant retreat and collapse over the second half of the 20th century, leading to an overall reduction in total ice-shelf area of over 28,000 km^2 (Cook and Vaughan 2010). Of the twelve ice shelves in this region, Larsen B, Muller, and Wilkins have shown dramatic retreat (less than 70% of the original ice shelf area remains, where "original area" means the earliest available area observation), and Jones, Wordie, Prince Gustav, Larsen A have totally disintegrated (10% or less of the original area remains) within the last half-century. Four of the ice shelves (George VI, Bach, Stange, and Larsen D) have not shown a steady retreat (more than 90% of their original area remaining), while Larsen D is the only ice shelf to have shown an overall advance over the time period. Large sections of the Larsen A (Rott et al. 1996), Larsen B, (Rack and Rott 2004), Wilkins (Scambos et al. 2009), and Larsen C (Hogg and Gudmundsson 2017b) ice shelves, calved in 1995, 2002, 2008, 2017, respectively, while the calving of Larsen C was likely a natural process and thus not necessarily indicative of changing climate conditions (Hogg and Gudmundsson 2017b).

Rapid ice shelf thinning has also been observed in the AP even where ice shelves have not substantially retreated or disintegrated (to date). According to the record of ice-shelf thickness around the whole Antarctic continent from 1994 to 2012, the average ice-shelf volume change for the whole Antarctic has accelerated from a small loss (25 ± 64 km^3 yr^{-1}) for 1994-2003 to rapid loss (310 ± 74 km^3 yr^{-1}) for 2003-2012 (Paolo et al. 2015). The largest regional ice shelf thinning over the eighteen years occurred in the Amundsen and Bellingshausen seas (Fig. 1.4), with average (and maximum) thinning rates of 19.4 ± 1.9 (66.5 ± 9.0) m/decade and 7.4 ± 0.9 (64.4 ± 4.9) m/decade, respectively, and the regional ice-shelf thinning rate on the western AP is about twice that on the eastern side (3.8 ± 1.1 m/decade) (Paolo et al. 2015). Fricker and Padman (2012) also found that from 1978 to 2008 six major AP ice shelves (Wilkins, George VI, Bach, Stange, Larsen B, Larsen C and Larsen D) thinned with rates between 0.03 and 0.16 m yr^{-1}, while the strongest negative elevation change occurred on most ice shelves over the period of 1992-1995. Sustained thinning of ice shelves will eventually result in ice-shelf collapse and grounding-line retreat, which could further increase the grounded ice discharge and sea level rise.

Most ice shelf thinning or disintegration is seen as a direct response to the rapid climate changes as described in Sec. 1.1 (Paolo et al. 2015), although some changes

are part of repeated internally-driven cycles of growth and decay, as the Larsen-C calving events likely are (Hogg and Gudmundsson 2017b). In addition, the timing and pattern of retreat/collapse is not only affected by the change of climate (atmospheric and oceanic forcing and sea-ice extent), but also by the ice shelf configuration (e.g., ice shelf geometry, pinning points and regions of compressive flow) and conditions of mass balance (e.g., ice surface melting and texture, ice thickness, ice velocity and the ocean-driven basal melting), although it is not always clear exactly which processes dominate in each case or why (Cook and Vaughan 2010, Fricker and Padman 2012).

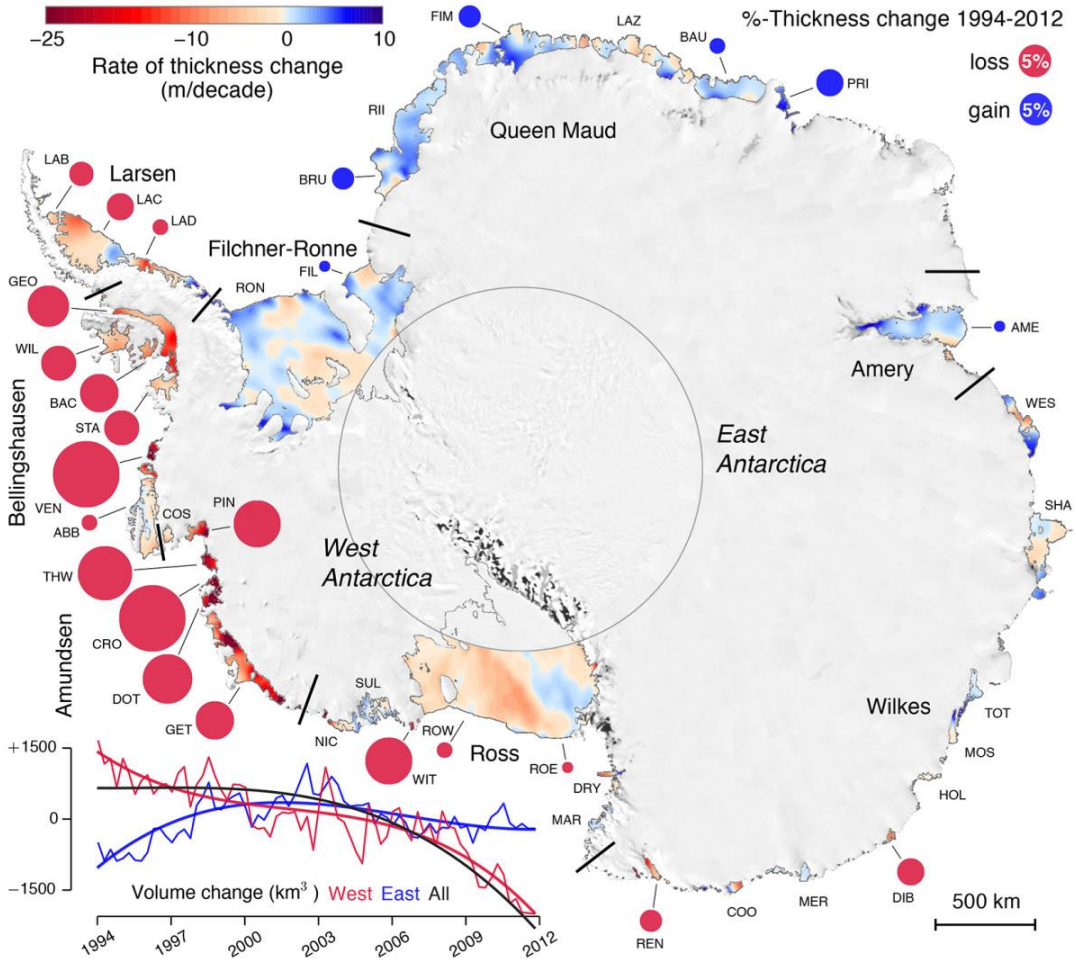

Figure 1.4 Average ice thickness and volume changes of Antarctic ice shelves from 1994 to 2012 (see Paolo et al. (2015)).

1.3 Dynamic ice thinning, glacier acceleration and grounding line retreat

Floating ice shelves exert a significant “buttressing” effect on their upstream feeding glaciers and regulate the flow of grounded ice (Furst et al. 2016, Reese et al. 2017). The retreat or collapse of floating ice shelves reduces the restraining effect on their feeding glaciers, which results in acceleration, dynamic thinning, and contributes to sea level rise (Scambos et al. 2004, Pritchard et al. 2009, Wouters et al. 2015, Gardner et al. 2017). The quantified impacts of ice shelf buttressing in Antarctica implies that the further retreat of current ice shelves in the Bellingshausen and Amundsen seas

will trigger important dynamic changes, compared with East Antarctica (Furst et al. 2016).

Ice mass loss from the Antarctic Ice Sheet has contributed 7.6±3.9 mm to the increase in global sea level between 1992 and 2017 (Shepherd et al. 2018), with substantial ice mass loss from the WAIS and the AP, with the East Antarctic Ice Sheet (EAIS) either near balance or growing somewhat (Harig and Simons 2015, Wouters et al. 2015, Gardner et al. 2017, Shepherd et al. 2018). Widespread ice losses along the Bellingshausen and Amundsen seas and in the AP have significantly increased in the past few decades (Rignot et al. 2008, Gardner et al. 2018). In the past six decades, the main 16 glaciers in the northern AP have lost ice at an annual rate of 0.24±0.08 m yr^{-1} (water equivalent metres per year) (Fieber et al. 2017). For the southern AP (including the Palmer Land and the Bellingshausen Coast), the rate of ice mass loss accelerated from near balance during 2003-2009 to a rate of -56±8 Gt yr^{-1} from 2010 to 2014 (Wouters et al. 2015). It is expected that tidewater glaciers and ice shelf tributary glaciers in the AP will continue to lose mass over the following century, with Schannwell et al. (2016) projecting a possible small contribution to sea level rise of 0.028-0.032±0.016 m by 2300.

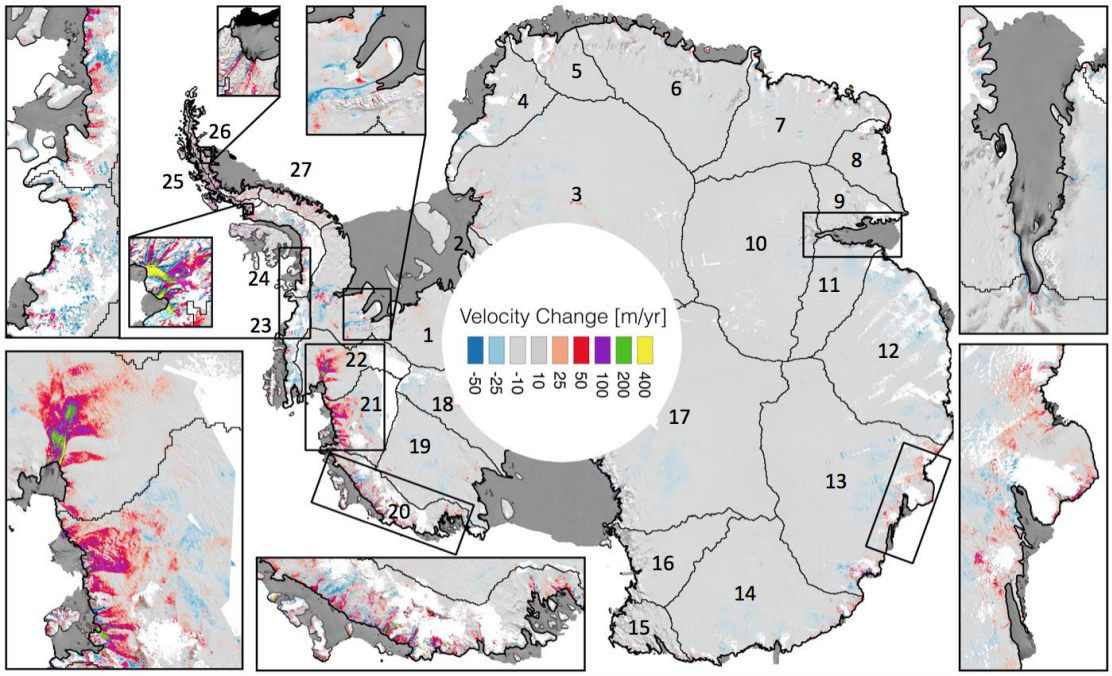

Figure 1.5 Change in surface velocities from 2008 to 2015 (2015 minus 2008). Reproduced from Gardner et al. (2018).

Grounded ice mass loss in the WAIS and the AP is largely dynamic, driven by increased ice discharge across the grounding line. Ice discharge from the whole of Antarctica increased from 1897±41 Gt yr^{-1} in 2008 to 1932±38 Gt yr^{-1} in 2015, with a 79% increase occurring overall in glaciers in the Amundsen Sea sector and another 11% from WIS-FG system flowing into Marguerite Bay located in the western AP (Gardner et al. 2017). This is coincident with the surface acceleration pattern during this period (Fig. 1.5). In western Palmer Land, most of the outlet glaciers have

accelerated by 0.2 to 0.3 m d^{-1} over 1992 to 2015, equivalent to a 13% increase in ice flow and a 15 km^3 yr^{-1} increase in ice discharge across the grounding line (Hogg et al. 2017a).

Consistent with this surface acceleration, the pattern of surface elevation changes of the Antarctic glaciers shows that an accelerated rate of dynamic thinning has occurred at the grounding zones of the Amundsen Sea Embayment and the AP (Pritchard et al. 2009). For the northern AP, the mean ice elevation change from 2003 to 2008 is -0.33 m yr^{-1} on the western side while for the eastern side the change averages to -1.48 m yr^{-1} (Scambos et al. 2014). The southern AP marine-terminating glaciers (Fig. 1.6) show pronounced increases in their thinning rates since 2010 (Wouters et al. 2015). Strong thinning trends were found in Wordie Bay sector and along a ~750 km western coastal transect between the catchments of the Jensen Nunataks and the Wesnet and Williams Ice Stream (Fig. 1.6b) (Wouters et al. 2015).

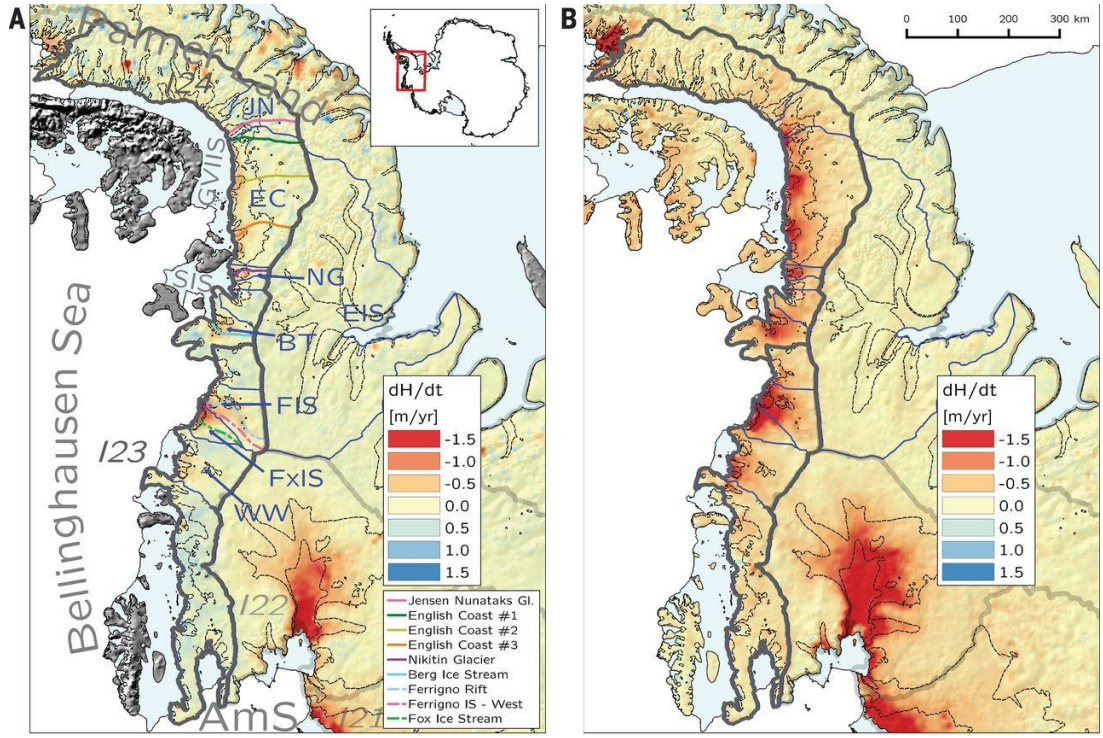

Figure 1.6 Surface elevation change rates of the southern Antarctic Peninsula. (A) ENVISAT/ICESat (2003-2009). (B) CryoSat-2 (2010-2014). Glacier basins of Wouters et al. (2015) study are outlined in blue: JN, Jensen Nunataks; EC, English Coast; NG, Nitikin Glacier; BT, Berg & Thompson Ice Stream; FIS, Ferrigno Ice Stream; FxIS, Fox Ice Stream; WW, Wesnet & Williams Ice Stream; EIS, Evans Ice Stream. The ice sheet mass balance inter-comparison exercise (IMBIE; Shepherd et al. (2012)) basins are shown in gray and pale gray and include the Fleming Glacier at top left. Ice shelves are plotted in light blue: GVIIS, George VI Ice Shelf; SIS, Stange Ice Shelf; AmS, Amundsen Sea. Reproduced from Wouters et al. (2015).

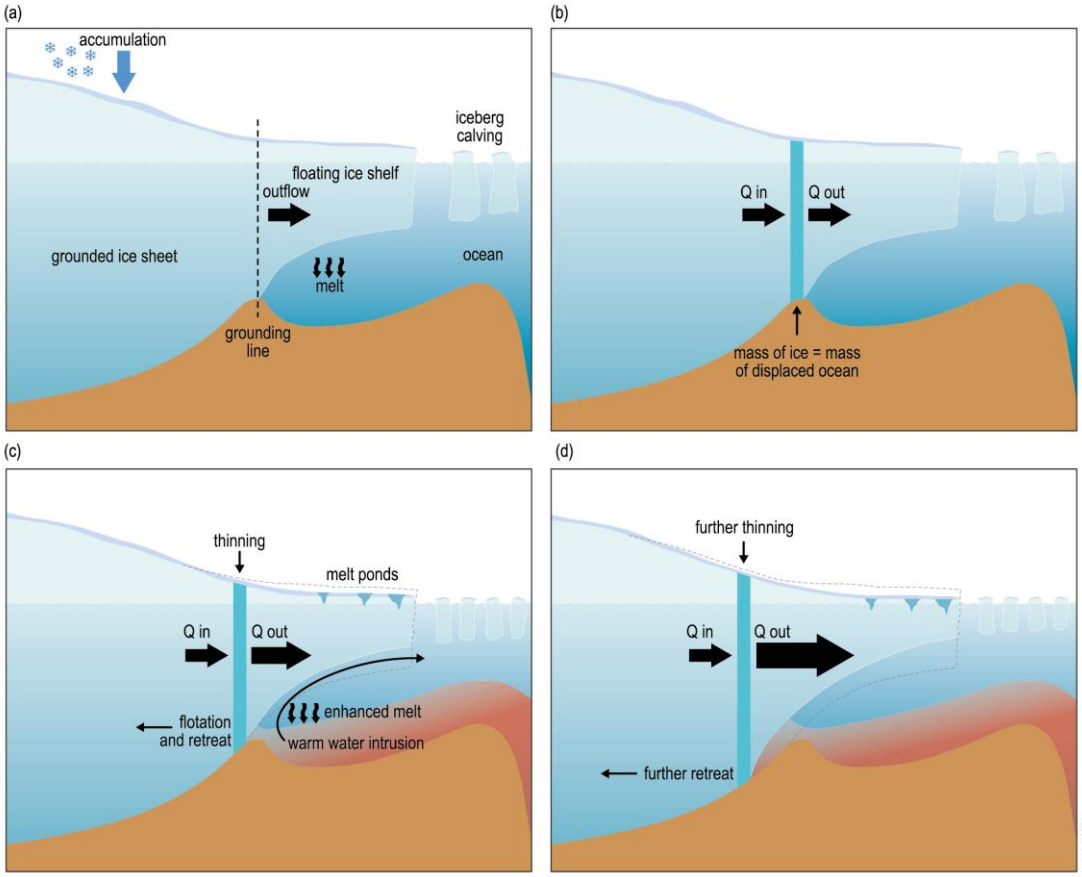

Figure 1.7 Schematic of the processes leading to the potentially unstable retreat of a grounding line showing (a) geometry and ice fluxes of a marine ice sheet, (b) the grounding line in steady state, (c) climate change triggering increased outflow from the ice sheet and the start of grounding line retreat and (d) self-sustained retreat of the grounding line (Church 2013).

Rapid acceleration and increased dynamic thinning in the WAIS and AP in the past few decades, especially over the recent two decades, implies that glaciers in those regions are in an unstable state. Most glaciers on the coasts of the WAIS and AP are marine-terminating and rest on a bed below sea level sloping down towards the ice sheet interior. Glaciers located on such reverse bed slopes are inherently vulnerable to increased basal melting, rapid dynamic thinning, and grounding line retreat. As shown in Fig. 1.7, the collapse and thinning of buttressing ice shelves in a marine glacier system should result in glacier acceleration, thinning, and grounding line inland migration for those glaciers with a retrograde bed slope (Schoof 2007). In the Bellingshausen coast, nearly 65% of the grounding line has retreated from 1990 to 2015 (Christie et al. 2016). Once perturbed past a critical threshold, such as grounding-line retreat over a bedrock hump into a region of retrograde slope, the grounding line will continue to retreat inward until the next stable state without any additional external forcing (Weertman 1974, Mercer 1978, Thomas and Bentley 1978). This “marine ice sheet instability (MISI)” has been invoked to explain the recent widespread and rapid grounding line retreat of glaciers in the Amundsen and Bellingshausen coast, possibly driven by increased basal melting reducing the

buttressing influence of ice shelves (Schoof 2012, Favier et al. 2014, Rignot et al. 2014, Christie et al. 2016, Arthern and Williams 2017, Hogg et al. 2017a). Rapid grounding line retreat and accelerated flow in these unstable systems leads to significant increases in ice flux and increased contribution from these marine ice sheets to sea-level rise. Although the MISI concept is largely based on theoretical arguments (Weertman 1974, Schoof 2012), numerical models with appropriate ice dynamics and resolutions (sub-km) have supported that MISI is a "real" phenomenon likely to be found in marine ice sheets, like the Pine Island Glacier in the WAIS (Favier et al. 2014).

1.4 Wordie Ice Shelf and Fleming Glacier System

The WIS (Fig. 1.8; $69^{\circ}10'$ S, $67^{\circ}30'$W) is one of seven ice shelves in the AP that collapsed in the last sixty years (Scambos et al. 2000, Cook and Vaughan 2010). The ice supply of the WIS is mainly from seven main marine-terminating glaciers (Fig. 1.8b), which connect to make three major input units. In the north, Hariot Glacier merges with another glacier 12 km upstream of the grounding-line; in the middle part, the Airy, Rotz, and Seller glaciers and Fleming Glacier merge around 15 km upstream of the grounding-line; and in the south, the Prospect Glacier and the Carlson Glacier merge close to the grounding-line (Reynolds 1988, Doake and Vaughan 1991a). The grounded ice flow from the Fleming Glacier into the ice shelf is split by Mount Balfour, which creates a central region of thinner and broken ice in its wake. Fifteen small ice rises and ice rumples existed within the pre-collapse glacier-ice shelf system, and it has been argued (Reynolds 1988, Doake and Vaughan 1991b, Vaughan 1993) that the major ice rises have had different roles in controlling the behavior of the ice shelf. When embedded in the ice shelf, the ice rises possibly helped stabilize the ice shelf and provided restraint at the grounding line by creating zones of compression upstream of pinning points; but during the ice front retreat, velocity and thickness changed so that areas of crevasses appeared upstream of the ice rises, and the ice rises may then have acted as indenting wedges for rifting and contributed to weakening the ice shelf (Doake and Vaughan 1991b, Vaughan 1993).

The WIS has disintegrated since 1966, with a particularly big iceberg calving event between 1988 and 1989, followed by a continuous steady retreat and almost-complete disappearance by 2008 (Fig. 1.8b) (Doake and Vaughan 1991a, Rignot et al. 2005, Cook and Vaughan 2010, Wendt et al. 2010). The retreat of the ice front led to a reduction in ice shelf area from about 2000 km^2 in 1966 to about 700 km^2 in 1989 (Doake and Vaughan 1991a). Between February 1972 and January 1974, 585 ± 30 km^2 of ice shelf had broken away, of which 90% had come from the southern part of the bay (Colvill, 1977). A further 265 ± 20 km^2 of ice shelf broke away between 1974 and 1979 from across the width of the ice front (Doake, 1982). After the collapse in 1989, the ice shelf was split into two separate parts (green line in Fig. 1.10b) (Doake and Vaughan 1991b). After further areal reduction until 1989, the ice shelf stabilized in the early 1990s, with even a minor re-advance in 1997, but shrank again in the following years, reaching a recorded minimum in 2009 with an area of 90 km^2 (Wendt

et al. 2010). The fronts of all glaciers except for Prospect Glacier, the southern branch of the Fleming Glacier and a local confined unnamed glacier next to Hariot Glacier coincided with the 1996 grounding line until 2009 (Fig. 1.10b). Since then, the ice front position remained quite stable except for the Prospect system where the floating parts calved and lost some ice (Friedl et al. 2018).

se

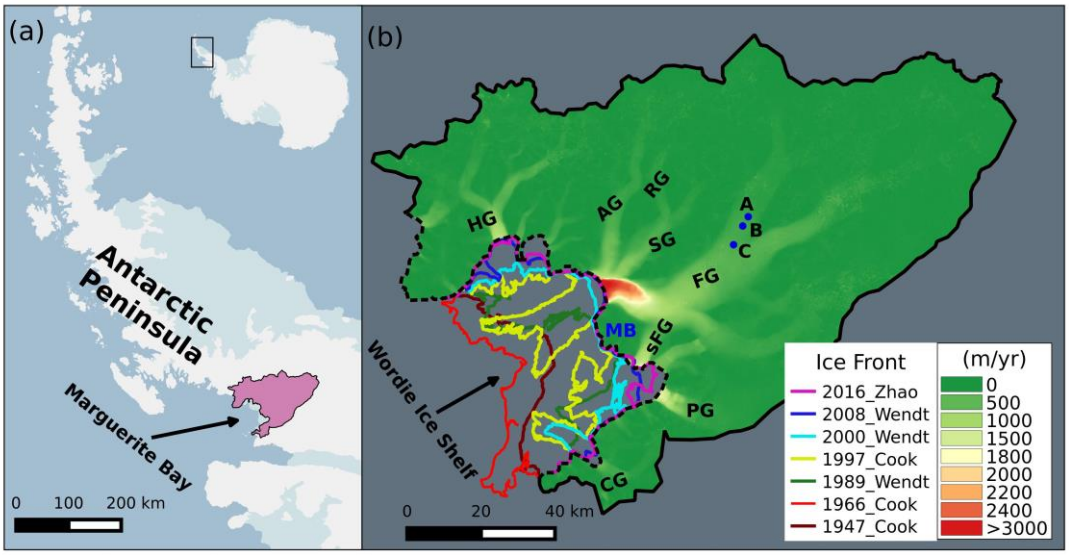

Figure 1.8 (a) Location of the Wordie Ice Shelf-Fleming Glacier system in the Antarctica Peninsula (pink polygon). (b) Surface speed in 2015 obtained from Landsat 8 data (Gardner et al. 2017) for the feeding glaciers. Colored lines represent the ice front position of the ice shelf in 1947, 1966, 1989, 1997, 2000, 2008 and 2016 obtained from Cook and Vaughan (2010), Wendt et al. (2010), Zhao et al. (2017). The dotted black line is the grounding line in 1996 from Rignot et al. (2011a) and the solid black line represents the catchment boundary from Cook et al. (2014). Points A, B and C marked on Fleming Glacier relate to the locations for which velocity time series are available. HG, AG, RG, SG, FG, sFG, PG and CG are short for Hariot Glacier, Airy Glacier, Rotz Glacier, Seller Glacier, Fleming Glacier, southern branch of Fleming Glacier, Prospect Glacier, and Carlson Glacier. MB is short for Mount Balfour.

Various factors could have caused the collapse of WIS, and climatic warming possibly acted as the primary driver by increasing ablation and the amount of melt water on the shelf (Doake and Vaughan 1991b), but this is not universally accepted, with some studies indicating that ice shelf thinning and retreat may be the result of oceanographic change (Shepherd et al. 2003, Cook and Vaughan 2010). Increasing air temperature has been observed at Rothera Station 240 km to the northwest of Fleming Glacier from 1979 to 1999 (Vaughan et al. 2001). Ice shelf buttressing would have been reduced owing to the removal of ice pinning points (ice rises and rumples) and reduction in longitudinal stress and lateral shear stress in Marguerite Bay (Doake and Vaughan 1991b). Surface crevasses and rifts, some initiated by ice rises, are also likely to be responsible for iceberg calving and weakening of the ice shelf, and those fracture processes were enhanced by the presence of increased surface melt water as a result of atmospheric warming in Marguerite Bay (Doake and Vaughan 1991b). The

existence of pinning points in Wordie Bay may explain the long-term steady retreat rather than a sharp retreat like that which occurred for Larsen A and B ice shelves (Wendt et al. 2010).

In response to the retreat and collapse of the ice shelf, grounded glaciers draining into the shelf accelerated and have been rapidly thinning and losing mass into the ocean. Surface ice-flow speed was measured at three sites upstream of the Fleming Glacier by Doake (1975), Rignot et al. (2005) and Wendt et al. (2010), and it shows that the Fleming Glacier accelerated significantly by 40-50% over the period of 1974 to 1996 at those sites, remained relatively stable from 1996 to 2008 (Wendt et al. 2010), and sped up again in early 2008 and during 2010-2011 (Friedl et al. 2018). Over 2008-2015, the Fleming Glacier, as the main tributary glacier, had the largest velocity changes across the whole Antarctic, with ~500 m yr^{-1} increase near the grounding line (Walker and Gardner 2017). With rapid acceleration of the Fleming system as a response to the ice shelf loss, grounded ice has been observed to be thinning at the same time (Wendt et al. 2010, Wouters et al. 2015, Friedl et al. 2018). The ice surface elevation change rates from 2004 to 2008 revealed the greatest lowering rates of 4.1 ± 0.2 m a^{-1} at the glacier front (Wendt et al. 2010). The comparison of thinning rates in the southern AP between 2003-2009 and 2010-2014 indicates a rapid increase in surface lowering of the Fleming system after 2009 (Wouters et al. 2015), which is consistent with the present study as shown in Chapter 2. It suggests a new equilibrium state has not been reached following the loss of the majority of the ice shelf, which has been confirmed in some recent studies (Walker and Gardner 2017, Friedl et al. 2018).

Generally, negative mass balance of tributary glaciers may be due to a combination of several factors that include reduced snow accumulation, an increase in surface melting, a dynamic response to a decline in ice shelf restraint, and an increase in basal sliding due to changing bed conditions. With the overall increase in snowfall since the 1850s confirmed at Gomez Plateau with ice-core data (Thomas et al. 2008) and negligible surface melting, the observed surface lowering and the increased ice velocity acceleration before 2008 are most probably related to dynamic thinning as a direct response to the loss of buttressing due to the ice shelf collapse (Rignot et al. 2005, Wendt et al. 2010). Recent studies have suggested that the post-2008 speedup and increased surface lowering of the grounded ice may indicate the onset of unstable rapid grounding line retreat as a response to oceanic forcing (Walker and Gardner 2017, Friedl et al. 2018). However, none of the past studies have modelled the glacier system and hence these hypotheses are untested.

1.5 Solid Earth response on ice unloading

1.5.1 Glacial isostatic adjustment (GIA)

Due to the mass loss of the major ice sheets following the Last Glacial Maximum (LGM) about 20,000 years ago, ice-ocean surface loads on the solid Earth have been redistributed, reshaping Earth's gravitational field, altering the orientation of its rotation pole, and causing viscoelastic deformation of the solid Earth (Peltier 2004);

these processes are collectively known as glacial isostatic adjustment (GIA). Antarctica, and especially the northern AP and the Amundsen Sea Sector with low mantle viscosities and thin lithosphere (Nield et al. 2014, Barletta et al. 2018), is experiencing GIA in response to changes in surface loading since the LGM deglaciation, which is important for modelling present-day GIA (Whitehouse et al. 2012a, King 2013, Nield et al. 2014, Wolstencroft et al. 2015, Martín-Español et al. 2016b, Sasgen et al. 2017).

The magnitude and spatial distribution of GIA are determined by two dominant factors: the spatiotemporal evolution of surface loading defines the forces applied to the surface of the Earth; the rheological structure of the Earth determines its isostatic response to the ice-loading. These, combined within a theoretical framework of GIA enables the prediction of three-dimensional solid earth deformation and gravity-field rate of change (Whitehouse et al. 2012a, King 2013, Peltier et al. 2015). The rheological properties refer to the Earth's viscoelastic properties, which govern the spatial pattern, magnitude and temporal evolution of deformation. Elastic deformation occurs immediately in response to loading changes, while the viscous behavior is time dependent and hence driven by ice loading changes over various timescales, for which the time periods depend on the viscosity of the mantle (Whitehouse 2009). In an Antarctic context, GIA modelling may help infer the extent and amount of the former ice masses, reconstruct sea level during glacial cycles, and constrain the Earth's structure and rheological properties (Whitehouse et al. 2012a, Ivins et al. 2013, King 2013, Argus et al. 2014).

Various geodetic measurements are sensitive to the effects of GIA. The Global Positioning System (GPS) allows measurement of the change in shape of the solid Earth and the Gravity Recovery and Climate Experiment (GRACE, e.g. Tapley et al. (2004), Barletta et al. (2013)) allows measurement of Earth's changing gravity field, from which ice/ocean mass redistribution can be deduced (Velicogna and Wahr 2006). GRACE data may be used to determine ice mass change, but first need to be corrected for GIA (Velicogna and Wahr 2006, King et al. 2012).

1.5.2 GIA modelling

Published GIA models differ substantially in terms of predicted solid Earth deformation in Antarctica, due to differences in the proposed amplitude and distribution of ice load since LGM and the different solid Earth rheologies adopted (Whitehouse et al. 2012a, King 2013). GIA is normally estimated using forward models, consisting of a deglaciation history model and an Earth rheology model (Peltier 2004), although inverse solutions have recently emerged based on satellite altimetry and GRACE observations (e.g., Gunter et al. (2014)).

Forward models, like the IJ05R2 (Ivins et al. 2013), ICE-6G_C (Argus et al. 2014, Peltier et al. 2015), W12 (Whitehouse et al. 2012b), A13 (A et al. 2013), and AGE1b (Sasgen et al. 2013) GIA models, have been extensively used to model the gravitational signal of GIA. The uncertainties of forward models are mainly from the

uncertainties in the ice loading history and the viscoelastic rheology used. The ICE-6G_C prediction is constrained by global ice extent and relative sea-level data while the IJ05R2 and W12 constrain their solutions to local geological constraints and substitut their Antarctic ice loading histories in place of Antarctic part of ICE-5G (Whitehouse et al. 2012b). The total contribution to global sea level rise from Antarctic ice mass loss since the LGM is larger in the ICE-6G_C model, with 13.6 m of eustatic sea level (ESL), than in the IJ05_R2 and W12 models with 7.5 m and 8 m ESL, respectively (Argus et al. 2014).

These GIA models adopt a 1D viscosity model (i.e., varying only in the radial direction). However, seismic tomography models show that substantial lateral variation in structure and temperature is likely, notably between East and West Antarctica, but also within each region (An et al. 2015). Using geodetic data and forward GIA modelling, Nield et al. (2014) constrained upper mantle viscosities in the northern AP to values (6×10^{17}–2×10^{18} Pa s) one to two orders of magnitude lower than widely adopted in 1D models (3×10^{19} Pa s; Ivins et al. (2011)), further reflecting regional variation. These suggest that 1D GIA models do not fully represent Earth structure in Antarctica.

Additionally, recent studies imply that GIA results are sensitive to the 3D (also including lateral) variations in solid Earth rheology (A et al. 2013, van der Wal et al. 2015), and these need to be considered. By using a model with 3D viscosity variations, Kaufmann et al. (2005) suggested that the upper mantle viscosity underneath West Antarctica is weaker than under East Antarctica, however the results showed that the 3D viscosity model gave a similar uplift rate pattern to a 1D viscosity model. Likewise, A et al. (2013) modelled GIA using a 3D viscosity profile derived from a realistic seismic tomography model and found a slight difference in the effect on ice mass change estimates compared with those made using a 1D model. However, using more recent Earth structure based on new seismic tomography, van der Wal et al. (2015) found that the effect of 3D viscosity on the spatial pattern of the gravity rates is often significant and the features cannot be replicated with a 1D viscosity model.

Inverse models, like the R09 (Riva et al. 2009), G14 (Gunter et al. 2014), and RATES (Martín-Español et al. 2016a), could infer the present-day uplift pattern due to GIA from a combination of GRACE and altimetry measurements and remove the dependence on the ice loading history and Earth rheological structure. However, those analyses are limited by assumptions about surface density change associated with firn compaction and varying surface mass balance, and by the resolution and coverage of the GRACE and altimetry data. The present-day uplift predictions from various GIA models (Fig. 1.9) show large differences between different solutions, and most models underestimate the observed uplift rates in the northern AP and the Amundsen Sea Embayment (Martín-Español et al. 2016b).

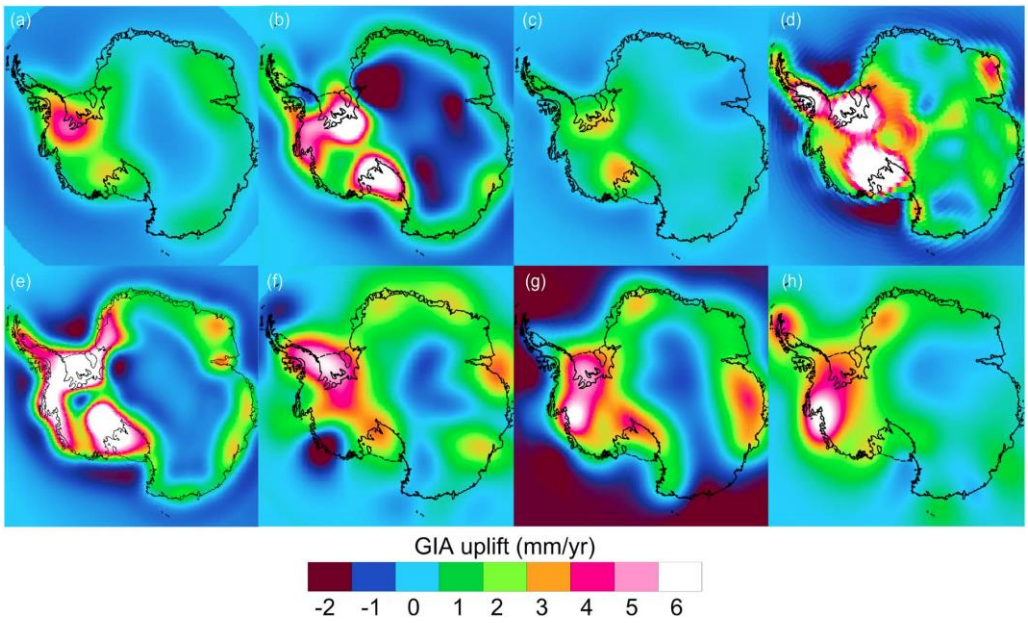

Figure 1.9 Predictions of Antarctic present-day uplift rates owing to glacial isostatic adjustment from recent GIA models and different solutions: (a) IJ05_R2, (b) W12, (c) AGE-1b, (d) A13, (e) ICE-6G_C (VM5a), (f) R09, (g) G14, and (h) RATES. Reproduced from Martín-Español et al. (2016b).

Conventional GIA models consider only millennial-scale ice mass changes following the LGM, assuming that deglaciation was complete several thousand years before present (e.g. Whitehouse et al. (2012a), Ivins et al. (2013), Argus et al. (2014)). As such, any loading changes since that time are not included, although the relatively high upper mantle viscosities employed in such models (5×10^{20} Pa s in ICE-6G_C (Argus et al. 2014), 2×10^{20} Pa s in IJ05_R2 (Ivins et al. 2013), and 1×10^{21} Pa s in W12 (Whitehouse et al. 2012b)) mean that small mass losses during the last few thousand years would have little impact on the present-day deformation pattern. This is not the case, however, if mantle viscosities are lower than 10^{20} Pa s (Ivins et al. 2000). Indeed, owing to the collapse of several ice shelves in the northern AP since 1995, the solid Earth response to the resulting ice mass loss has been observed in GPS records, such as the markedly increased uplift in GPS records associated with ice unloading owing to the breakup of Larsen B Ice Shelf in 2002 (Nield et al. 2014). A purely elastic response to unloading in the northern AP has been shown to be insufficient to explain the observed uplift pattern, while a rapid viscoelastic response (upper mantle viscosities (UMV) $<3\times10^{18}$ Pa s) demonstrates very good agreement with the observations (Thomas et al. 2011, Nield et al. 2014). Compared to the northern AP, the southern AP (Palmer Land) overall appears to have a significantly stronger rheology (UMV of $1\text{-}3\times10^{20}$ Pa s) (Wolstencroft et al. 2015). Focusing on the southern limit of the AP, Wolstencroft et al. (2015) found they could not explain the spatial pattern of uplift observed by GPS after elastic correction, and concluded that poorly known late Holocene (last few thousand years) loading changes may be responsible, due to low mantle viscosities in this region. Reconstruction of high spatial and temporal resolution ice history in the southern AP is essential to better model the GIA of the whole of Palmer Land.

1.6 Research Objectives

The objectives of this study are to investigate the dynamic response of glaciers feeding the WIS to ice shelf disintegration and the response of the solid Earth to the ice unloading history in the past 50 years, and to use ice sheet modelling to better understand the ice dynamics and mechanisms behind the rapid acceleration in ice flow and dynamic thinning over this period. After a long period of retreat and collapse since the 1960s, little remains of the WIS. However, the processes governing ice-shelf retreat and their influence on glacier dynamics are still not completely understood. Further, it is still unclear how the solid Earth in the southern AP has responded to grounded-ice loss in the past few decades. This study aims to contribute to the understanding of the above scientific questions.

This thesis includes five chapters, three of which were written as separate papers with specific objectives. A summary of the overall objectives of those chapters is outlined below:

Chapter 2 Rapid Ice Unloading in the Southern Antarctic Peninsula and its Effect on Bedrock Uplift Rates

Objective 1: Quantify the ice unloading history from 1966 to 2015 and explore the viscoelastic properties of the southern Antarctic Peninsula by comparing simulated and observed rates of bedrock deformation.

The WIS has experienced a history of retreat since 1966. The elevation change rates of the Fleming Glacier system since 2002 are well documented but the full loading history since the commencement of retreat in the 1960s is not known, and consequently neither is the solid Earth response. In this chapter, multi-source satellite data were used to quantify the elevation changes from 1966 to 2015. Using the full ice loading changes in the past 50 years, the solid Earth rheology in this region was then well constrained by comparing simulated and observed rates of bedrock deformation. Simulated and observed bedrock deformations were compared at three GPS sites to indicate how the bedrock responded to the ice mass unloading and whether the GPS site motion across Palmer Land could be explained with recent ice loading changes combined with realistic solid Earth models.

Chapter 3 Basal friction of Fleming Glacier, Antarctica, Part A: sensitivity of inversion to temperature and bedrock uncertainty

Objective 2: simulate the ice flow in the WIS-FG system to infer the spatial distribution of basal friction coefficients and test the sensitivity of this inverse modelling to bedrock datasets, ice front position, and ocean-pressure boundary conditions.

The retreat of the WIS has continued for more than four decades, and the Fleming Glacier, as its main feeding glacier, has shown continuous acceleration in recent decades even after the almost-disappearance of the ice shelf. Why did the Fleming system keep thinning and speeding up even

after most of the ice shelf had collapsed? Ice sheet modelling can help better understand the ice dynamics to answer this question. Inverse methods are commonly used in ice sheet models to infer the distribution of basal friction coefficients and basal velocities from the glacier topography and observed surface velocities. In this chapter, the Stokes Elmer/Ice ice sheet model was used to simulate the basal friction coefficients of the WIS-FG system with an inverse method and a proposed multi-cycle spin-up scheme. To better constrain the model, experiments were used to explore the sensitivity of inverse modelling to the assumed initial englacial temperature distribution, bedrock datasets, ice front positions, and ice front boundary conditions.

Chapter 4 Basal friction of Fleming Glacier, Antarctica, Part B: evolution from 2008 to 2015

Objective 3: Infer the basal shear stress distribution of the WIS-FG system in 2008 and 2015 and explore the mechanisms behind the rapid dynamic changes that occurred during this period.

As a marine glacier system resting on a retrograde bed, the rapid speedup and dynamic thinning of the Fleming system in recent decades may indicate unstable inland movement of the grounding line. Changes in basal shear stress linked with the ice flow could suggest the possible grounding line movement. In this chapter, the basal shear stress distributions in both 2008 and 2015 were simulated with an inverse method using the Elmer/Ice model. Through the comparison of basal shear stress and height above buoyancy in both epochs, the stability of the grounding line during this period was analyzed. An ongoing marine ice sheet instability and direct ocean warming as possible reasons for increased speed-up and thinning were discussed.

Chapter 5 Discussions, conclusions and future directions

In this chapter, I conclude the research results about the ice unloading history in the past 50 years and the response of solid Earth, discuss the possible reasons of the significant acceleration and thinning of the Fleming system, and propose the future research directions on such marine ice sheet systems.

Chapter 2

Rapid Ice Unloading in the Southern Antarctic Peninsula and its Effect on Bedrock Uplift Rates

Chapter 2 quantifies ice mass loss from 1966 to 2015 and explores the response of the solid Earth to ice unloading during this period. The content of this chapter was published as Zhao et al. (2017) and is re-formatted for this thesis but otherwise presented as published in:

Zhao, C., M. A. King, C. S. Watson, V. R. Barletta, A. Bordoni, M. Dell and P. L. Whitehouse (2017). "Rapid ice unloading in the Fleming Glacier region, southern Antarctic Peninsula, and its effect on bedrock uplift rates." Earth and Planetary Science Letters 473: 164-176.

2.1 Abstract

Rapid regional warming in the Antarctic Peninsula has led to significant retreat and eventual collapse of several major ice shelves since the 1970s, triggering the subsequent acceleration and thinning of their feeding glaciers. The Wordie Ice Shelf, lying off the west coast of the Antarctic Peninsula, has undergone long-term disintegration since the 1960s with a substantial calving event occurring around 1989, followed by continuous steady retreat and its almost-complete disappearance. The dynamic response of the upstream glaciers to the ice shelf collapse and the response of the solid Earth to the associated mass loss are not fully understood. To quantify the mass loss from the system, we generated a digital elevation model (DEM) using airborne vertical and oblique imagery from 1966 and compared it to a DEM derived from 2008 SPOT data. This analysis reveals lowering over that time of approximately 60 m at the front of Fleming Glacier. Using IceBridge and ICESat-2/GLAS data spanning 2002-2014, we show an increased magnitude of mean elevation change rate, with rates post-2008 more than twice those of 2002-2008. We use these load change data as a basis for the simulation of viscoelastic solid Earth deformation. We subtract modelled elastic deformation rates, and a suite of modelled viscous rates, from GPS-derived three-dimensional bedrock velocities at sites to the south of Fleming Glacier to infer properties of Earth rheology. Assuming the pre-breakup bedrock uplift was positive due to post-Last Glacial Maximum (LGM) ice retreat, our viscoelastic-corrected GPS uplift rates suggest upper mantle viscosities are $> 2\times10^{19}$ Pa s and likely $>1\times10^{20}$ Pa s in this region, 1-2 orders of magnitude greater than previously found for the northern Antarctic Peninsula. Horizontal velocities at the GPS site nearest the Fleming Glacier, after the application of elastic and plate tectonic corrections, point away from Marguerite Bay rather than the present glacier front. This suggests that horizontal plate motion in the region reflects the earlier retreat of

the glacier system following the LGM, compatible with a relatively strong mantle in this region. These findings highlight the need for improved understanding of ice load changes in this region through the late Holocene in order to accurately model glacial isostatic adjustment.

2.2 Introduction

Rapid regional climate warming in the second half of the 20th Century, in both the atmosphere and ocean (Cook et al. 2016), led to the retreat and disintegration of major ice shelves across the Antarctic Peninsula (AP) and extensive changes in coastal tributary glaciers (Cook et al. 2005, Wendt et al. 2010, Wouters et al. 2015, Cook et al. 2016). In response to the loss of floating ice shelves and ice in fjords, outlet glaciers have exhibited acceleration and dynamic thinning (Rignot et al. 2004, Seehaus et al. 2016). A purely elastic response to unloading in the northern AP has been shown to be insufficient to explain the observed uplift pattern, while a rapid viscoelastic response demonstrates very good agreement with the observations (Thomas et al. 2011, Nield et al. 2014). For the southern AP (Palmer Land), a significantly stronger Earth model with a higher upper mantle viscosity has been suggested (Nield et al. 2012, Whitehouse et al. 2012a, Ivins et al. 2013, Argus et al. 2014, Wolstencroft et al. 2015), although the observed pattern of present-day deformation, including an anomalous southward motion in northernmost Palmer Land, is yet to be fully explained by models(Wolstencroft et al. 2015).

Wordie Ice Shelf (WIS) (Fig. 2.1) is one of seven AP ice shelves that collapsed in the last sixty years (Scambos et al. 2000, Cook and Vaughan 2010). The WIS entered a period of sustained but intermittent retreat in the 1960s, and subsequently Fleming Glacier, its main tributary glacier, has accelerated and thinned through to end of 2008 (Rignot et al. 2005, Wendt et al. 2010). As such, the WIS system represents a very good example of long-term sustained dynamic thinning following the retreat/collapse of an Antarctic ice shelf.

In this paper we revisit the thinning of the glaciers feeding WIS, using airborne and satellite altimetry to quantify the changing elevation from 1966 through to early 2015 (hereafter elevation change is assumed to be equivalent to ice thickness change). We then consider the effect of the estimated high-resolution loading changes on the solid Earth, by considering models of elastic and viscoelastic deformation. In particular, we attempt to use observed responses to these relatively well quantified ice loading changes to constrain the solid Earth rheology in this region. Furthermore, we test the hypothesis put forward by Wolstencroft et al. (2015) who suggested that the anomalous southward motion of northern Palmer Land could be due to recent ice loading changes in the WIS region.

2.3 Background

2.3.1 Changes in ice dynamics

The WIS lies off the west coast of the AP, in Marguerite Bay, and drains a grounded catchment of 15,000 km^2 (Vaughan 1993). It is fed by seven glaciers (Fig. 2.1), which

can be divided into three main input units: Hariot glaciers in the north; Airy, Rotz, Seller, Fleming and Prospect in the middle; and Carlson in the south.

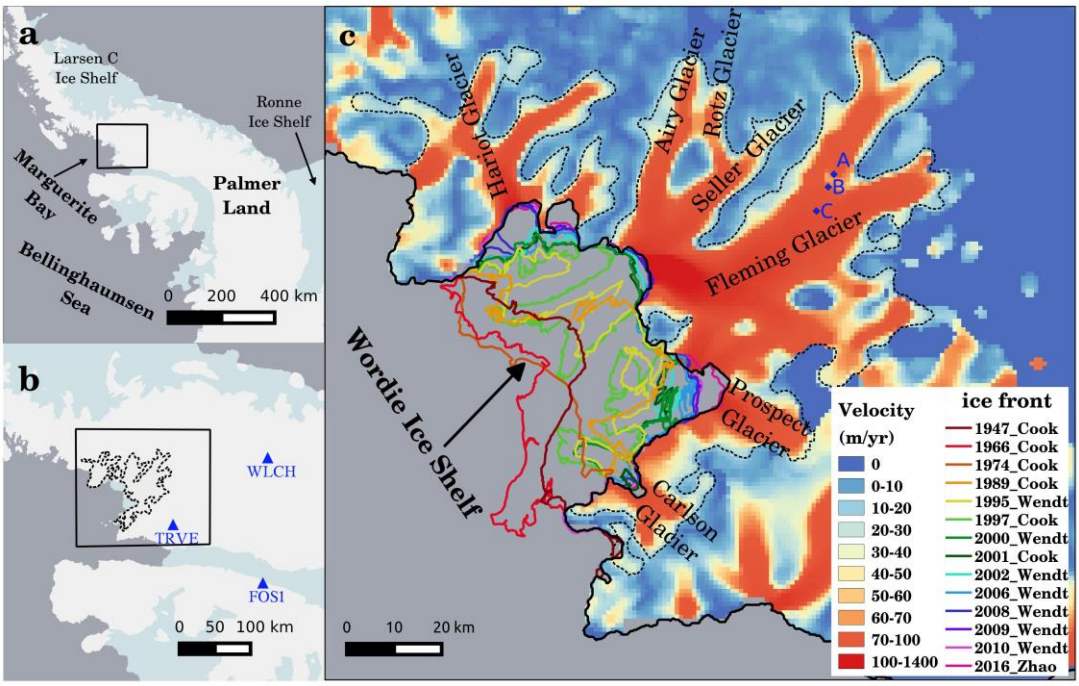

Figure 2.1 a) Location of Wordie Ice Shelf, Antarctic Peninsula. b) Three GPS sites near the Wordie Ice Shelf c) Ice front positions of Wordie Ice Shelf and its feeding glaciers. The shading relates to the observed ice velocity derived during austral summer 2007-2008 from Rignot et al. (2011) and recorded ice shelf fronts are shown in colored lines (Cook and Vaughan 2010, Wendt et al. 2010). The dotted black line is the boundary of ice velocity greater than 20 m/yr acquired from Rignot et al. (2011) and the solid black line is the grounding line in 1996 from Rignot et al. (2011a). Points A, B and C marked on Fleming Glacier relate to the locations for which velocity time series are available.

The WIS has undergone a series of calving events since the 1960s with a significant breakout between 1988 and 1989 as shown in Figure 1 (Doake and Vaughan 1991a, Rignot et al. 2005, Cook and Vaughan 2010, Wendt et al. 2010). After this, the ice shelf area and front stabilized until around 1997 before gradually retreating back towards its present location (Doake and Vaughan 1991a, Cook et al. 2005, Wendt et al. 2010).

The temporal evolution of change is shown in Fig. 2.2. We added an ice front position for February 2016, extracted from a Landsat 8 OLI_TIRS scene, revealing that the remaining ice shelf has an area of just 54 km^2 (using the 1996 grounding line from Rignot et al. (2011a)). The fronts of all glaciers now coincide with the 1996 grounding line except for Prospect Glacier, Carlson Glacier and an unnamed glacier next to Hariot Glacier (see the 2016 ice front in Fig. 2.1c).

Likely as a result of the collapse of the ice shelf, the feeding glaciers of the WIS accelerated and have been rapidly thinning and losing mass into the ocean. The velocity of the upstream region of Fleming Glacier (locations A, B and C on Fig. 2.1c)

increased by 40-50% between 1974 and 1996, remained largely unchanged in 2008 (Fig. 2.2) (Doake 1975, Rignot et al. 2005, Wendt et al. 2010), but increased sharply again between 2008 and 2015 despite almost no ice shelf remaining in front of Fleming Glacier since 2008. Detailed elevation change data have been published for the period 2004-2008 over Fleming Glacier and show the greatest change at its downstream extent with lowering of up to 4.1$\pm$ 0.2 m/yr between December 2004 and December 2008 (Wendt et al. 2010).

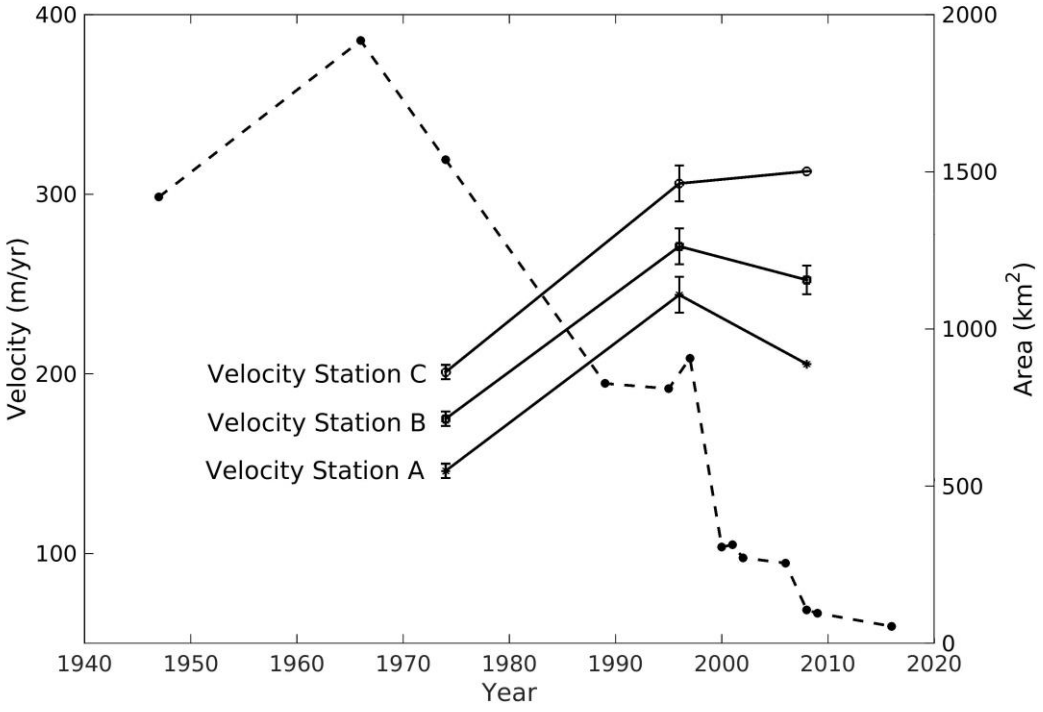

Figure 2.2 Time series of the Wordie Ice Shelf area (dashed line) compiled from different sources (Wendt et al. (2010), Cook and Vaughan (2010) and Landsat 8 OLI_TIRS data in Feb 2016) and of ice velocities at three locations (A, B, and C at Fig. 2.1c) in 1974 and 1996 from Doake (1975) and Rignot et al. (2005). The ice velocities at Station A and C in 2008 were from Wendt et al. (2010) and at station B from Rignot et al. (2011).

2.3.3 Glacial Isostatic Adjustment

Due to the demise of the major ice sheets following the Last Glacial Maximum (LGM), ice-ocean surface loads on the solid Earth have been redistributed, reshaping Earth's gravitational field, altering the orientation of its rotation pole, and causing viscoelastic deformation of the solid Earth (Peltier 2004); these processes are collectively known as glacial isostatic adjustment (GIA). Inputs required in a GIA model include the rheology of the Earth and the spatiotemporal evolution of ice-loading, enabling the prediction of three-dimensional solid earth deformation and geoid rate change (Whitehouse et al. 2012a, King 2013, Peltier et al. 2015).

Conventional models of Antarctic GIA consider only millennial-scale loading changes following the LGM, and they often assume that deglaciation was complete

several thousand years before present, e.g. Whitehouse et al. (2012a), Ivins et al. (2013), Argus et al. (2014). As such, any loading changes since that time are not accounted for, although the relatively high upper mantle viscosities employed in such models (5×10^{20} Pa s in ICE-6G_C (Argus et al. 2014), 2×10^{20} Pa s in IJ05_R2 (Ivins et al. 2013), and 1×10^{21} Pa s in W12 (Whitehouse et al. 2012b)) mean that small load changes during the last few thousand years would have little impact on the present-day deformation pattern. This is not the case, however, if mantle viscosities are lower than 10^{20} Pa s (Ivins et al. 2000). Indeed, the viscoelastic deformation of the AP due to recent (centennial to decadal) ice load changes has been the subject of several recent studies (Nield et al. 2012, Nield et al. 2014, Wolstencroft et al. 2015). For example, Nield et al. (2014) found it necessary to invoke mantle viscosities of 6×10^{17} - 2×10^{18} Pa s to explain the rapid uplift of the northern AP following the breakup of the Larsen B Ice Shelf in 2002. Focusing on the southern limit of the AP, Wolstencroft et al. (2015) found they could not explain the spatial pattern of uplift observed by GPS after correction for elastic deformation, and concluded that poorly known late Holocene (last few thousand years) loading changes may be responsible, implying that mantle viscosities are sufficiently low to allow for deformation over this timescale.

While Wolstencroft et al. (2015) did not extensively consider horizontal GPS velocities, they noted that the southward motion of GPS site TRVE (Fig. 2.1b) was anomalous to the pattern of deformation recorded at the other sites. Southward motion at TRVE would be consistent with late Holocene ice unloading in the Marguerite Bay region, which would be sufficiently distant that it would not affect other GPS sites in the region, but the timing of this unloading is poorly known. Millennial-scale GIA models simply assume that the grounding line had retreated back to approximately the present location by ~5 calibrated thousand years (cal ka) before present (BP) based on the radiocarbon dates from marine sediment cores (Bentley et al. 2011, Whitehouse et al. 2012b, Ó Cofaigh et al. 2014), and they do not account for any recent changes associated with the WIS retreat, some of which are poorly understood.

As described above, ice load changes during the last 20 years are well documented but the full loading history since the commencement of retreat in the 1960s is not known, and consequently neither is the solid Earth's response. We next describe new datasets that help constrain the loading changes in this region.

2.4 Data and Methods

2.4.1 Ice Unloading History

2.4.1.1 Altimetry data during 2002-2015

We assembled elevation measurements from Operation IceBridge and pre-IceBridge campaigns (2002, 2004, 2008-2011, 2014) (Krabill, 2014, updated 2016), and Geoscience Laser Altimeter System/Ice, Cloud, and land Elevation Satellite (GLAS/ICESat, Feb 2003 to Oct 2009) (Zwally et al., 2014). From these we determined elevation change rates (dh/dt), fitting a linear regression to all

measurements in each cell of a regular 250 m grid that has at least 3 measurement points (see Sec. A1 in the Appendix A). Here, we limit our dh/dt analysis to regions with velocity greater than 20 m/yr (Rignot et al. (2011b), dotted line in Figs. 2.1b, 2.1c), since the dh/dt could be ignored in low velocity areas. The dh/dt showed clear correlation with absolute elevation (Figs 2.3c, 2.3d).

For our loading computations we need complete coverage of the three main feeding glacier regions and we computed this based on the observed dh/dt and glacier hypsometry. We evaluated the fit of the hypsometric model to the data for chosen grid cells using a weighted root mean square error (RMSE), and the RMSE is 0.89 m/yr and 0.20 m/yr pre- and post-2008, respectively (see Fig. 2.3 and Sec. A1 in the Appendix A).

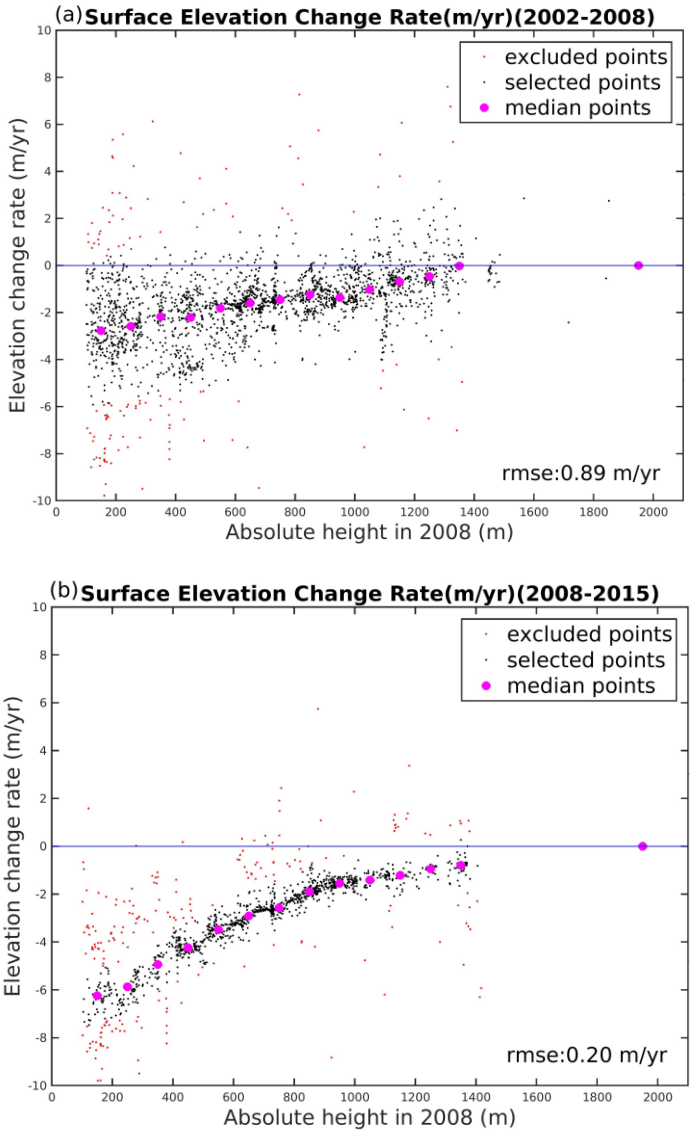

Figure 2.3 Elevation change rates (black dots) a) over 2002-2008 and b) over 2008-2015 against absolute surface height in 2008. The magenta dots are the median values for each 100 m height bin. Red dots represent grid cells excluded from the RMSE computation.

To compare our dh/dt values with those previously published using the ATM data from 2004 and 2008 only (Wendt et al. 2010) we computed dh/dt for three different periods (2002-2004, 2004-2008 and 2008-2015). Aside from Fleming Glacier, Prospect Glacier, Airy Glacier, Rotz Glacier, and Seller Glacier, where the majority of the airborne data focus (referred to hereafter as the Fleming system), we also made use of data from the two other main feeding regions (Hariot Glacier and Carlson Glacier; referred to hereafter as the HC system). We found that dh/dt values across the Fleming system did not change much over 2002 to 2008, but their magnitudes increased markedly after 2008, coinciding with an increase in ice velocity (Fig. 2.2) suggesting this is a result of dynamic mass loss. While data coverage for the HC system is spatially sparse, the rate of lowering appears to have remained stable from 2002 to 2015. So, for the loading deformation calculations below, we assumed that the surface lowering rate of Fleming system remained constant during 2002-2008 (Fig. 2.4a) and 2008-2015 (Fig. 2.4b), and that dh/dt values across the HC system did not change over the whole time period (that is, the rates in Fig. 2.4a were used). The interpolated surface lowering rates at the front of Fleming Glacier (computed at elevation 150 m) are 2.77±0.89 m/yr during 2002-2008 and 6.25±0.20 m/yr during 2008-2015, respectively.

To estimate mass change over the entire region, we created a digital elevation model (DEM; WGS84 ellipsoid) of the feeding glaciers by merging an ASTER 100 m DEM product (Cook et al. 2012) with the SPIRIT 40 m DEM from SPOT 5 (Korona et al. 2009), and then resampled the merged product to 1000 m resolution. Using this DEM, the distribution of dh/dt for all feeding glaciers was determined via linear interpolation of the hypsometric model (Fig. 2.3). The results are shown in Figs. 2.4.

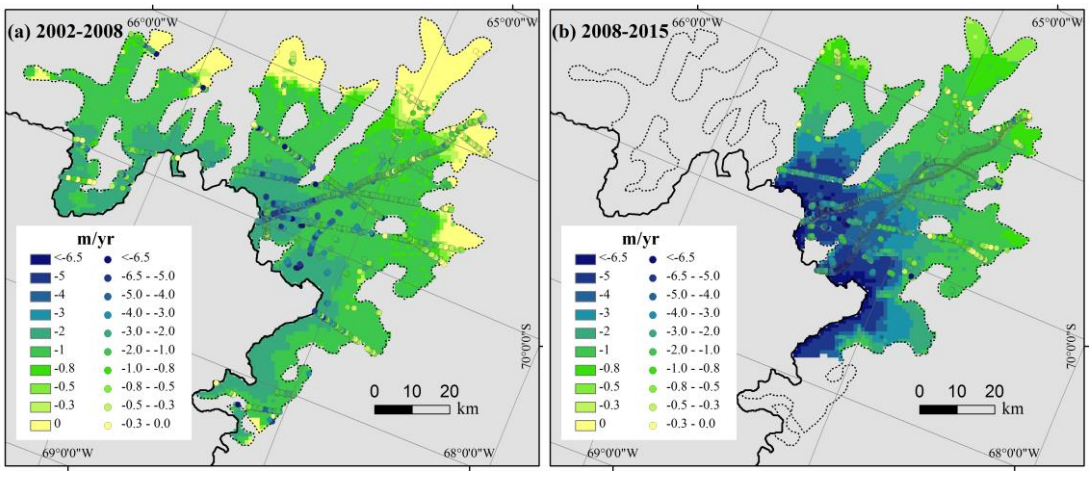

Figure 2.4. The distribution map of dh/dt during a) 2002 to 2008 and b) 2008-2015. Dots indicate the elevation change rates of grids derived from altimetry data. The maps cover the same region as Fig. 2.1c.

2.4.1.2 Elevation changes during 1966-2008

To understand the elevation change pattern before 2002, we generated a DEM for 1966 using historic aerial photographs from November 1966 taken as part of the historical mapping campaigns (see Sec. A2 in the Appendix A). The 1966 DEM was

then co-registered to the 2008 SPOT DEM (Korona et al. 2009) to estimate the elevation changes during 1966-2008 (See Sec. A2 in the Appendix A). Differencing the co-registered DEMs provided estimates of surface elevation change. Median surface lowering near the front of Fleming Glacier was nearly 60 m (taken along two ice flow lines and three transverse lines parallel to the grounding line in the very front of Fleming Glacier; see Fig. 2.5) between 1966 and 2008 (nearly 41 years), equivalent to a mean surface lowering rate of 1.5 m/yr. A region upstream of the grounding line shows a total lowering of 80-100 m between 1966 and 2008 (see Fig. 2.5); we return to the implications of using a different surface lowering value in the discussion.

2.4.1.3 Temporal interpolation of changes prior to 2002

To simulate the viscoelastic response of the solid Earth to ice mass change we need an ice loading history. The elastic component (which must be accounted for within the GPS measurements) depends on contemporaneous ice load changes, while the viscous response also depends on past ice load changes. The extent of the time span to be considered depends largely on the mantle viscosity, however, which is unknown.

We start by assuming that the glacier system was stable before 1966. This assumption is supported by the small net change in the ice front position from 1947 to 1966 (Fig. 2.1c), but the precise evolution of the glacier system prior to the velocity observation in 1996 (Rignot et al. 2005), and near-continuous elevation measurements from 2002, is uncertain. To begin with, we assume that the lowering rate for 1996-2002 is the same as for 2002-2008, based on the observation of similar velocities over these two periods (Fig. 2.2).

In Sec. 2.4.1.2, we determined that the mean surface-lowering rate over 1966-2008 was 1.5 m/yr at the glacier front. We now determine the surface lowering rate for different epochs within this period: the surface-lowering rate from 2002 to 2008 (see Fig. 2.5) was approximately 2.5 m/yr (Fig. 2.4a). Therefore, the ice thinned by 15 m during 2002-2008 or equivalently 30 m during 1996-2008. This implies that lowering between 1966 and 1996 must have been ~30 m (or at a mean rate of 1 m/yr). In the absence of further information, we developed two plausible end member scenarios for the period 1966 to 1996, each with a total thinning of the ice front of 30 m (~ 1 m/yr on average). The scenarios are illustrated in Fig. S1 in terms of dh/dt, normalized to the values for 1996-2008. Scenario 1: As one end member we assume that the retreat of WIS in the 1960s substantially perturbed the back-stress on the grounded ice and hence resulted in a near-instantaneous increase in ice velocities (as observed for the Larsen B tributary glaciers, e.g. Rignot et al. (2004)). We assume that the increase in ice velocities resulted in a constant surface-lowering rate of 1 m/yr, which persisted until 1996. Between 1996 and 2008 a higher rate of surface lowering was assumed. Scenario 2: As the other end member, we assume that the glaciers gradually increased in velocity from 1966 to 1996 as a result of a gradual reduction in back-stress as the ice shelf thinned and retreated. Using our constraint on total surface lowering from 1966 to 1996, the magnitude of dh/dt is uniformly increased 5 times over this period.

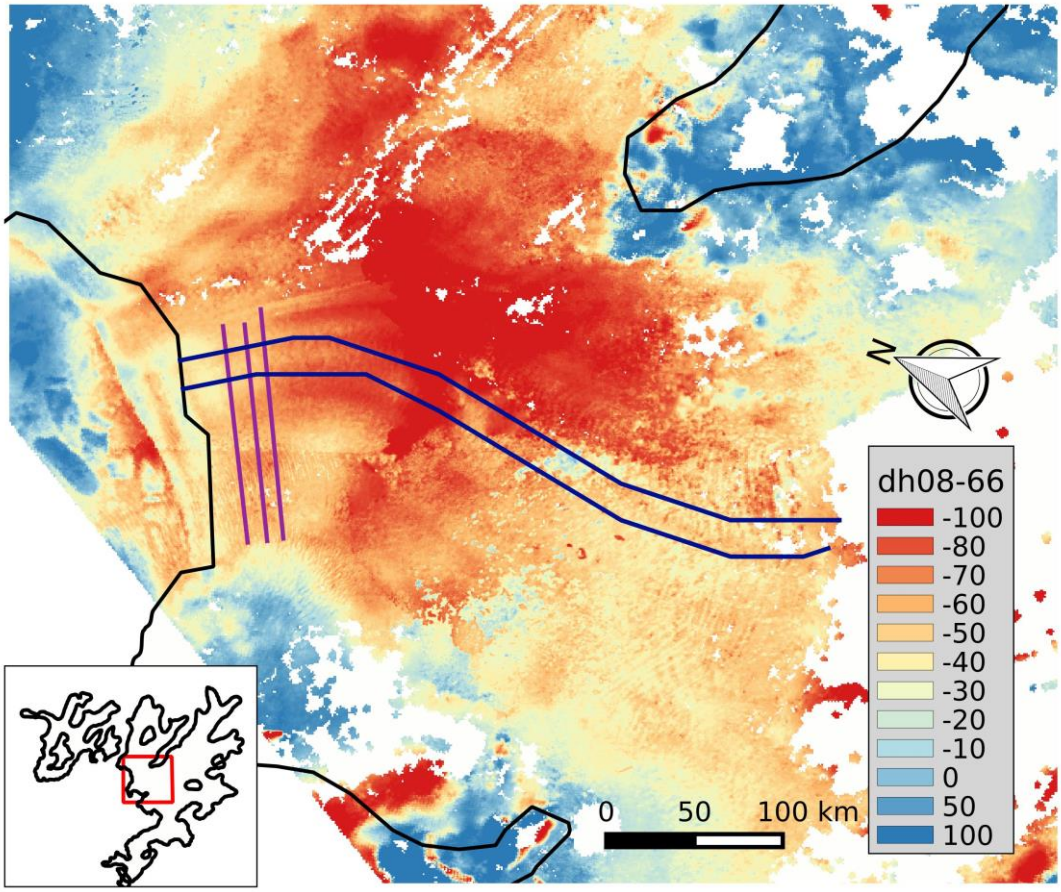

Figure 2.5 Elevation changes over 1966-2008. Black lines indicate the boundary of feeding glaciers with velocity > 20 m/yr. Blue and purple lines are the ice flow lines and the sampling lines used to compute the median of elevation change at the front of the Fleming Glacier, respectively. Inset map of the feeding glaciers shows the location of DEM data in 1966 (red box). The inset map covers the same region as Fig. 2.1c.

As described in Sec. 2.4.1.1, the Fleming system has different surface lowering rates over the periods 2002-2008 and 2008-2015, while the HC system maintained a constant thinning rate during 2002-2015. For both glacier systems, we presume that the spatial pattern of elevation changes prior to 2002 was consistent with that over 2002-2008. To generate the spatial field of change for earlier periods, we scale the map of 2002-2008 elevation changes.

For the loading computations, we convert from elevation change rate to mass change rate (dm/dt) by accounting for modelled firn compaction and surface mass balance (SMB) anomalies (see Sec. A3 in the Appendix A).

2.4.1.4 Far-field loading changes

For the far-field loading changes in Antarctica we adopt an approach and datasets similar to Wolstencroft et al. (2015). That is, we used ice mass trends for the northern AP (2002-2006, 2006-2011) obtained from Nield et al. (2014), a 5 km gridded ice loading history for the southern AP and Alexander Island (Nov. 2010-Sep. 2013) derived from CryoSat-2 data by McMillan et al. (2014), and detailed mass change in

the southern AP based on ICESat data from 2003 to 2009, acquired by Gunter et al. (2014) (see Table 2.1). For the post-2008 period, we assume that ice mass change rates have remained constant since the latest observation in the northern AP, southern AP and the Alexander Island. We modified the above to exclude data points inside the feeding glacier system of the WIS, noting that the uncertainty of CryoSat-2 dh/dt data in this region, as used by Wolstencroft et al. (2015), is greater than 0.65 m/yr.

Table 2.1 List of satellite data for ice surface elevation

Satellite	Sensor / Product/Version	Time Series	Space Resolution	Height reference System
IceBridge	Airborne Topographic Mapper / ATM	2002, 2004, 2008	Sample width: 80 m Spacing along track: 40 m	WGS84 ellipsoid
	Airborne Topographic Mapper / ILAM2 / Version 2	2009-2014		
	Land, Vegetation, and Ice Sensor / LVIS2/vERSION 1	2011, 2014	20 m	
ICESat-1	Geoscience Laser Altimeter System (GLAS) / GLA12 / Version 34	2003-2009	172 m	TOPEX/Poseidon ellipsoid (GRS80 ellipsoid)
ASTER	Global Digital Elevation Model Version 2 / GDEM	2002-2009	100 m	
SPOT	SPOT 5 stereoscopic survey of Polar Ice: Reference Images and Topographies / SPIRIT DEMs	2007,2008	40 m	EGM96 geoid

2.4.2 GPS

Three continuous GPS (cGPS) stations are located within ~200 km of Fleming Glacier, namely TRVE, FOS1, and WLCH, with their locations shown in Fig. 2.1b (blue triangles) and Table 2.2. We focus on these sites as they are the most sensitive to ice load changes in the feeding glaciers of the WIS. All of them were installed during the 2009-10 Austral summer (Wolstencroft et al. 2015). FOS1 also has three occupations prior to 2009, in 1995, 1996 and 1998. The same sites were used by Wolstencroft et al. (2015) although our analysis makes use of more recent data (Table 2.2). GPS data were analyzed as described in Wolstencroft et al. (2015), removing the effect of atmospheric loading displacements in post-processing (Petrov 2015); such a correction is particularly important for Antarctic time series (Santamaría-Gómez and Mémin 2015).

Time series at FOS1 have offsets evident in at least the vertical component prior to 2009, presumably due to the changes in equipment that occurred during site occupations. As it is not possible to robustly model these offsets in our analysis, together with the limited data before 2009, we do not consider the early parts of the record from FOS1.

Before considering the horizontal time series further, we removed the effects of plate rotation using the plate rotation of Argus et al. (2014). As noted by Wolstencroft et al.

(2015) there is uncertainty in removing plate rotations from Antarctic GPS data, which is expressed as a bias in the residual horizontal velocities (see also (King and Santamaría-Gómez 2016a), King et al. (2016b)); we consider this issue further below. We estimate site velocities from 2009 to 2015 using CATS software (Williams 2008) at the same time as annual and semi-annual terms and assuming a white-plus-flicker noise model. The resulting velocities and uncertainties are shown in Table 2.2.

Table 2.2 GPS site names, locations, velocities, uncertainties, corresponding elastic correction, and modelled three-dimensional deformation from ICE-6G (VM5a) and W12. The horizontal components have been corrected for plate rotation using the Euler pole and rate from Argus et al. (2014): 59.876, −127.277, 0.2178 (lat (deg), lon (deg), rate (deg/Ma)). Uncertainties are one standard deviation (68% confidence intervals). The ICE-6G rates were interpolated from 1 degree grids whereas the W12 estimates are directly computed at the sites with the best fitting Earth model for the West Antarctic sites described in Whitehouse et al. (2012a), and are taken from Wolstencroft et al. (2015).

Site	Lat	Lon	GPS collection (yyyymmdd)		Vertical rate (mm/yr)	Vertical Uncertainty σ_V (mm/yr)	Horizontal velocities after plate rotation correction (mm/yr)		Horizontal Uncertainty (mm/yr)	
			Start	End			North	East	σ_N	σ_E
FOS1	-71.31	-68.32	20091218	20150210	1.63	0.90	0.57	0.52	0.30	0.26
TRVE	-69.99	-67.55	20091222	20141025	3.68	0.68	-1.62	0.01	0.30	0.29
WLCH	-70.73	-63.82	20100315	20151102	1.02	0.73	0.06	-0.08	0.26	0.32

Site	Lat	Lon	Elastic Correction (mm/yr)	ICE-6G (mm/yr)	W12 1D (mm/yr)	Elastic Correction (mm/yr)	ICE-6G (mm/yr)	W12 1D (mm/yr)	Elastic Correction (mm/yr)	ICE-6G (mm/yr)
			Vert.	North	East	Vert.	North	East	Vert.	North
FOS1	-71.31	-68.32	1.82	-0.09	0.13	1.82	-0.09	0.13	1.82	-0.09
TRVE	-69.99	-67.55	2.97	-0.44	-0.29	2.97	-0.44	-0.29	2.97	-0.44
WLCH	-70.73	-63.82	1.38	-0.18	0.38	3.80	-0.52	0.24	4.64	0.69

2.4.3 Viscoelastic Modelling

2.4.3.1 Elastic modelling

For the elastic modelling we follow the approach previously used by Nield et al. (2014) and Wolstencroft et al. (2015). That is, we used the elastic output of the VE-HresV2 (Visco-Elastic High Resolution technique for Earth deformations) code (Barletta et al. 2006). The load Love numbers were computed to a maximum spherical harmonic degree of 3700 based on a compressible, self-gravitating Earth using VE-CL0V3RS v1.4 (Visco-Elastic Compressible LOVe numbER Solver) with a Preliminary Reference Earth Model structure (Dziewonski and Anderson 1981). We use the load Love numbers to compute Green's functions, which are spatially convolved with ice loading discs according to the methods presented in Barletta et al. (2006). The ice history, described in Sec. 2.4.1, is converted from ice elevation change to mass change for the feeding glaciers of the WIS, and as described in Wolstencroft et al. (2015) for other regions.

Ice load changes across Alexander Island are not known before 2008, so we tested the sensitivity of our modelled displacements at TRVE and FOS1 to assumptions of either no ice load change over Alexander Island before 2008 or a constant rate of ice mass

change during the whole period 2002 to 2015. The results revealed small differences (0.29 and 0.25 mm/yr for vertical rate difference, 0.09 and 0.09 mm/yr for horizontal rate difference at FOS1 and TRVE respectively, which is smaller than the GPS uncertainty) and accordingly we regard ice load change across Alexander Island as negligible during 2002-2008.

We assumed negligible changes in ice load prior to 2002 in any region except for the feeding glaciers of WIS, and adopted a constant rate of mass change extending from the most recent data period to the present-day (e.g., 2011-2015 for the northern AP, and 2010-2015 for Alexander Island and southern AP; see Table 2.1). Changes in the far northern AP related to the mid-1990s breakups of the Larsen A and Prince Gustav ice shelves will not be of significant consequence here due to the relatively lower viscosity in that region (Nield et al. 2014) .

2.4.3.2 Viscous modelling

We again follow Nield et al. (2014) in constructing a model of the Earth's viscous response to ice load changes, adopting a 4-layer model with a purely elastic lithosphere underlain by three distinct viscous layers with linear Maxwell rheology. We use the time-dependent viscous load Love numbers generated (with the code VE-CL0V3RS v1.4) for Nield et al. (2014), which were explicitly computed at sufficient epochs to allow interpolation (where necessary) with <10% error. The maximum spherical harmonic degree is 1195, which is sufficient for the spatial and temporal scale of the viscous response considered here.

The viscosity and thickness of the various layers are free variables in this model, which are not well constrained in this region. In the northern AP, Nield et al. (2014) found a preferred model with lithospheric thickness (LT) 100 -140 km and upper mantle viscosity (UMV) between 6×10^{17} Pa s and 2×10^{18} Pa s. In the far south of the AP, Wolstencroft et al. (2015) found a best-fit model with LT 120 km and a higher UMV of 1-3 $\times 10^{20}$ Pa s. We test a wide range of values for the Earth model (345 models), adopting an elastic lithosphere in the range 20 km to 130 km, a viscoelastic upper mantle of 400 km with viscosity between 1×10^{17} Pa s and 3×10^{20} Pa s, a fixed viscosity transition zone with a base at 670 km and viscosity of 4×10^{20} Pa s, and a lower mantle with a viscosity of 1×10^{22} Pa s. Using even higher UMV would result in an elastic-only response over this time-period.

To compute the time series of modeled viscous deformation for each candidate Earth model at each GPS site, we convolved the viscous Love numbers with each of the two scenarios for ice loading history. We use the same load change datasets as in the elastic modelling. For the tests that follow, we primarily adopt Scenario 2, but also discuss the effect of adopting Scenario 1.

2.4.4 GIA modelling

The above modelling only considers decadal-scale load changes, while our GPS velocities could also be sensitive to any ongoing deformation related to earlier

(centennial- or millennial-scale) GIA signal. To explore the direction and magnitude of this, we consider the output of two millennial-scale GIA models: the ICE-6G_C (Argus et al. 2014, Peltier et al. 2015) and W12 models (Whitehouse et al. 2012b), the latter was computed using both 1-D and 3-D Earth rheologies as described in King et al. (2016b). Predicted uplift rates at the GPS sites from the ICE-6G_C and W12 1D models are listed in Table 2.2.

2.5 GPS results

The GPS horizontal and vertical velocities of TRVE, FOS1 and WLCH are presented in Table 2.2 and Fig. 2.6 after correction for plate rotation and elastic effects. Our GPS velocities for these sites are slightly different to those of Wolstencroft et al. (2015) due to our longer data period and an improved dataset for the elastic correction. Our higher-resolution ice loading data for Fleming Glacier produced a slightly greater elastic correction at the TRVE and WLCH sites as a result of a greater ice mass loss than that derived using CyroSat-2 data post-2010.

Fig. 2.6b shows that the modelled horizontal elastic deformation vector at TRVE (red dotted arrow) points away from Fleming Glacier as a result of the large center of ice mass loss at that location. However, unlike the Wolstencroft et al. (2015) horizontal vector after plate rotation correction and elastic correction, our GPS analysis results in a corrected horizontal vector at TRVE that points away from the center of Marguerite Bay (red arrow in Fig. 2.6b). If viscous deformation in this region were dominated by decadal-scale mass loss from the Fleming Glacier system, the vector would be expected to point away from the glacier (red dots in Fig. 2.6b). Instead, our data suggests that viscous deformation in the region does not just reflect the response to ice mass loss in the Fleming Glacier system, but also the effect of earlier ice load changes in Marguerite Bay since the LGM. Adopting an alternative model of plate rotation (Altamimi et al. 2011) would result in a TRVE horizontal vector that points even further into Marguerite Bay. The potential for biases in these derived plate rotation estimates (King and Santamaría-Gómez 2016a, King et al. 2016b) means this conclusion is not definitive, however, and we explore the rheology further below. Unfortunately, FOS1 and WLCH are too far away for their horizontal velocities to provide useful information as to the distribution of ice mass change in the Fleming Glacier/Marguerite Bay region.

2.6 Model fit analysis

We compared the GPS data with results from the various combined viscoelastic models, and calculated the misfit in both the vertical and horizontal directions. In the tests below we make use of the Scenario 2 loading history (Fig. A1b), but we also refer to scenario 1 for comparative purposes.

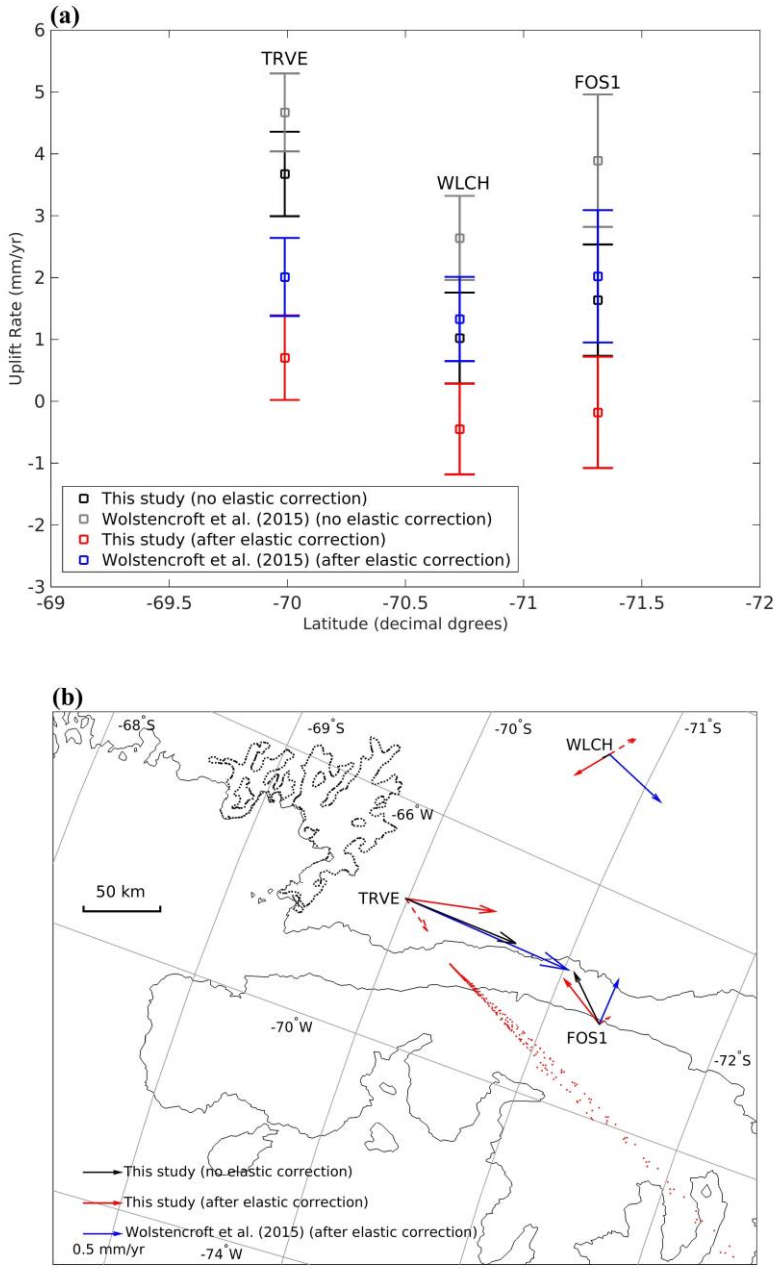

Figure 2.6. a) Observed GPS uplift rates without elastic correction from this study (dark gray) and Wolstencroft et al. (2015) (light gray), and observed GPS uplift rates after elastic correction from this study (red) and as published by Wolstencroft et al. (2015) (blue). b) Map view of observed GPS horizontal deformation rates at three sites. The black solid arrow shows the original measured horizontal rates after plate rotation correction. The red and blue solid arrows represent the horizontal rates after plate rotation correction and elastic correction from this study and as published by Wolstencroft et al. (2015), respectively. The red dashed arrow displays the elastic correction component from this study. The red dots show the predicted viscoelastic deformation at TRVE from the range of models in this study, considering post-1966 loading changes only.

2.6.1 Viscoelastic modelling constrained by GPS vertical velocities

First, we estimated the background (pre-1966) vertical velocity by computing the difference between observed and predicted uplift rates at TRVE, WLCH, and FOS1. We assume this background velocity is dominated by ice load changes from earlier time periods. This assumption is supported by predictions from both the ICE-6G_C and W12 1D models, which suggested positive uplift rates at the three GPS sites (Table 2.2) as a result of millennial-scale deglaciation. Ongoing uplift through to the late Holocene is also supported by evidence for relative sea level fall in Marguerite Bay over this period (Simkins et al. 2013).

On this basis, we test the appropriateness of the proposed viscoelastic models by assuming that the background rate of bedrock uplift in this region must be either close to zero or positive. Fig. 2.7a shows that background rates at TRVE are only close to zero or positive when upper mantle viscosities are greater than about 1×10^{20} Pa s. In contrast, there is little sensitivity to choices of LT at this site. Consideration of the uncertainty in the GPS velocity (σ_V in Table 2.2) would allow for only a slightly smaller lower limit to the UMV (2×10^{19} Pa s) (Fig. 2.7a).

The same comparisons at FOS1 and WLCH reveal a generally lower sensitivity to choice of Earth model due to their location farther away from Fleming Glacier. Considering them separately to TRVE, they allow for a relatively lower viscosity and thinner lithosphere (Figs. 2.7b and 2.7c), although viscosities lower than about 1×10^{18} Pa s are still excluded for most lithospheric thicknesses. Considering all sites together suggests a lower bound for the UMV of around 1×10^{20} Pa s, which is substantially larger than the value preferred for the northern AP (Nield et al. (2014) indicated by the red star in Fig. 2.7a) and consistent with the models for the whole of Palmer Land proposed by Wolstencroft et al. (2015) (cyan star in Fig. 2.7a).

We repeated the above analysis, which was based on Scenario 2 (S2; Fig. A1b), but using Scenario 1, and reached very similar conclusions regarding the preferred Earth model (Fig. A4). That is, our finding that UMV in this region is greater than 1×10^{20} Pa s is not strongly sensitive to the timing of recent ice load changes.

We also explored the effect of making different assumptions when constructing our load change dataset (see Sec. A3). All of these tests suggest an UMV greater than around 2×10^{19} Pa s, and we suggest this is a robust lower bound for our Earth model. This bound is consistent with the preferred model of Wolstencroft et al. (2015).

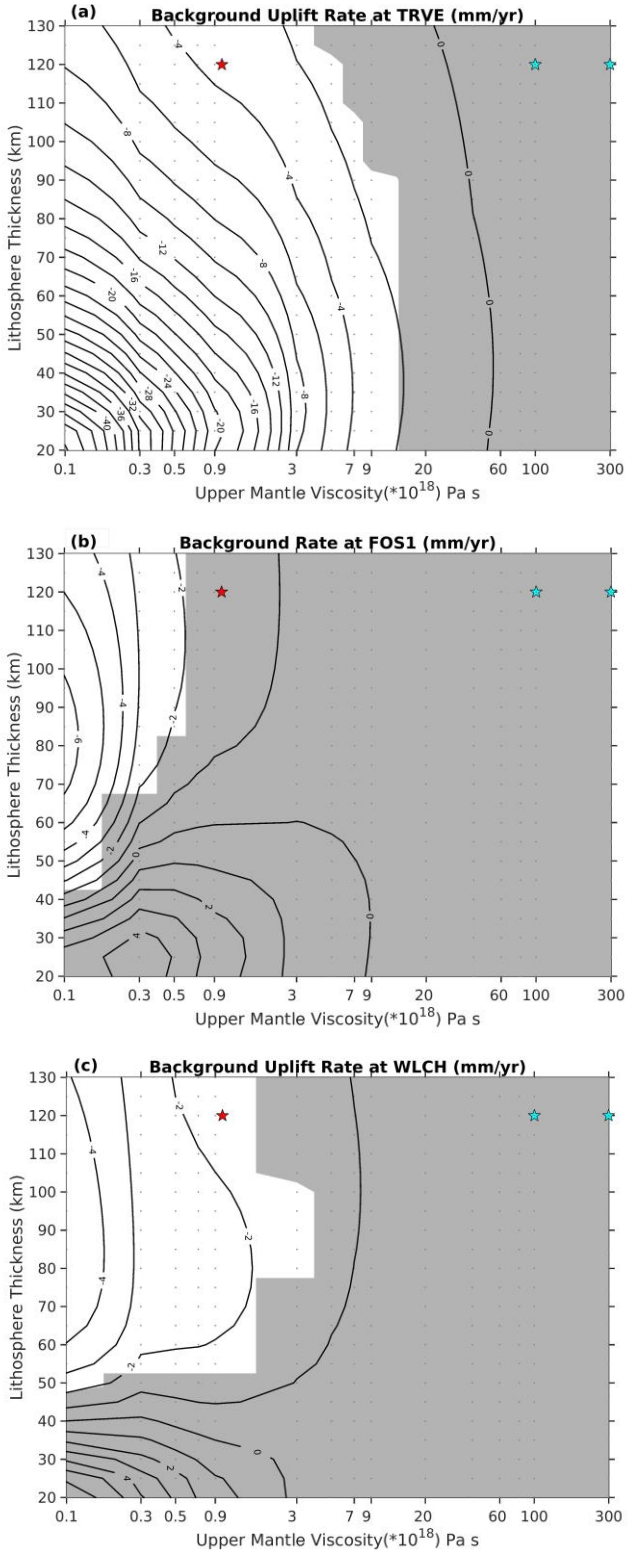

Figure 2.7. Estimated pre-1966 background uplift rates as a function of viscoelastic model setup at a) TRVE, b) FOS1 and c) WLCH. The red star is the best fit model for the northern AP from Nield et al. (2014), and the cyan stars span the range of upper mantle viscosities preferred by Wolstencroft et al. (2015). The black lines are contours of the implied vertical background rate. The gray shading areas indicate the Earth models with background rate greater than or equal to zero while considering measurement uncertainty (i.e., > $-2\sigma_V$).

2.6.2 Viscoelastic modelling constrained by GPS horizontal velocities

We next evaluated the different models by considering their ability to explain the observed horizontal velocities. We assume that the remaining signal after plate rotation correction can be explained by a sum of the decadal-scale viscoelastic deformation and that from late Holocene or earlier GIA (Argus et al. 2014). For simplicity, we extract a single rate of decadal-scale deformation at 2012.0 from each model. In the absence of late Holocene load data, we limit ourselves to exploring the general magnitude and direction of deformation predicted by millennial-scale GIA models. We considered predictions from ICE-6G_C, W12 1D, and another eight W12 models that were combined with 3D, power-law viscosity models; these vary as a function of mantle grain size, water content and seismic model, as described by King et al. (2016b). We note that even in the presence of an UMV as low as 2×10^{19} Pa s, with a relaxation time of ~2000 years, some surface deformation will be driven by large spatial-scale loading changes over longer (millennial-scale) periods interacting with the lower mantle (e.g., Argus et al. (2014)).

Fig. 2.8 shows the measured horizontal velocity at TRVE (black arrow in Fig. 2.8) after application of the plate rotation correction. The FOS1 and WLCH horizontal vectors are small and the observation uncertainties were not small enough to separate the various models. In addition to the observed horizontal velocity at TRVE we also plot the predicted horizontal velocity at this location due to decadal viscoelastic deformation (using 345 different Earth models; black points in Fig. 2.8). Some black points fall inside the observation 2σ (95% confidence interval) uncertainty ellipse but relate to Earth models with the UMV < 9×10^{18} Pa s and the LT < 60 km, which have already been ruled out as shown in Fig. 2.7a. If we instead applied the ITRF2008 plate rotation model (Altamimi et al. 2011), the observed GPS rates at TRVE would rotate anticlockwise, further away from the model predictions. It is possible that this misfit between observed and predicted horizontal velocities could be explained by signal related to ice mass loss further offshore during deglaciation.

To explore the potential contribution to present-day deformation from millennial-scale GIA, which includes the response to mass loss from across the whole of Marguerite Bay, each of the 345 decadal-scale viscoelastic model predictions were summed with each of the millennial-scale GIA predictions (colored dots in Fig. 2.8). We take care not to over-interpret these summed predictions given the different rheological frameworks employed in the different decadal-scale and millennial-scale models. While some models, which include millennial-scale GIA, move the predictions away from the observation, some are closer and indeed a few points are now located inside the uncertainty ellipse of the observed motion. The closest points (in dark green) use the W12 3D model (S-dry-10 mm). Considering the sensitivity to changes in the decadal-scale Earth model only, those predictions inside the error ellipse are largely insensitive to LT changes (bottom-left inset in Fig. 2.8), but prefer an UMV ranging from 7×10^{18} Pa s to 3×10^{20} Pa s (bottom-right inset in Fig. 2.8).

Taking into account GPS velocity uncertainties and the uncertainty in modelling plate tectonics and viscoelastic deformation, we are unable to identify a unique set of preferred Earth models via the analysis of horizontal velocities. However, we do find that post-1966 deformation alone cannot explain the observed horizontal velocity at TRVE, and conclude that there must be a contribution from pre-1966 mass loss within Marguerite Bay. In general, our horizontal rates provide a less definitive lower bound on UMV than vertical rates, but we once again find that the UMV in this region is very likely greater than that found in the northern AP.

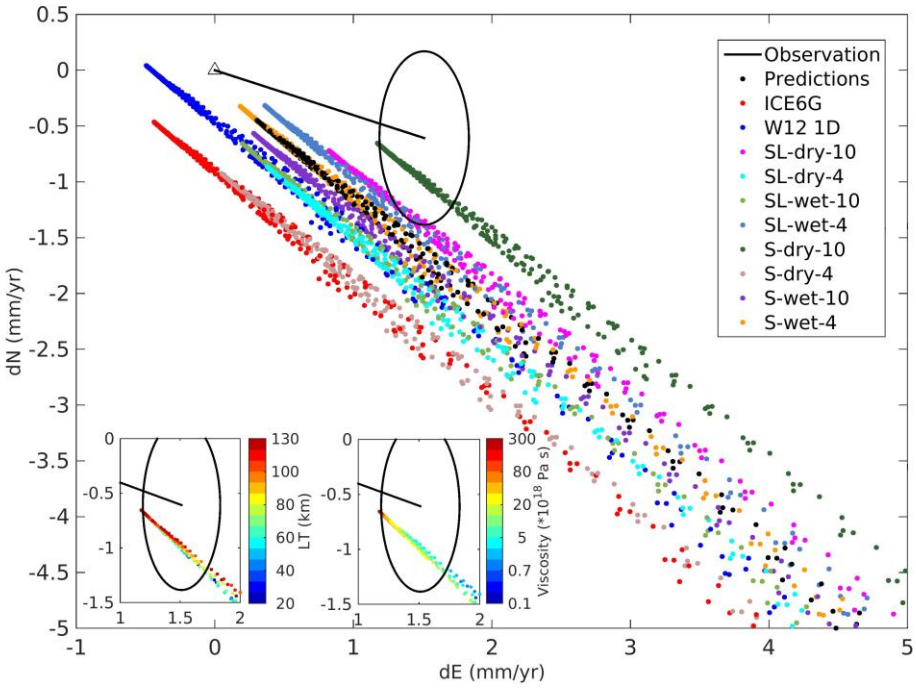

Figure 2.8. Observed and predicted horizontal rates at TRVE. The black arrow and ellipse indicate the observed GPS horizontal velocity after plate rotation correction and the 2σ uncertainty (σ_N and σ_E in Table 1), respectively. The black points are modelled horizontal velocities due to post-1966 viscoelastic deformation, as detailed in this study (one dot per 345 different model realizations). The colored points are modelled horizontal velocities calculated by summing the predicted post-1966 horizontal velocities from this study (black points) and the post-LGM deformation rates from various millennial-scale GIA models. The two inset panels show the lithospheric thickness and upper mantle viscosity of various models after removing the post-LGM deformation rates using W12 3D (S-dry-10 mm).

2.7 Discussion

A previous study has calculated ice elevation change rates for Fleming Glacier by comparing data from 2004 and 2008 (Wendt et al. 2010). Our study extends this analysis to span 1966-2015. Our quantification of total lowering since 1966 demonstrates dynamic mass loss sustained over 50 years, indicating that this glacier is likely still far from achieving a new equilibrium. The Fleming Glacier system represents one of the best-quantified examples of long-term change of an Antarctic

glacier system following the retreat/collapse of its ice shelf (although we note that ice shelf retreat has been episodic rather than instantaneous, meaning several perturbations to back-stresses have possibly occurred). Little is known of the bathymetry in front of the present-day glacier, and hence it is not known if this historic change is related to unstable grounding line retreat across a reverse sloping bed or not (Schoof 2007).

Underscoring the sustained loss is the sharp increase in the rate of ice surface-lowering at the ice shelf front after 2008 (-6.25±0.20 m/yr) to values more than twice that of the 2002-2008 rate (-2.77±0.89 m/yr), which is consistent with the observed ice velocity increases between 2008 and 2015. This post-2008 lowering is 4 times the multi-decadal average during 1966-2008 (1.5 m/yr), highlighting the magnitude of the dynamic response of the feeding glaciers to the recent disappearance of the ice shelf. We note that these ice elevation change rates could have been higher for a period of time within 2002-2008 or 1966-2008 but the average during these periods is lower than 2008-2015.

Thinning of grounded ice unloads the solid Earth and induces a viscoelastic response. Our quantification of mass change since the ice shelf breakup provides a relatively unusual opportunity to constrain viscous Earth rheology; GIA modelling usually includes uncertainties in both ice history and earth structure, and strong trade-offs between the two are typically present (e.g., Fig. 2.4 in Argus et al. (2014)). In contrast, while uncertainties exist in the earliest part of our ice history, our findings remain robust to different assumptions in that we require at least moderate upper mantle viscosities (> 2×10^{19} Pa s) in all cases, with little sensitivity to LT. Our preferred dm/dt model suggests that this region is underlain by upper mantle with a similar viscosity (> 1×10^{20} Pa s; Fig. 2.9a) to that found for all of Palmer Land (Wolstencroft et al. 2015). The lack of detailed ice history prior to ice shelf retreat and the short-duration GPS observations are the primary reasons that we cannot further narrow the range of the best fitting Earth models for this region. Improved accuracy and temporal-spatial coverage of GPS data as well as more late Holocene ice extent constraints are therefore essential.

This UMV is in contrast with that found by Nield et al. (2014) in the northern AP, where preferred upper mantle viscosities are around 1×10^{18} Pa s. Allowing for uncertainties in the Earth models we infer for the WIS region, it seems likely that UMV varies by at least a factor of 10 in just over 500 km, although we note the limitation that we cannot represent such structure within the Earth models used in this study. It remains to be determined how smoothly this change occurs.

Wolstencroft et al. (2015) suggested that the pattern of GPS-observed uplift in Palmer Land could not be explained by existing GIA models and that ice histories in the south-west Weddell Sea region were in some way incorrect – either needing greater ice loss since the LGM or more localized loss during the late Holocene and a moderate-to-low mantle viscosity (1-3×10^{20} Pa s). Our new finding that the TRVE horizontal velocity points away from Marguerite Bay rather than Fleming Glacier is

suggestive of a continued response to ice load changes associated with grounding line retreat from a substantially more advanced position within Marguerite Bay. This is in agreement with our findings based on vertical uplift rates and confirms that late Holocene or earlier mass load changes play an important role in defining the solid Earth response of this region. Evidence suggests that initial grounding line retreat occurred within Marguerite Trough at ~14 cal ka BP (Ó Cofaigh et al. 2014) and continued until 9.2-9.6 ka BP (Bentley et al. 2011, Simkins et al. 2013), but little is known of the mid-to-late Holocene ice history of the region.

There is evidence for relative sea-level (RSL) fall in the Marguerite Bay region between ~5.5-7.3 ka BP and 2.5 ka BP, initially at a rate of 3.3 mm/yr, and then at a rate of ~1.4 mm/yr after 2.5 ka BP (Simkins et al. 2013). Given that global deglaciation had largely ended by this period and hence far-field drivers of sea level change were small, we assume that the late-Holocene RSL fall is dominated by local vertical land motion. The solid Earth implications of this sustained uplift depend on the extent to which local ice load changes occurred after 9.2 ka BP, which is not known. An early termination of deglaciation combined with our finding of relatively high mantle viscosity is compatible with this observation, but this is not the only plausible scenario and further Holocene ice loading data are required.

Finally, Nield et al. (2012) investigated the magnitude of solid Earth subsidence associated with accumulation increases in the southern AP between 1855 to 2010, for a range of Earth models. When they used an Earth model that is consistent with our analysis (a thick lithosphere of 71 km and a UMV of 1×10^{20} Pa s), they predicted a present-day subsidence rate of up to 3.2 mm/yr, although we note that their GIA model resolution is not ideal for high resolution studies. We have not considered their loading change in this study because our observation of changes in some way overlap with those reconstructed by the ice sheet model output used by Nield et al. (2012) and hence there is a danger of double-counting. Repeating this modelling effort is a substantial undertaking beyond the scope of the present study. Nonetheless, regional subsidence over the past 150 years or so makes it plausible that the vertical background rates shown in Fig. 2.7a could be negative (i.e., uplift prior to the 1850s, then subsidence over 1850-1966), which would bring about a downward revision to our estimated lower bound on upper mantle viscosity.

2.8 Conclusion

We provide a 50-year quantification of ice elevation changes of glaciers feeding the WIS, associated with the retreat and collapse of this ice shelf. We then use this quantification in conjunction with viscoelastic modelling to provide constraints on viscous Earth rheology in this region.

Comparing DEMs derived from historical aerial photography from 1966 and a satellite-derived DEM from 2008, we identify more than 60 m of ice surface lowering over this time. High-resolution elevation data over 2002 to 2014 in the Fleming Glacier system reveals a changing temporal response of the feeding glaciers with no

sign of abatement in glacier thinning. Indeed, thinning rates from 2008-2015 were substantially greater than rates averaged over 1966-2008 and 2002-2008. The increased dynamic thinning in this region may be associated with the intrusion of warm Circumpolar Deep Water or mid-depth oceanic warming, perhaps in addition to a possible retrograde bed (Wouters et al. 2015, Cook et al. 2016). The glaciers feeding the WIS are yet to reach a new equilibrium some 50 years after ice shelf retreat commenced.

Using a new high-resolution ice unloading dataset from 1966 to 2015, we simulated solid Earth deformation at three GPS sites. Comparison between the GPS observations and the model predictions argue for a higher viscosity Earth rheology in the southern AP than previously reported in the northern AP (Nield et al. 2014), suggesting a north-south gradient in viscosity, which changes by an order of magnitude over 500 km. We find horizontal velocities that, after removal of plate rotation and recent viscoelastic effects, point away from Marguerite Bay. This is suggestive of a continued response to Holocene deglaciation and hence provides further evidence of a relatively strong upper mantle compared with the northern AP where a near-instantaneous viscous response has been observed.

The specific viscoelastic properties of the southern AP still remain to be identified quantitatively, but our analysis establishes a robust lower bound. Improved Holocene ice loading history, ongoing glacier loading changes, and long-term and high-accuracy GPS time series will help resolve the remaining ambiguity in GIA modelling in this region.

Chapter 3

Basal friction of Fleming Glacier, Antarctica, Part 1 - Sensitivity of inversion to temperature and bedrock uncertainty

Chapter 3 explores the sensitivity of the basal friction coefficients of the Fleming Glacier system to initial englacial temperature assumptions, various bedrock datasets, ice front positions and ocean-pressure boundary conditions. The content of this chapter is published as Zhao et al. (2018) and is re-formatted for this thesis but otherwise presented as published in:

Zhao, C., R. M. Gladstone, R. C. Warner, M. A. King, T. Zwinger and M. Morlighem (2018). "Basal friction of Fleming Glacier, Antarctica - Part 1: Sensitivity of inversion to temperature and bedrock uncertainty." The Cryosphere **12**(8): 2637-2652.

3.1 Abstract

Many glaciers on the Antarctic Peninsula are now rapidly losing mass. Understanding the dynamics of these fast-flowing glaciers, and their potential future behavior, can be improved through ice sheet modelling studies. Inverse methods are commonly used in ice sheet models to infer the spatial distribution of a scalar basal friction coefficient, which has a large effect on the basal velocity and ice deformation. Here we use the Stokes Elmer/Ice model to simulate the Wordie Ice Shelf-Fleming Glacier system in the southern Antarctic Peninsula. With an inverse method, we infer the pattern of the basal friction coefficient from surface velocities observed in 2008. We propose a multi-cycle spin-up scheme to reduce the biases in the final inversion that result from the assumed initial englacial temperature field. This is particularly important for glaciers like the Fleming Glacier, which have areas of strongly temperature-dependent, deformational flow in the fast-flowing regions. Tests using various bed elevation datasets, ice front positions and boundary conditions demonstrate the sensitivity of inversion results to high-accuracy ice thickness/bed geometry data and precise location of the ice front boundary.

3.2 Introduction

In response to rapid changes in both atmosphere and ocean forcing, glaciers in West Antarctica (WA) and the Antarctic Peninsula (AP) have undergone rapid dynamic thinning and increased ice discharge over recent decades, which has led to a significant contribution to global sea level rise (Wouters et al. 2015, Cook et al. 2016, Gardner et al. 2018), e.g. -20 ± 15 Gt yr^{-1} for the AP and -94 ± 27 Gt yr^{-1} for the WA during 1992-2017 (Shepherd et al. 2018). Understanding the underlying physical

processes is crucial for improving predictive modelling of ice dynamics and enabling reliable predictions of contributions to sea level change, especially for fast-flowing outlet glaciers.

The high velocities of fast-flowing outlet glaciers arise from internal ice deformation, or ice sliding at the bed, or both. Internal deformation is dependent on gravitational driving stress, englacial temperature, ice anisotropy (e.g. Gagliardini et al. (2009)), and larger scale rheological factors, such as weakening from fractures (Borstad et al. 2013). Basal sliding is dependent on the gravitational driving stress, bedrock topography and the basal friction coefficient, which in turn is affected by the roughness of the bed, the presence of deformable till, or subglacial hydrology. Therefore, one of the keys to modelling fast-flowing glaciers is accurate knowledge of the basal conditions: the bedrock topography and the basal friction coefficient (Schäfer et al. 2012, Gillet-Chaulet et al. 2016). Inverse methods are commonly used in ice sheet models to infer the basal friction coefficient, basal velocities, and ice rheology from the glacier geometry and observed surface velocities (Morlighem et al. 2010, Gladstone et al. 2014, Gillet-Chaulet et al. 2016).

Poorly constrained quantities, like basal topography, and the distribution of internal temperature, have provided major challenges for modelling the basal shear stress (Vaughan and Arthern 2007). However, in studies carried out on a fast-flowing outlet glacier draining from the Vestfonna ice cap in the Arctic (Schäfer et al. 2012, Schäfer et al. 2014), it was found that the Robin inverse method did not depend strongly on the uncertainties in the topographic and velocity data. In their case, sliding dominated the flow regime, and the impact of internal deformation on ice velocity was relatively small compared to the important role of frictional heating at the bed on the basal sliding (Schäfer et al. 2012, Schäfer et al. 2014). It is unclear whether this property is specific to the Vestfonna situation or if it also applies to other fast-flowing glaciers. The motivation of this paper is twofold: to test the sensitivity of a variational inverse method (e.g., MacAyeal (1993), Morlighem et al. (2010)) for basal friction to basal geometry and to an assumed initial englacial temperature distribution for a different outlet glacier system, and to determine a robust basal friction coefficient pattern for the Fleming Glacier, located in the southern AP, in 2008.

The Wordie Ice Shelf (WIS) (Fig. 3.1b) in the southern AP has experienced ongoing retreat and collapse since 1966, with its almost-complete disappearance by 2008 (Cook and Vaughan 2010, Zhao et al. 2017). The Fleming Glacier (FG) (Fig. 3.1b), the main tributary glacier that fed the WIS, has a current length of ~80 km and is ~10 km wide near the ice front (Friedl et al. 2018). This glacier has recently shown a rapid increase in surface-lowering rates (doubling near the ice front after 2008) (Zhao et al. 2017), and the largest velocity changes (> 500 m yr^{-1} near the ice front) across the whole Antarctic ice sheet over 2008-2015 (Walker and Gardner 2017).

In this study, we employ the Elmer/Ice code (Gagliardini et al. 2013), a three-dimensional (3D), finite element, Stokes ice sheet model, to invert for the basal friction coefficient distribution over the whole WIS-FG system using a parallel

computing environment. We assess its sensitivity to assumptions about the initial temperature distribution, bedrock topographies, ocean boundary conditions and other model parameters. We introduce the data in Sec. 3.4.3, present the ice sheet model, spin-up scheme and experiment design in Sec. 3.4.4, and discuss the results in Sec. 3.4.5 presenting conclusions in Sec. 3.4.6.

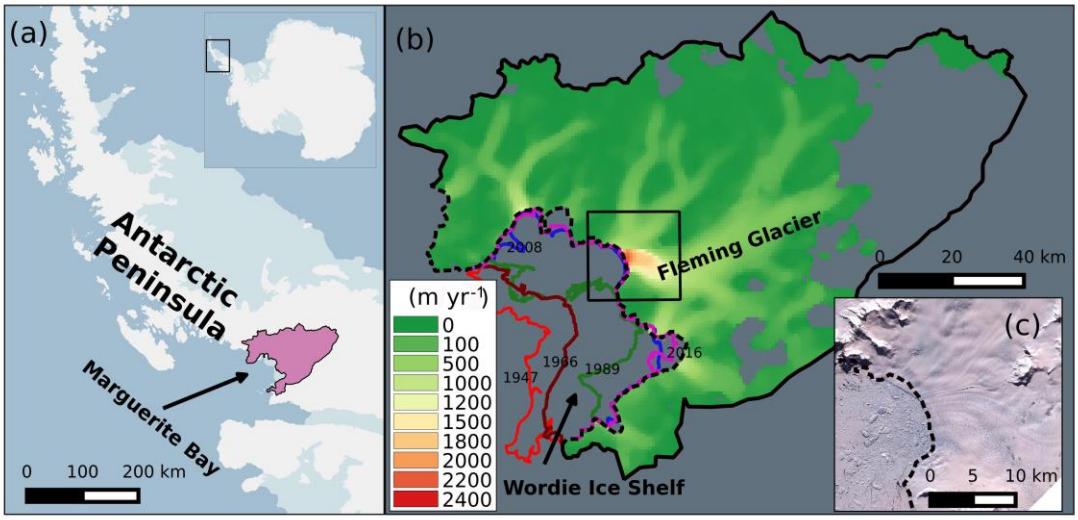

Figure 3.1. (a) The location of the Wordie Ice Shelf-Fleming Glacier system (shaded purple region) in the Antarctica Peninsula. (b) Surface speed in 2008 with a spatial resolution of 900 m obtained from InSAR data (Rignot et al. 2011c) for the study regions. Colored lines represent the ice front position in 1947 (red), 1966 (brown), 1989 (green), Apr 2008 (blue), and Jan 2016 (magenta) obtained from Cook and Vaughan (2010), Wendt et al. (2010), and Zhao et al. (2017). The grey area inside the catchment shows the region without velocity data. (c) Ice front images acquired from ASTER L1T data on Feb 2nd, 2009. The dashed line in (b) and (c) is the 1996 grounding line position (Rignot et al. 2011a).

3.3 Data

3.3.1 Surface elevation data in 2008

The surface topography in 2008 (Fig. 3.2a) is combined from two SPOT DEM products acquired on 21st Feb, 2007 (resolution: 240 m) and 10th Jan, 2008 (resolution: 40 m) (Korona et al. 2009) and an ASTER DEM product ranging from 2000 to 2009 (resolution: 100m) (Cook et al. 2012). The surface elevation data for the Fleming Glacier is mainly from the SPOT DEM product acquired on 10th Jan, 2008 (see masks of different DEM products in Fig. B1 in the Appendix B). Here we apply the SPOT DEM precision quality masks on the raw data to extract the DEM data with correlation scores from 20% to 100%. Areas with low correlation scores were filled with the ASTER DEM data. To remove noise from the DEM data, the combined DEM (resolution: 40 m) is resampled to 400 m with a median filter and a window size of 10×10 pixels.

Both SPOT and ASTER DEM products used the EGM96 geoid (Lemoine et al. 1998) as the height reference. However, the bed elevation data from Bedmap2 dataset

(Fretwell et al. 2013) adopted the EIGEN-GL04C geoid (Förste et al. 2008) as its height reference, and we chose to convert all the elevation datasets to the WGS84 ellipsoid. The EGM96 geoid (Lemoine et al. 1998) and EIGEN-GL04C geoid (Förste et al. 2008) are used to convert from the EGM96 geoid and EIGEN-GL04C geoid values to WGS84 ellipsoidal heights, respectively. Accordingly, a height of 0 m does not refer to sea level. We extract a median value of 15 m for the DEM data over Marguerite Bay (Fig. 3.1a) as the mean local sea level in the ellipsoid frame.

Both geoid-ellipsoid separation fields vary very slowly spatially compared to the surface elevation of the ice sheet, so that we do not expect any significant change in the computed surface slope that enters the driving stress calculations from mapping the geoid-based elevations into the ellipsoidal frame. Ice thickness is preserved in converting the datasets to the ellipsoid reference frame (see Sec. 3.3.2). Clearly, the sea level height in the ellipsoidal reference frame enters the calculation of ocean water pressure on the ice front explicitly, as we discuss under experimental design in Sec 3.4.6 and Sec. 3.5.4.

3.3.2 Bed elevation data

The bed topography plays an important role in basal sliding and the distribution of fast-flowing ice (e.g., De Rydt et al. (2013)). However, high-resolution observations of bedrock elevation for the WIS-FG system are currently not available. To explore the sensitivity of the basal friction coefficient distribution to the uncertainty in the bedrock topography, we test three basal topographies. The first is from the Bedmap2 dataset (Fretwell et al. 2013) with a resolution of 1 km (hereafter bed_bm; Fig. 3.2b), which is converted from the EIGEN-GL04C geoid (Förste et al. 2008) to WGS84 ellipsoid heights. The other two are derived using the equations below:

$$\text{bed\_zc} = S_{2008} - H_{mc} \quad (3.1)$$

$$\text{bed\_mc} = S_{bm} - H_{mc} \quad (3.2)$$

where S_{2008} is the 2008 surface DEM described in Sec. 2.1, and S_{bm} is the surface elevation data from Bedmap2 (Fretwell et al. 2013), again relative to the WGS84 ellipsoid. S_{bm} is downscaled to 500 m with a bilinear interpolation method. H_{mc} (where "mc" refers to "mass conservation") is the ice thickness data with a resolution of 450 m covering three regions shown in Fig. 3.2e. H_{mc} for the yellow area is computed using the Ice Sheet System Model's mass conservation method (Morlighem et al. 2011, Morlighem et al. 2013), based on ice thickness measurements from the Center for Remote Sensing of Ice Sheets (CReSIS), using ice surface velocities in 2008 from Rignot et al. (2011b), surface accumulation from RACMO 2.3 (van Wessem et al. 2016) and 2002-2008 ice thinning rates (see Chapter 2). The mass conservation method infers ice thickness using the mass continuity equation with the assumption that ice is incompressible (Morlighem et al. 2011, Morlighem et al. 2013). The thickness data for the grey area is interpolated from Bedmap2 (Fretwell et al. 2013), while the data in the red area is interpolated from the grey and yellow regions. The yellow area indicates the Fleming Glacier system with ice velocity >100 m yr^{-1}.

The uncertainty of H_{mc} (Fig. 3.2f) ranges from 10 m to 108 m. For the calculation of H_{mc}, we assume that the ice elevation changes over 2002 to 2008 (Zhao et al. 2017) were small compared to the uncertainties in ice thickness (Fig. 3.2f) and could be ignored in the ice thickness measurements, which span a wider time frame. Both bed_mc (Fig. 3.2c) and bed_zc (Fig. 3.2d) have a higher resolution of 450 m while bed_bm (Fig. 3.2b) has a resolution of 1 km. The uncertainty of bed_bm for the fast-flowing regions of the Fleming Glacier (yellow and red area in Fig. 3.2e) ranges from 151 m to 322 m (Fretwell et al. 2013), while the uncertainty of bed_mc and bed_zc ranges from 10 m to 108 m (from uncertainties in H_{mc}).

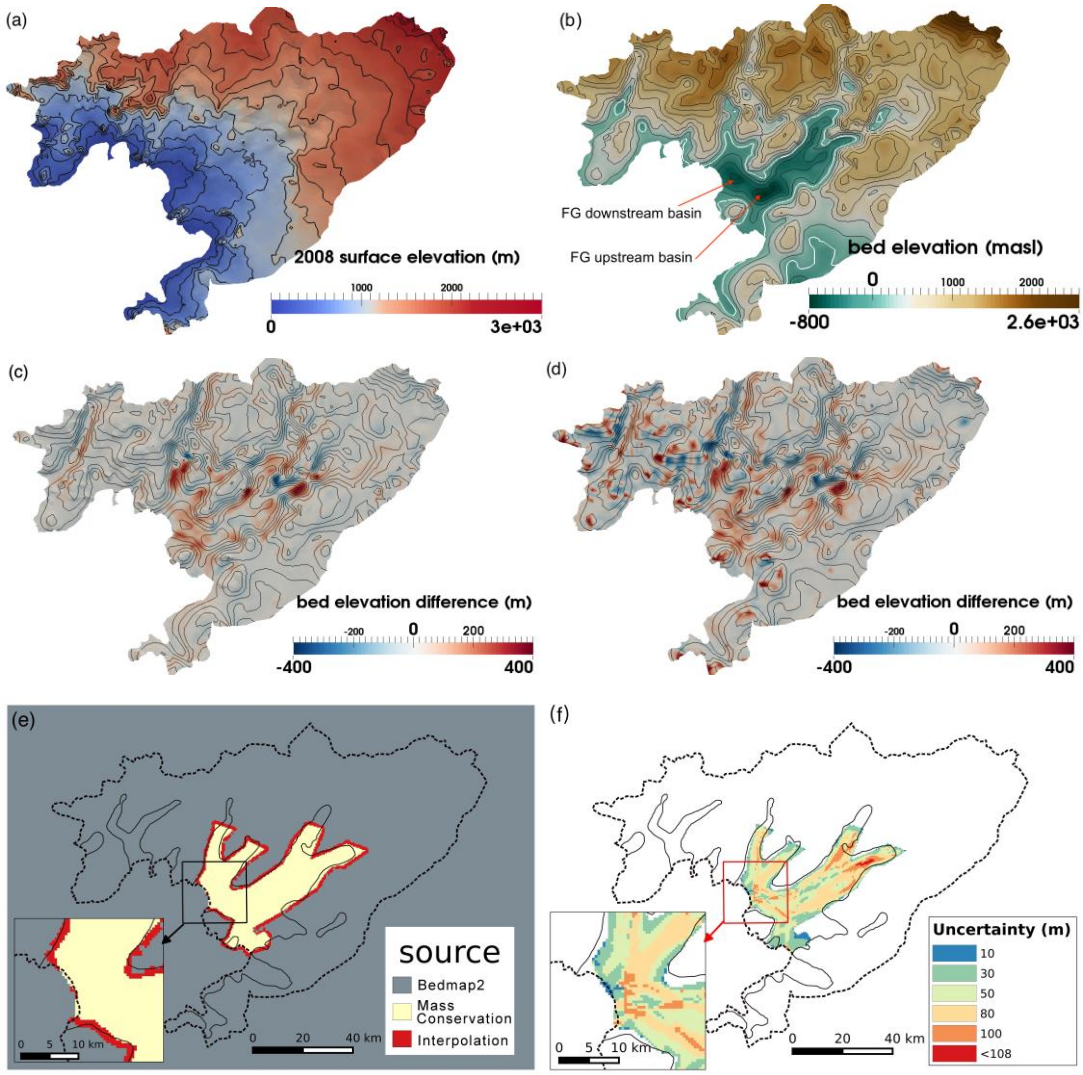

Figure 3.2. (a) Surface elevation data in 2008 with black contours (interval: 200 m) representing the surface elevation. (b) bed elevation data from bed_bm (metres above sea level, masl), (c) elevation difference between bed_mc and bed_bm (d) elevation difference between bed_zc and bed_bm. The black contours in (b-d) show the bed elevation, bed_bm, with an interval of 200 m. (e) The ice thickness data sources and (f) the uncertainty of the ice thickness data H_{mc} with black solid lines representing the observed ice surface velocity of 100 m yr^{-1}.

The bed topography data (Fig. 3.2b) indicates the essentially marine character of the Fleming Glacier, showing two basins featuring retrograde slopes, both located

underneath the main trunk of the Fleming Glacier's fast flow region. The basin further upstream (hereafter "FG upstream basin") has a steeper retrograde slope than the one closer to the grounding line (hereafter "FG downstream basin"). For the FG downstream basin, elevation differences between bed_bm and the other two datasets (Figs 3.2c, 3.2d) show that bed_bm has a generally steeper retrograde slope. The sensitivity of basal friction coefficient distributions to the three bed datasets is discussed in Sec. 3.5.2.

3.3.3 Surface velocity data in 2008

The surface velocity data used for 2008 (Fig. 3.1b) were obtained from MEaSUREs InSAR-based Antarctic ice velocity (from the fall 2007 and/or 2008) produced by Rignot et al. (2011b) (version 1.0) with a resolution of 900 m and with uncertainties ranging from 4 m yr^{-1} to 8 m yr^{-1} over the study area. For the regions without data (grey area in Fig. 3.1b), we prescribe the surface speed to be 0. We do not use the finer (450 m) resolution MEaSUREs velocity here since the coarser (900 m) resolution data have been subjected to some post-processing, including smoothing and error corrections.

3.4 Method

All the simulations are carried out using the Elmer/Ice model (Gagliardini et al. 2013). These simulations solve the ice momentum balance equations with an inverse method to determine the basal friction coefficients by minimizing the mismatch between magnitudes of modelled and observed surface velocities, and using the steady state heat equation to model the ice temperature distribution. The ice rheology is given by Glen's flow relation (Glen 1955):

$$\boldsymbol{\tau} = 2\eta\dot{\boldsymbol{\varepsilon}} \tag{3.3}$$

where $\boldsymbol{\tau}$ is the deviatoric stress tensor and $\dot{\boldsymbol{\varepsilon}}$ is the strain rate tensor. The non-linear, "effective" viscosity η is computed as:

$$\eta = \frac{1}{2}(EA)^{-1/n}\dot{\varepsilon}_e^{(1-n)/n} \tag{3.4}$$

where E is an overall flow enhancement factor, A is a temperature-dependent rate factor calculated using an Arrhenius equation (Gagliardini et al. 2013), $\dot{\varepsilon}_e = \sqrt{tr(\dot{\varepsilon}^2)/2}$ is the effective strain rate, and n is the exponent in Glen's flow law. Table 3.1 lists the parameters used in this study.

3.4.1 Mesh generation and refinement

We use GMSH (Geuzaine and Remacle 2009) to generate an initial 2-D horizontal mesh with the boundary defined from the grounding line data in 1996 (Rignot et al. 2011a) and the catchment boundary of the feeding glacier system (Cook et al. 2014), with the assumption that the ice front position in 2008 coincided with the grounding line position in 1996 (Rignot et al. 2011a). This assumption is tested as part of the sensitivity tests to various ice front positions.

Table 3.1. List of parameter values used in this study.

Parameters	Symbol	Values	Units
Rheological parameter in the Arrhenius law	A_0 (T < -10 ℃)	3.985×10^{-13}	$Pa^{-3}\ s^{-1}$
	A_0 (T > -10 ℃)	1.916×10^{3}	$Pa^{-3}\ s^{-1}$
Activation energy in the Arrhenius law	Q_0 (T < -10 ℃)	-60	kJ mol^{-1}
	Q_0 (T > -10 ℃)	-139	kJ mol^{-1}
Gravitational constant	g	9.8	m s^{-2}
Exponent of Glen flow law	n	3	
Density of ocean water	ρ_w	1025	kg m^{-3}
Density of ice	ρ_i	900	kg m^{-3}

To reduce computational cost without reducing accuracy, we refine the mesh with the anisotropic mesh adaptation software YAMS (Frey and Alauzet 2005) using the local Hessian matrix (second derivatives) of the surface velocity data in 2008 from Rignot et al. (2011c) as a metric for the mesh density. The resulting mesh is shown in Fig. 3.3 and has minimum and maximum element sizes of approximately 250 m and 4 km, respectively. The 2-D mesh is then vertically extruded using 10 equally spaced, terrain following layers. Sensitivity tests have been done on the Vestfonna ice cap (Schäfer et al. 2012, Schäfer et al. 2014) to demonstrate the robustness of inverse simulations to the vertical mesh resolution. In the current study an experiment with 20 extruded layers (not shown) gives very similar results as with 10 layers, confirming those findings also apply to the WIS-FG system. Experiments with various horizontal resolutions (1 km, 500 m, 250 m, and 125 m) show that a minimum resolution of 250 m is sufficient for simulations of the WIS-FG system.

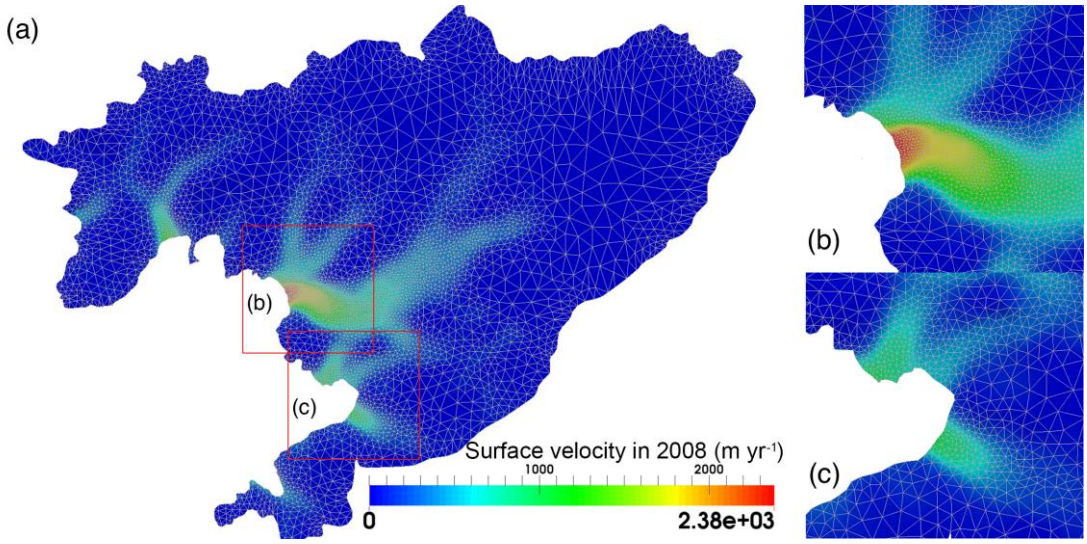

Figure 3.3. (a) Mesh structure of the domain in the current study with surface velocity in 2008 (Rignot et al. 2011c) and the zoomed-in map for (b) the Fleming Glacier and (c) the Prospect Glacier.

3.4.2 Boundary Conditions

For transient simulations (surface relaxation, see Sec. 3.4.3), the stress-free upper surface is allowed to evolve freely, with a minimum imposed ice thickness of 10 m over otherwise ice-free terrain. For inverse and temperature simulations, the upper surface height and temperature are fixed.

The surface temperature is defined by the yearly averaged surface temperature over 1979-2014 computed from the regional atmospheric climate model RACMO2.3/ANT27 (van Wessem et al. 2014). The geothermal heat flux (GHF) at the bed is specified from Fox Maule et al. (2005) using input data from the SeaRISE project, and the GHF is interpolated with bilinear interpolation method from the standard 5 km grid onto the mesh. A basal heat flux boundary condition combining GHF and basal friction heating is imposed for temperature simulations.

At the ice front, the normal component of the stress is set equal to the hydrostatic water pressure exerted by the ocean where the ice is below sea level. We discuss the sensitivity to the ice front boundary condition in Sec. 3.5.4. On the lateral boundary, which falls within glaciated regions, the normal component of the stress vector is set equal to the hydrostatic ice pressure exerted by the neighboring glacier ice and the tangential velocity is assumed to be zero.

The bedrock is regarded as rigid, impenetrable, and temporally fixed in all simulations. The present-day solid Earth deformation rate in the Fleming glacier region (Zhao et al. 2017) is negligible compared to the uncertainty of the bedrock data. Assuming that basal melt contribution to the vertical velocity and stress balance is negligible under grounded ice, the normal basal velocity is set zero at the ice/bed interface. The sliding relation relates the basal sliding velocity $\boldsymbol{u_b}$ to basal shear stress $\boldsymbol{\tau_b}$. Considering that in this diagnostic study the sliding law is only used as a numerically convenient tool for calculating the basal shear stress, a simple linear sliding law following Gillet-Chaulet et al. (2012), Gagliardini et al. (2013) is applied on the bottom surface:

$$\boldsymbol{\tau_b} = -C\boldsymbol{u_b} \tag{3.5}$$

where C, the basal friction coefficient, is used as the adjustable parameter in the inversion scheme described below. During the initial surface relaxation, and at the start of the inversion, C is initialized to a constant value of 10^{-4} MPa m^{-1} yr (following Gillet-Chaulet et al. (2012)), which is replaced with the inverted values of C in subsequent steps.

3.4.3 Surface relaxation

There may be non-physical "spikes" in the initial surface geometry, caused for example by observational uncertainties of the surface or bedrock data and/or by the resolution discrepancy between mesh and geometry data. To reduce these features, we relax the free surface of this domain during a short transient simulation of 0.2 yr length with a timestep of 0.01 yr. This is long enough to remove the non-physical

spikes, but too short to significantly modify the geometry of the fast-flowing regions of the Fleming Glacier.

3.4.4 Inversion for basalfriction coefficient

After the surface relaxation, we use a variational inverse method (MacAyeal 1993, Morlighem et al. 2010) implemented in Elmer/Ice (Gillet-Chaulet et al. 2012, Gagliardini et al. 2013) to constrain the basal friction coefficient *C* in Eq. (3.5). To avoid non-physical negative values, we use a logarithmic representation of the basal friction coefficient, $C = 10^{\beta}$, where β can take any real value.

The inverse method is based on adjusting the spatial distribution of the basal friction coefficient to minimize a cost function that represents the mismatch between the magnitudes of the simulated and observed surface velocities:

$$J_0 = \int_{\Gamma_s} \frac{1}{2} (|\boldsymbol{u}| - |\boldsymbol{u}^{obs}|)^2 d\Gamma \tag{3.6}$$

where Γ_s is the upper surface of the domain, and $\boldsymbol{u}$ and $\boldsymbol{u}^{obs}$ are the simulated and observed surface velocities, respectively. We do not try to fit velocity directions.

To avoid over-fitting of the inversion solution to non-physical noise in the observations, a regularization term J_{reg} is added to the cost function imposing an additional cost on spatial variations in the control parameter β:

$$J_{reg} = \frac{1}{2} \int_{\Gamma_b} \left(\frac{\partial \beta}{\partial x}\right)^2 + \left(\frac{\partial \beta}{\partial x}\right)^2 \tag{3.7}$$

The total coast function is now written as:

$$J_{tot} = J_0 + \lambda J_{reg} \tag{3.8}$$

where λ is a positive regularization weighting parameter, and J_{tot} is the total cost (following for example Gillet-Chaulet et al. (2012)). Thus, the minimum of this cost function is no longer the best fit to observation but a compromise between fit to observation and smoothness in β. An L-curve analysis (Hansen 2001) has been carried out for inversions in the current study to find the optimal value of λ by plotting the term J_{reg} as the function of J_0 (Fig. B2 in Appendix B). The optimal value of 10^8 is chosen for λ to minimize J_0.

3.4.5 Steady-state temperature simulations

In the absence of a known englacial temperature distribution for the Fleming Glacier system, the steady state heat transfer equation is solved using an iterative method as described in Gagliardini et al. (2013) to provide temperatures for use in the inversion process, since the temperature affect the ice rheology, i.e. the ice internal deformation rate via *A* in Eq. 3.4 . The ice velocity and geometry are held constant for this part of the simulation. Steady-state temperature simulations for a non-steady-state glacier system will result in estimations of temperatures that deviate from reality. Similar experiments on the Greenland Ice Sheet indicated that the simulated steady-state

temperature field could provide a reasonable thermal regime for calculation of basal conditions (Seroussi et al. 2013).

3.4.6 Experiment design

Gong et al (2017) adopted a four-step spin-up scheme (Gladstone et al., 2014) in inverse modelling using Elmer/Ice (Gagliardini et al. 2013), but without testing the effect of assumptions about the initial englacial temperature distribution on the inversion results. To explore the sensitivity of inverse modelling to initial temperature assumptions, we proposed a spin-up scheme with more cycles (three cycles in this study as presented in Fig. 3.4). For each cycle, we followed the spin-up scheme from Gladstone et al. (2014):

1. surface relaxation;
2. inversion of the basal friction coefficient using the relaxed surface geometry;
3. a steady state temperature simulation using the simulated velocities from that inversion;
4. another inversion with the previously obtained steady-state temperature.

The surface relaxation for each cycle starts from the same initial geometry described in Sec. 3.4.3. For cycle 1, the surface relaxation and first inversion are implemented with an initial temperature assumption (described below) and uniform basal friction coefficient of 10^{-4} MPa m^{-1} a (following Gillet-Chaulet et al. (2012)). For cycles 2 and 3, the surface relaxation and inversion are initiated with the simulated steady-state temperature and an initial distribution of basal friction coefficient $\boldsymbol{C}$ from the final state of the previous cycle.

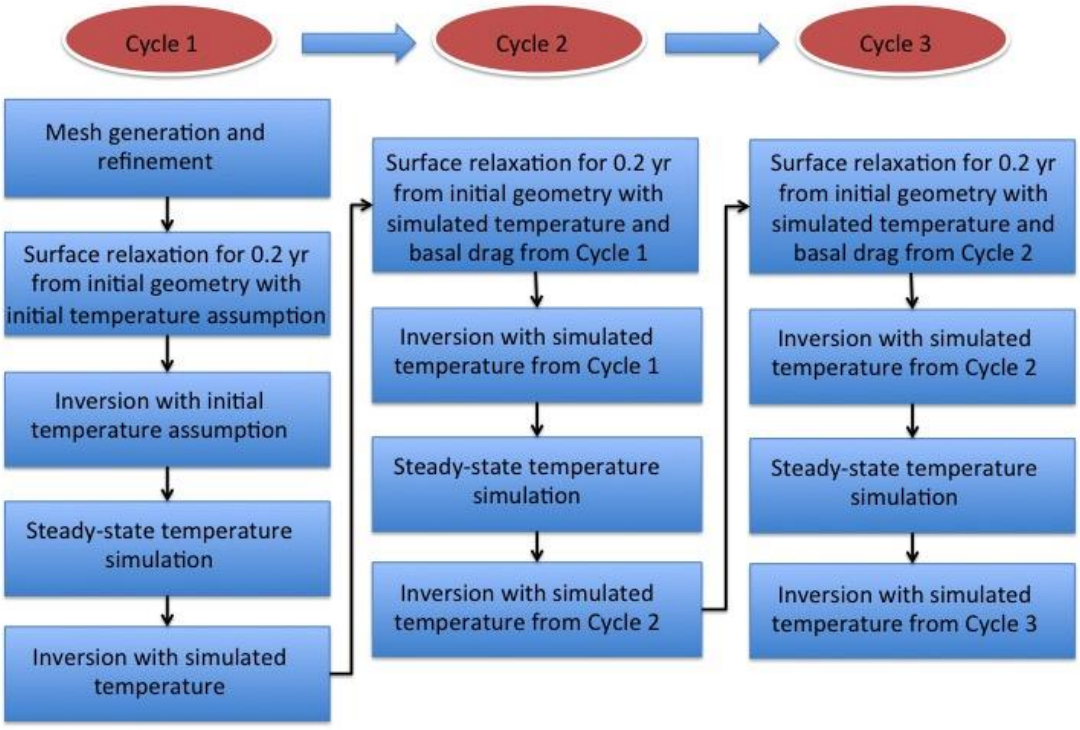

Figure 3.4. Flow chart of simulation spin-up with three cycles.

To explore the sensitivity of our inverse method to assumed initial englacial temperature distribution, enhancement factor (E), basal topography, ice front positions, and the ice front boundary conditions, we carry out the experiments summarized in Table 3.2.

Table 3.2 Experiment lists. n/a is short for "not applicable". EF and SL are short for "enhancement factor" and "sea level", respectively. IF1 and IF2 represent the ice front positions located downstream and upstream of the 1996 grounding line position (Rignot et al. 2011a), respectively. RMSD is the root mean square deviation between the observed and simulated surface speed for the fast-flowing region of the Fleming Glacier (> 1500 m yr^{-1}) after the third cycle.

Experiment	EF	Bed topography used	Initial temperature in surface relaxation of Cycle 1	Initial temperature in first inversion of Cycle 1	SL	Ice front position	RMSD (m yr^{-1})
CTRL	1.0	bed_bm	Linear temperature	Linear temperature	15 m	GL1996	75.12
TEMP1	1.0	bed_bm	-20 ℃	-20 ℃	15 m	GL1996	80.65
TEMP2	1.0	bed_bm	-5 ℃	-5 ℃	15 m	GL1996	78.07
TEMP3	1.0	bed_bm	-20 ℃	Linear temperature	15 m	GL1996	78.48
EF1	0.5	bed_bm	Linear temperature	Linear temperature	15 m	GL1996	86.35
EF2	2.0	bed_bm	Linear temperature	Linear temperature	15 m	GL1996	89.38
EF3	4.0	bed_bm	Linear temperature	Linear temperature	15 m	GL1996	993.20
BEDZC	1.0	bed_zc	Linear temperature	Linear temperature	15 m	GL1996	62.60
BEDMC	1.0	bed_mc	Linear temperature	Linear temperature	15 m	GL1996	61.78
IFP1	1.0	bed_bm	Linear temperature	Linear temperature	15 m	IF1	72.10
IFP2	1.0	bed_bm	Linear temperature	Linear temperature	15 m	IF2	75.12
IFBC1	1.0	bed_bm	Linear temperature	Linear temperature	5 m	GL1996	79.38
IFBC2	1.0	bed_bm	Linear temperature	Linear temperature	25 m	GL1996	72.68
IFBC3	1.0	bed_bm	Linear temperature	Linear temperature	n/a	GL1996	249.64

An assumed initial englacial temperature distribution is used in the first cycle of the scheme above and would affect the surface relaxation, the modelled ice deformation and the ice velocity field, especially for fast-flowing regions, and consequently affect the steady-state temperature calculation, which might affect the subsequent inversion

process. To explore the impact of initial temperatures on inversion results with the three-cycle spin-up scheme, we propose experiments with different initial temperature assumptions for the surface relaxation and initial inversion in Cycle 1. TEMP1: a uniform temperature of -20 ℃; TEMP2: a uniform temperature of -5 ℃; CTRL: a linearly increasing temperature from the upper surface values (see also Sec. 3.4.2) to the pressure melting temperature at the bed. To test the sensitivity of basal friction to the relaxed geometry, we also add another experiment - TEMP3: surface relaxation in the first cycle using the linear temperature, followed by inversion with a uniform temperature of -20 ℃. Experiments TEMP1, TEMP2 and TEMP3 differ from CTRL only in the temperature fields imposed before the first temperature simulation.

Ma et al. (2010) tested the influence of ice anisotropy on the ice flow through various enhancement factors, and found that appropriate *E*-values for the grounded ice are usually >1.0. To find out the most appropriate value of *E* (in Eq. 3.4) in this study, we evaluate inversion carried out with different values of *E* (EF1: E = 0.5, CTRL: E = 1.0, EF2: E = 2.0, EF3: E = 4.0; Table 3.2). Experiments EF1, EF2 and EF3 differ from CTRL only in terms of the value used for *E*.

As described in Sec. 3.3.2, we generate three different bed topography datasets to explore the sensitivity of the inverse modelling. The three-cycle spin-up scheme is carried out for each bed dataset using the linear initial temperature distribution described above. These experiments are referred to as CTRL, BEDZC, and BEDMC (Table 3.2). Experiments BEDZC and BEDMC differ from CTRL only in terms of the bedrock data set used.

In our standard model domain we assume the 2008 ice front is coincident with the 1996 grounding line, which has an error of several km on fast-moving ice (Rignot et al. 2011a) and might have changed since 1996. The frontal surface elevation is from the SPOT DEM data in Jan 2008, which shows the ice front position is ~1.5 km downstream of the 1996 grounding line position. Since such a narrow residual ice shelf is considered unlikely to have a major influence, we construct the model geometry to have the ice front coincide with the 1996 grounding line for simplicity, i.e. all ice is considered grounded. To test the sensitivity of inverse modelling to the ice front positions, we implement two further scenarios with different ice front positions: downstream (experiment IFP1) and upstream (experiment IFP2) of the 1996 grounding line position (CTRL). In IFP1, we assume the ice front position is coincident with the frontal boundary of SPOT DEM data (~1.5 km downstream). In IFP2, we artificially put the ice front position ~1.5 km upstream of the 1996 grounding line position for ~1.5 km. IFP1 and IFP2 differ from CTRL only in their ice front position.

In addition to the ice front position, there are other sources of uncertainty in the vicinity of the ice front: ice thickness, bedrock depth, height conversion from geoid to ellipsoid, and backstress due to the presence of ice mélange. These uncertainties have an effect on the pressure boundary condition applied to the ice front, which conventionally balances the normal stress in the ice against ocean water pressure. In

view of the ice thickness uncertainty (ranging from 10 m to 100 m) and hence bedrock depth around the grounding line, and given the possibility of increased additional buttressing force due to floating icebergs and ice mélange as indicated in many previous studies (e.g. Amundson et al. (2010), Todd and Christoffersen (2014), Krug et al. (2015), Robel (2017), Walter et al. (2017)) and clearly seen in Fig. 3.1c, we adopt a heuristic approach to investigating the sensitivity to uncertainty in the ocean pressure boundary condition by varying the sea level used to calculate ocean water pressure. This approach represents some small uncertainty in the actual sea level, but is also a proxy for pressure variations due to bedrock elevation/ice thickness uncertainty and mélange back stress. First in the CTRL experiment, we assume an ocean pressure at the ice front computed using the observed sea level of 15 m, as mentioned in Sec. 3.3.1. We further simulate two alternative scenarios for the sea level used in the simulations to calculate ocean pressure: IFBC1 with a sea level of 5 m and IFBC2 with a sea level of 25 m. Another extreme scenario (IFBC3, Table 3.2) is adopted here by setting the ice front pressure to the ice overburden:

$$P_i(z) = \rho_i g(z_s - z) \tag{3.9}$$

where $P_i(z)$ is the pressure at the ice front as a function of height z, ρ_i is ice density (Table 3.1), g is the gravitational constant (Table 3.1), and z_s is the height of ice upper surface at the ice front. This is the pressure that would be imposed by a hypothetical undeforming continuation of the advancing glacier, and imposes zero normal strain rate at the ice front. The ice surface elevation z_s at the front is ~115 m, approximately 100 m above actual sea level. The total vertically integrated pressure imposed by this condition is equivalent to a sea level of ~60 m, although the vertical distribution of pressure differs from an ocean pressure condition. Experiments IFBC1, IFBC2 and IFBC3 differ from CTRL only in their ice front boundary condition.

3.5 Results and discussions

The main focus of the current study is the sensitivity of the inversion to the variations of five factors: temperature initialization, enhancement factor, bed topography, ice front positions, and ice front oceanic pressure boundary condition. The evaluation criteria are the robustness of simulated basal friction coefficient distribution to experiment design and the mismatch between the simulated and observed surface velocities.

3.5.1 Sensitivity to initial temperature

We present the results for the inferred basal friction coefficients from the CTRL and three TEMP experiments (Sec. 3.4.6, Table 3.2) for the WIS-FG system in Fig. 3.5. The 2008 ice velocity contours are added as visual references for comparing the basal friction coefficient patterns in the regions of fast flow, since the largest observed ice velocity changes occurred in fast-flowing outlet regions (Mouginot et al. 2014, Walker and Gardner 2017).

In each cycle, the root-mean-square deviation (RMSD, sometimes also called root-mean-square error) between the relaxed and the observed surface was < 25 m (see Table B1 in the Appendix B), smaller than the ice thickness uncertainty (> 50 m) used in this study. However, the systematic changes generated at the ice front during the surface relaxation may have an effect on the inversion, and this is further discussed in Sec. 3.5.4.

After the first cycle (left column, Fig. 3.5), results showed different patterns of basal friction coefficient for each experiment, especially in the fast-flowing regions with surface velocity exceeding 1000 m yr^{-1} (yellow contour in Fig. 3.5). The basal friction coefficients from TEMP2 (Fig. 3.5g) and CTRL (Fig. 3.5a) share similar sticky spots around the ice front, and some isolated sticky spots ~3-5 km upstream of the ice front, but TEMP1 (Fig. 3.5d) and TEMP3 (Fig. 3.5j) display different patterns, indicating dependence on the initial temperature assumption. The RMSDs of key properties are computed to evaluate the consistency of these experiments (Table 3.2, B2-B5).

To reduce the dependence on initial temperature and achieve a consistent equilibrium thermal regime with respect to the given friction coefficient distribution, we carried out the second cycle shown in Fig. 3.4. The basal friction coefficients from the final step of Cycle 2 (the middle column in Fig. 3.5) show greater similarity across all the temperature experiments. However, for experiments CTRL and TEMP2, the isolated sticky points ~3-5 km upstream of the ice front (with horizontal scale around ~1 km and peak basal friction coefficient of around 6×10^{-5} MPa m^{-1} yr) mostly decrease or disappear from the first cycle (Figs. 3.5a, 3.5g) to the second cycle (Figs. 3.5b, 3.5h). Therefore, a third cycle was implemented to test whether a two-cycle spin-up scheme was enough to reduce the dependence on the initial temperature assumptions. After the third cycle, all the scenarios depicted a similar basal friction coefficient pattern (right column in Fig. 3.5). These differences in basal friction coefficients between the TEMP simulations can also be analyzed through Table B2 and Fig. B4. While these statistics and visualizations confirm the similarity between CTRL, TEMP2 and TEMP3, it is evident that TEMP1 still shows notable differences to these simulations, even after three cycles (see also Table B3 for basal velocity RMSD). The CTRL simulation, starting with a linear interpolation of temperature from upper to lower surfaces, seems to be the best option for several reasons: the choice of temperature value for upper and lower surfaces is physically motivated, which is not true for the other assumptions; it shows the lowest RMSD between simulated and observed upper surface velocity of the temperature sensitivity simulations (Table 3.2); and it shows the least change in the temperature distribution over the three cycles (Table B4). Given this choice of preferred temperature initialization (CTRL), and the significant difference between this and the cold initialization (TEMP1), we argue that TEMP1 likely deviates furthest from an ideal temperature initialization, and that such a large initial deviation would require more than three cycles to converge on a basal friction coefficient distribution. In other words, we postulate that the three cycles are likely sufficient to provide a robust inversion only for initial temperatures moderately close to reality, with the linear interpolation in the vertical providing the most appropriate

initial guess amongst our tests. Hence, we adopted the scenario with initial linear temperature for the experiments described hereafter.

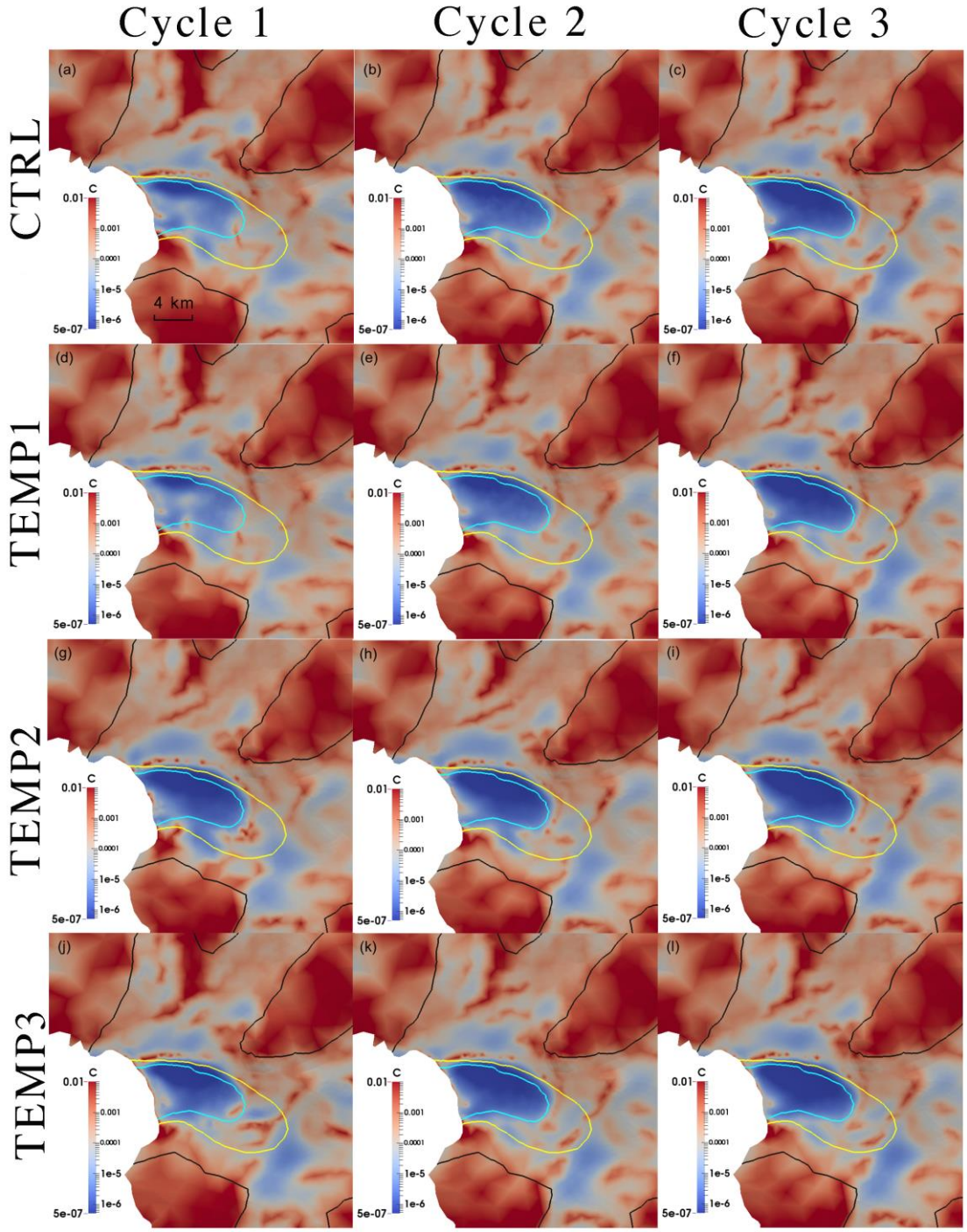

Figure 3.5. Basal friction coefficient ***C*** (MPa m^{-1} yr) inferred from experiments: (a-c) CTRL (first row), (d-f) TEMP1 (second row), (g-i) TEMP2 (third row), and (j-l) TEMP3 (fourth row). The left (a, d, g, j), middle (b, e, h, k) and right columns (c, f, i, l) are the inferred basal friction coefficients from Cycle 1, Cycle 2 and Cycle 3, respectively. The black, yellow, and cyan solid lines represent observed surface speed contours of 100 m yr^{-1}, 1000 m yr^{-1} and 1500 m yr^{-1}, respectively.

The present study is focused on exploring the effects of uncertainties and their impact, while the dynamics of the FG system will be discussed in more detail in Chapter 4.

However, a few comments are in order regarding the contrast with an earlier study on the Vestfonna ice cap. The low impact of temperature profile on the basal friction coefficient distribution in that study was due to a lower contribution of ice deformational motion compared to basal sliding (Schäfer et al. 2012). Internal ice deformation, and hence temperature, may be especially important for the WIS-FG system due to steep surface slopes and corresponding high driving stresses in the region between the downstream and upstream basins (~8-12 km upstream of the ice front in Fig. B5a). The patterns of basal friction coefficient (right column of Fig. 3.5) all indicate substantial spatial variation in basal friction over the fast-flowing part of the FG. For example, in the region flowing faster than 1000 m yr^{-1} (inside the yellow contour), we see very low friction over the downstream basin, but higher friction coefficients over the upstream bedrock high, and in a narrow band along the ice front. A comparison between the simulated basal and surface velocities (Fig. B5b) shows that vertical shear dominates the ice dynamics in the region of high slope between the downstream and upstream basins, where the driving stress is relatively high. This alone would suggest a high sensitivity of modelled sliding velocity and basal friction to the englacial temperature.

The multi-cycle iterative spin-up scheme is suggested as an effective set-up for inverse modelling of fast-flowing glaciers that have high surface slopes and vertical shear strain rates and therefore are sensitive to the internal vertical ice temperature distribution. In the present application to the Fleming system, three cycles were sufficient, except in the case of an unphysically cold initialization. In other cases, the inversion process is not so heavily dependent on the temperature field, for example for reproducing the shear margins of the outlet glacier of Basin 3 on Austfonna ice cap, Svalbard (Gladstone et al. 2014).

3.5.2 Sensitivity to enhancement factor

Sensitivity of inverse modelling to the flow enhancement factor has been explored by experiments EF1-3 and the results (after the three-cycle procedure) are shown in Fig. 3.6. The simulated basal friction coefficients (left column in Fig. 3.6) show different patterns with different E values. Recall that from Eq. (3.4), smaller E means higher ice viscosity. The local high friction coefficient sticky spots near the ice front expanded both upstream and along the ice front with increased E values, forming a band across the ice front for E = 4.0 (EF3). Conversely, inversions with smaller E give a better-simulated surface velocity at the ice front (middle column in Fig. 3.6), and also lead to smaller differences between the observed and relaxed surface elevation after the surface relaxation (right column in Fig. 3.6), whereas for EF3 the surface relaxation generates a considerable steepening of the surface slope towards the ice front (Fig. 3.6l). However, the computed RMSD of the surface velocity mismatch for the fast-flowing regions (> 1500 m yr^{-1}, middle column in Fig. 3.6 and Table B5) indicates that the experiment EF1 (E = 0.5) (Fig. 3.6e) shows greater underestimation of surface velocity than CTRL (Fig. 3.6f). Therefore, the optimal value of E = 1.0 is chosen as the most suitable enhancement factor for the Fleming

system.

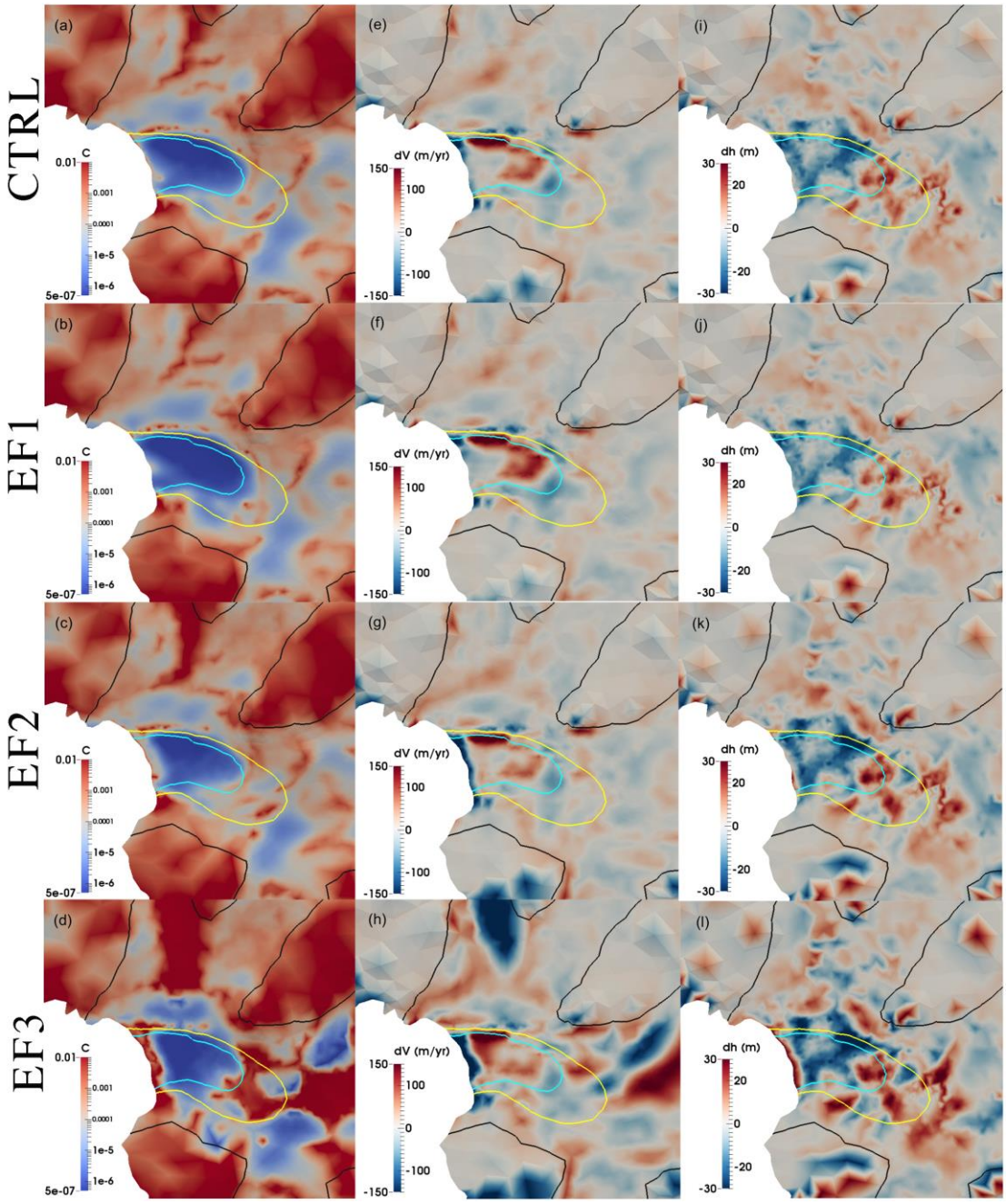

Figure 3.6. Distribution of basal friction coefficient ***C*** (MPa m^{-1} yr) (left column), mismatch between the observed and modeled surface velocity (observed minus simulated; middle column), and the difference between the observed initial surface and relaxed surface elevation (observed minus relaxed; right column) from experiments: (a, e, i) CTRL (first row), (b, f, j) EF1 (second row), (c, g, k) EF2 (third row), and (d, h, l) EF3 (fourth row). The black, yellow and cyan solid lines represent observed surface speed contours of 100 m yr^{-1}, 1000 m yr^{-1}, and 1500 m yr^{-1}, respectively.

3.5.3 Sensitivity to bedrock topography

Figure B6 summarizes results from the three experiments using different bed topographies (Sec. 3.4.6, Table 3.2). As shown in Fig. B6, the simulated basal friction

coefficient *C* varies slightly with bedrock geometry and its distribution shows greater similarity between BEDZC and BEDMC, compared with CTRL. CTRL (using Bedmap2 bedrock data; Fig. B6a) shows slightly smaller basal friction coefficients than BEDMC (Fig. B6b) and BEDZC (Fig. B6c) in the fast-flowing region (>1500 m yr^{-1}, cyan contour in Fig. B6). The pattern in the region between the 1000 and 1500 m yr^{-1} contours also differs compared to the CTRL case, which might be caused by the deeper bedrock of Bedmap2 in this region (Fig. B6g), compared to the other two datasets (Figs. B6h, B6i). However, all three cases feature a low basal friction coefficient in fast flow regions (>1500 m yr^{-1} in Fig. B6), which is approximately coincident with the FG downstream basin.

The simulated surface velocities from BEDZC (Fig. B6e) and BEDMC (Fig. B6f) match the observed surface velocities better than those from CTRL (Fig. B6d) in the regions around the ice front and more broadly for velocity exceeding 1000 m yr^{-1}. This point is supported by the computed RMSD of surface velocity mismatches (Table 3.2). One possible cause of the different basal friction coefficient distributions in these inversions might be the changed surface topography during the surface relaxation, especially near the ice front (Figs. B6).

Comparisons of the distributions of velocity mismatch and of $\boldsymbol{C}$ between BEDZC and BEDMC do not provide direct insight into which is the more accurate basal geometry for modelling the Fleming system. The computed RMSD of the velocity mismatch for the regions with velocity >1500 m yr^{-1} (Table 3.2) is only slightly higher for BEDMC (62.60 m yr^{-1}) than for BEDZC (61.78 m yr^{-1}), and both are much lower than CTRL. Both BEDMC and BEDZC use the 2008 surface DEM and this improvement over the Bedmap2 surface DEM in CTRL appears significant, even before turning to the matter of ice thickness. Both cases use the ice thickness extracted using the mass conservation approach (which is independent of surface geometry) and the bed geometries are accordingly more similar to each other than they are to CTRL (see Fig. 3.2 b-d). However, BEDZC maintains better internal consistency with the 2008 surface elevation, since it results in the mass conserving ice thickness H_{mc} being employed, whereas, by the construction of bed_mc (Eq. 3.2), the ice thickness in BEDMC is not entirely consistent with mass conservation, although still a more physically motivated interpolation than bed_bm in CTRL. The BEDMC and BEDZC ice thicknesses clearly differ by the difference between the Bedmap2 and 2008 DEMs, which should be greatest in areas of greatest lowering, and as we see BEDMC provides a useful sensitivity test case. Since bed_zc is extracted from the accurate and contemporary DEM2008, it should also incorporate into the bed geometry (via H_{mc}) more detail from the then current surface, compared to bed_mc, extracted from Bedmap2's surface DEM, which was generated from datasets obtained over a longer time range. Therefore, bed_zc is suggested as the best current bedrock elevation data for further ice sheet modelling of the WIS-FG system.

3.5.4 Sensitivity to ice front position and boundary condition

All the inversions presented so far feature some sticky spots with high basal friction coefficient near the ice front of the Fleming Glacier (right column of Fig. 3.5 and left column of Fig. B6). We now consider causes for possible uncertainties in the force applied to the ice front, and whether high basal friction near the ice front is likely to be a feature of the real system or emerges from the inversion process as a compensating response to incorrect representation of these boundary conditions. These possible causes include uncertainty in local bedrock elevation (or equivalently ice thickness), uncertainty in the geoid-ellipsoid height conversion, uncertainty in observed sea level, uncertainty in exact ice front position and grounding line position, uncertainty in surface velocity, and uncertainty in potential backstress due to ice mélange and/or grounded icebergs in contact with the ice front. The sensitivity to various bedrock datasets has been discussed in Sec. 3.5.3. By assuming the ice front position to coincide with the 1996 grounding line, uncertainty about the bedrock depth at the ice front feeds into significant uncertainty in the total restraining force from ocean pressure. Regarding velocities, Friedl et al. (2018) presented evidence that an acceleration phase occurred on the Fleming Glacier between Jan-Apr 2008, but the surface velocity data used in the current study was extracted from measurements in Fall 2007 and 2008 (Rignot et al. 2011b). This means the surface velocity data, which provide the target to be matched by the inversion, might not be consistent with the DEM data used here (acquired in Jan 2008). To explore the influence of these different sources of uncertainty, we adopt different ice front positions and effective sea level heights as described in Sec. 3.4.6 (IFBC1-3 and IFP1-2, Table 3.2).

Experiments with different ice front positions (IFP1-2 in Table 3.2) directly affect the ice thickness and bed elevation at the ice front, which affects the ice front pressure condition. The simulated basal friction coefficients (left column in Fig. 3.7) show that the high sticky spots near the ice front migrate with the ice front position but with different patterns. The experiment IFP1 with a seaward shifted ice front position shows a decrease in magnitude of the high friction spots (Fig. 3.7b) and a better match with the observed velocity (Fig. 3.7e), while the IFP2 with a retreated ice front shows an increased C (Fig. 3.7c) and worse surface velocity match (Fig. 3.7f) compared with CTRL experiment (Figs. 3.7a, 3.7d). In experiment IFP1, thinner ice at the ice front leads to a relatively smaller ice velocity compared with CTRL, so the model does not need to increase C to match the observed surface velocity. This does not mean that ice front position in IFP1 is more accurate than CTRL, since the time inconsistency of surface DEM data, ice front and grounding line position, and surface velocity data is the obstacle to obtaining a reliable basal friction pattern. Therefore, we speculate that some of the high basal friction spots near the ice front are artefacts. However, we do not exclude the possibility of high basal friction spots caused by the pinning points located at the 1996 grounding line, which is also proposed by Friedl et al. (2018). An accurate location of the ice front and grounding line is clearly important for inverse modelling of fast-flowing glaciers like the Fleming Glacier.

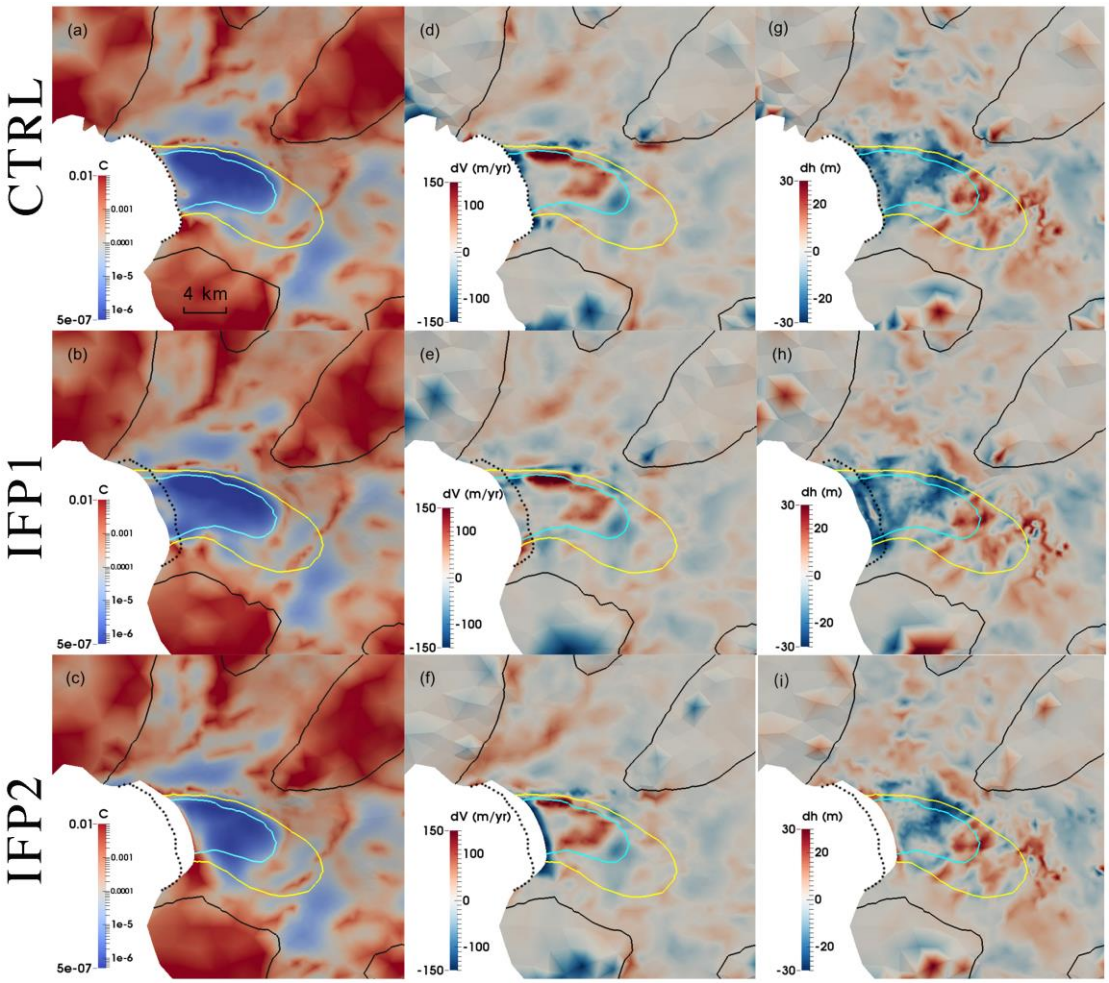

Figure 3.7. Distribution of basal friction coefficient C (MPa m^{-1} yr) (left column), the mismatch between the observed and modeled surface velocity (observed minus simulated; middle column), and the difference between the observed initial surface and relaxed surface elevation (observed minus relaxed; right column) from experiments: (a, d, g) CTRL (first row), (b, e, h) IFP1 (second row), and (c, f, i) IFP2 (third row). The black, yellow, and cyan solid lines represent surface speed contours of 100 m yr^{-1}, 1000 m yr^{-1}, and 1500 m yr^{-1}, respectively. Black dotted line is the 1996 grounding line position (Rignot et al. 2011a).

A higher sea level in the ice front boundary condition imposes a higher pressure at the ice front for the grounded ice, i.e. a higher total retarding force, and we impose these different boundary conditions as a proxy for the sources of uncertainty discussed above. Basal friction coefficients *C* simulated from the IFBC1-2 and CTRL experiments (Figs. 3.8a-c) present similar patterns but differ systematically around the ice front regions (within ~1 km of the grounding line). Experiments with higher sea levels display smaller *C* there (Fig. 3.8, left column) and provide a better match between modeled and simulated surface velocities (Fig. 3.8, middle column), which is consistent with the computed RMSD of the surface velocity mismatch (Table B5). If the applied ice front boundary condition underestimates the real world forcing, the inversion process will compensate by increasing the basal friction in this region.

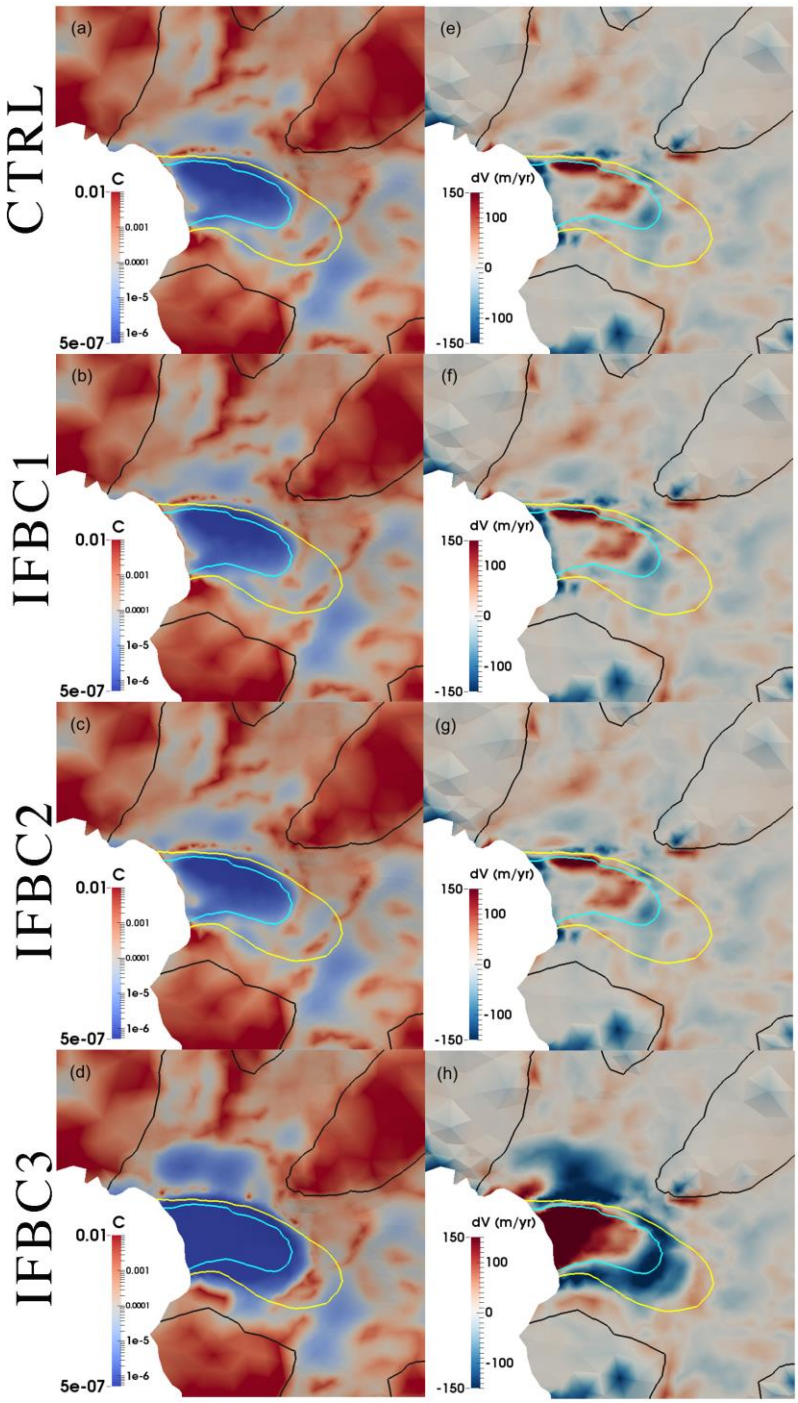

Figure 3.8. Distribution of basal friction coefficient C (MPa m^{-1} yr) (left column), and the mismatch between the observed and modeled surface velocity (observed minus simulated; right column) from experiments: (a, e) CTRL (first row), (b, f) IFBC1 (second row), (c, g) IFBC2 (third row), and (d, h) IFBC3 (fourth row). The black, yellow, and cyan solid lines represent surface speed contours of 100 m yr^{-1}, 1000 m yr^{-1}, and 1500 m yr^{-1}, respectively.

Experiment IFBC3, with an extreme assumption of applying ice pressure corresponding to a neighboring column of ice matching the ice front, shows very small basal friction for the downstream basin (Fig. 3.8d). However, IFBC3 introduces a much greater mismatch to the observed surface velocities (Fig. 3.8h), with

underestimated velocities over a substantial region extending upstream from the ice front and greater overestimate of velocities further upstream. This is only a sensitivity test but implies a potentially suitable ice front pressure may lie between IFBC2 and IFBC3. This set of experiments also suggests that moderate changes influence only a limited area. It is hard to decide the best ice front boundary condition here owing to the lack of precise bedrock data (as seen above) and difficulty of estimating the additional pressure from the partly detaching icebergs and ice mélange. As an indicator, the simulated ice mélange depth-integrated back stress (~1.1×10^{7} N m^{-1}) required to prevent the iceberg rotation at a calving front (Krug et al. 2015) would be comparable to an additional ~2.3 m in sea level in terms of ice front boundary condition for the Fleming Glacier. The thickness and density of mélange may affect this estimation. But it is certainly clear that the ice front boundary conditions can have a significant effect on the inversion results near the grounding line.

The different ice front boundary conditions also lead to minor differences in the surface relaxation at the ice front, with lower sea levels (and hence smaller back pressure at the ice front) leading to slightly greater lowering and corresponding steepening of the surface adjacent to the ice front (right column in Fig. 3.8; e.g. ~8 m lowering from IFBC2 to CTRL and from CTRL to IFBC1 at the ice front). The differences in surface elevation are localized to the ice front zone, with the relaxation over the rest of the domain essentially unaffected, except for the most extreme forcing. The lowered surface at the ice front in experiments IFBC1 and CTRL is apparently the consequence of rapid deformation due to its own weight (longitudinal extension with locally high vertical shear) of an ice cliff, which is over 100 m higher than the control sea level. However, the sticky spot located ~1 km upstream the ice front is a persistent feature except for the experiment IFBC3. This implies that the high friction near the ice front is sensitive to the boundary condition at the ice front.

Based on the experiments IFP 1-2 and IFBC1-3, we suspect the high friction near the ice front is likely an artefact due to errors in the ice front boundary condition but we cannot rule out the possibility that this may be a real feature. However, the impact diminishes rapidly with distance inland for moderate sea level shifts, which do not affect the general pattern of basal friction coefficients or the quality of the velocity matching more than ~2 km upstream of the grounding line.

3.6 Conclusion

We have obtained a basal friction coefficient distribution for the Wordie Ice Shelf-Fleming Glacier system in 2008, using an iterative spin-up scheme of simulations, observed surface velocities and a detailed surface DEM. We explored the sensitivity of the inversion for basal friction to four inputs to the modelling process. Within the approximation of using simulated steady-state ice temperatures, we showed that multiple temperature-inversion cycles are necessary to remove the influence of initial englacial temperature assumptions, at least for plausible initial temperature assumptions, and that a poor initial assumption will lead to a requirement for a greater

number of cycles. This conclusion is expected to also apply to other fast-flowing glacier systems that feature high rates of internal deformation.

Our inversion of the Wordie Ice Shelf-Fleming Glacier system is highly sensitive to the choice of ice flow enhancement factors and basal elevation datasets. The “bed_zc” bed topography, which used ice thickness determined using the mass conservation method for the fast-flowing regions, using contemporary velocities and ice thinning rates, and applied to the then current DEM, is suggested as the best current bed topography for further simulations in this region.

For the Wordie Ice Shelf-Fleming Glacier system, which we treated as grounded adjacent to the ice front, the inferred basal friction coefficient near that ice front is sensitive to the ice front position and ocean pressure boundary condition, emphasizing the importance of the normal force on the ice front and the accuracy of ice front positions. These factors have a very low impact on basal friction coefficients more than a few kilometres upstream of the grounding line, but may still be important when using inversion to initialize transient simulations, due to the high sensitivity of transient ice dynamic behavior to grounding line dynamics.

Chapter 4

Basal friction of Fleming Glacier, Antarctica, Part 2 - evolution from 2008 to 2015

Chapter 4 infers the basal shear stress distribution of the Fleming system in 2008 and 2015, and explores the mechanisms behind the rapid acceleration and greater thinning rates after 2008. The content of this chapter is published as Zhao et al. (2018) in The Cryosphere and is re-formatted for this thesis but otherwise presented as published in:

Zhao, C., R. M. Gladstone, R. C. Warner, M. A. King, T. Zwinger and M. Morlighem (2018). "Basal friction of Fleming Glacier, Antarctica - Part 2: Evolution from 2008 to 2015." The Cryosphere **12**(8): 2653-2666.

4.1 Abstract

The Wordie Ice Shelf-Fleming Glacier system in the southern Antarctic Peninsula has experienced a long-term retreat and disintegration of its ice shelf in the past 50 years. Increases in the glacier velocity and dynamic thinning have been observed over the past two decades, especially after 2008 when only a small ice shelf remained at the Fleming Glacier front. It is important to know whether the substantial further speed up and greater surface draw-down of the glacier since 2008 is a direct response to ocean forcing, or driven by feedbacks within the grounded marine-based glacier system, or both. Recent observational studies have suggested the 2008-2015 velocity change was due to the ungrounding of the Fleming Glacier front. To explore the mechanisms underlying the recent changes, we use a Stokes ice sheet model to infer the basal shear stress distribution of the Fleming system in 2008 and 2015. This study is part of the first high resolution modelling campaign of this system. Comparison of inversions for basal shear stresses for 2008 and 2015 suggests the migration of the grounding line ~9 km upstream by 2015 from the 2008 ice front/grounding line positions, which virtually coincided with the 1996 grounding line position. This migration is consistent with the change in floating area deduced from the calculated height above buoyancy in 2015. The retrograde submarine bed underneath the lowest part of the Fleming Glacier may have promoted retreat of the grounding line. Grounding line retreat may also be enhanced by a feedback mechanism upstream of the grounding line by which increased basal lubrication due to increasing frictional heating enhances sliding and thinning. Improved knowledge of bed topography near the grounding line and further transient simulations with oceanic forcing are required to accurately predict the future movement of the Fleming Glacier system grounding line and better understand its ice dynamics and future contribution to sea level.

4.2 Introduction

In the past few decades, glaciers in West Antarctica and the Antarctic Peninsula (AP) have experienced rapid regional atmospheric and oceanic warming, leading to significant retreat and disintegration of ice shelves and rapid acceleration of mass discharge and dynamic thinning of their feeding glaciers (Wouters et al. 2015, Cook et al. 2016, Gardner et al. 2018). Most of the West Antarctic Ice Sheet and the glaciated margins of the AP (Fig. 4.1a) rest on a bed below sea level sloping down towards the ice sheet interior, and the grounding lines of outlet glaciers located on such reverse bed slopes may be vulnerable to rapid retreat depending on the bedrock and ice shelf geometry (e.g., Schoof (2007), Gudmundsson et al. (2012), Gudmundsson (2013)). Once perturbed past a critical threshold, such as grounding line retreat over a bedrock hump into a region of retrograde slope, the grounding line may continue to retreat inward until the next stable state without any additional external forcing (e.g., Weertman (1974), Mercer (1978), Thomas and Bentley (1978)). This marine ice sheet instability has been invoked to explain the recent widespread and rapid grounding line retreat of glaciers in the Amundsen Sea sector, likely triggered by increased basal melting, reducing the buttressing influence of ice shelves (Rignot et al. 2014). Rapid grounding line retreat and accelerated flow in these unstable systems may lead to significant increases in ice discharge and increased contribution from these marine ice sheets to sea-level rise.

The former Wordie Ice Shelf (WIS; Fig. 4.1b) in the western coast of AP started its initial recession in the 1960s with a substantial break-up occurring around 1989, followed by continuous steady retreat (Vaughan and Doake 1996, Cook and Vaughan 2010, Wendt et al. 2010, Zhao et al. 2017). The former ice shelf is fed by three tributaries as shown in Fig. 4.1b. The Fleming Glacier (FG; Fig. 4.1b), as the main tributary glacier, splits into two branches: the main branch to the north and the southern branch (hereafter "southern FG"). The floating part in front of the main FG disappeared almost entirely sometime between 1997 and 2000 (Fig. 4.1b), and the ice front position in Apr 2008 (dark blue line in Figs. 4.1b and 4.1c, Wendt et al. (2010)) almost coincides with the latest known grounding line position in 1996 (Rignot et al. 2011a). The main branch of the FG has thinned at a rate of -6.25 ± 0.20 m yr^{-1} near the front from 2008 to 2015, more than twice the thinning rate during 2002-2008 (-2.77 ± 0.89 m yr^{-1}) (Zhao et al. 2017). This is consistent with recent findings that the largest velocity changes across the whole Antarctic Ice Sheet over 2008-2015 occurred within the FG (500 m yr^{-1} increase close to the 1996 grounding line) (Walker and Gardner 2017). Time series of surface velocities along the centerline of the FG (extending ~16 km upstream from the 1996 grounding line) (Friedl et al. 2018) indicate that two rapid acceleration phases occurred: in Jan-Apr 2008 and from Mar 2010 to early 2011, followed by a relatively stable period from 2011 to 2016. During the first acceleration phase in Jan-Apr 2008, the front of the FG retreated behind the 1996 grounding line position for the first time (Friedl et al. 2018).

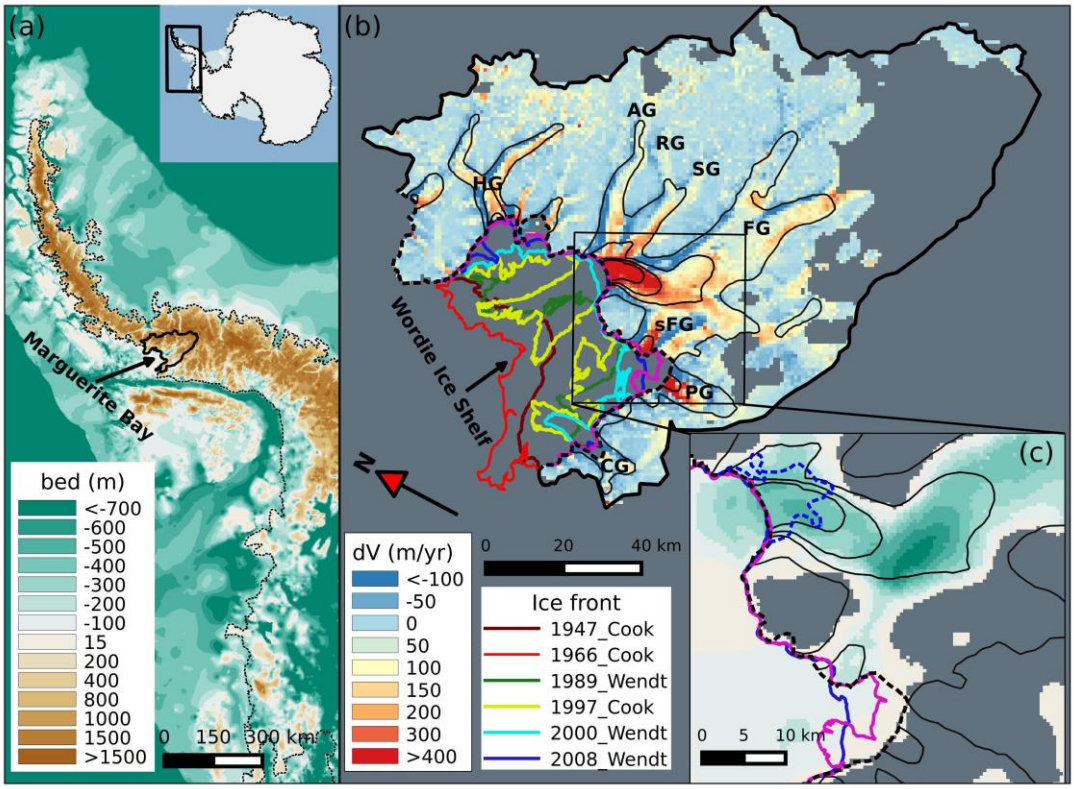

Figure 4.1. (a) The location of the study region in the Antarctica Peninsula (solid line polygon) with bedrock elevation data "bed_zc" ", based on Bedmap2 (Fretwell et al. 2013) but refined using a mass conservation method for the fast-flowing regions of the Fleming Glacier system (see Chapter 3). (b) Velocity changes of the Wordie Ice Shelf-Fleming Glacier system from 2008 (Rignot et al. 2011c) to 2015 (Gardner et al. 2018). Black contours representing the velocity in 2008 with a spacing of 500 m yr^{-1}. The colored lines represent the ice front positions in 1947, 1966, 1989, 1997, 2000, 2008, and 2016 obtained from Cook and Vaughan (2010), Wendt et al. (2010), and Zhao et al. (2017). The feeding glaciers for the Wordie Ice Shelf include three branches: Hariot Glacier (HG) in the north, Airy Glacier (AG), Rotz Glacier (RG), Seller Glacier (SG), Fleming Glacier (FG), southern branch of the FG (sFG) in the middle, and Prospect Glacier (PG), and Carlson Glacier (CG) in the south. The grey area inside the catchment shows the region without velocity data. (c) Inset map of the Fleming Glacier with ice front positions in 2008 and 2016, grounding line in 1996 (dashed black line) from Rignot et al. (2011a) and deduced grounding line in 2014 (dashed blue line) from Friedl et al. (2018). The background image is the bedrock from panel (a) and the black contours are the same ones as in panel (b).

As a marine-type glacier system residing on a retrograde bed with bedrock elevation as much as ~800 m below sea level (Fig. 4.1c), the Fleming system is potentially vulnerable to marine ice sheet instability (Weertman 1974, Mercer 1978, Thomas and Bentley 1978). The acceleration and greater dynamic thinning of the FG over 2008-2015 suggests the possible onset of unstable rapid grounding line retreat (Walker and Gardner 2017, Zhao et al. 2017), which has been confirmed by Friedl et al. (2018). The speedup of the FG before 2008 was originally assumed to be a continuing direct response to the collapse of the Wordie Ice Shelf (Rignot et al. 2005, Wendt et al.

2010). Recent studies have suggested that the recent further glacier speedup and grounding line retreat could be a direct response to oceanic forcing (Walker and Gardner 2017, Friedl et al. 2018). The recent acceleration could also be triggered by the continued dynamic thinning passing some threshold. An alternative hypothesis is that the recent changes are reinforced by feedbacks in the dynamics of the evolving glacier, possibly involving the subglacial hydrology. The examination of changes in basal shear stress distributions between 2008 and 2015 in this modelling study provides a first step in exploring some of these possible feedback hypotheses. We explore the potential for these hypotheses in Sec. 4.6.

By analyzing the detailed history of surface velocities, rates of elevation change, and ice front positions from 1994 to 2016, Friedl et al. (2018) suggested that the initial ungrounding of the FG from the 1996 grounding line position (Rignot et al. 2011a) occurred during the first acceleration phase, between Jan and Apr 2008, and expanded further upstream by ~6-9 km by 2014, explaining the speedup and thinning of the FG since 2008. They speculated this was mainly the result of unpinning caused by increased basal melting due to the greater upwelling of warm Circumpolar Deep Water (CDW) in 2008/2009 and 2010/2011 found by Walker and Gardner (2017). However, this study by Friedl et al. (2018) lacked direct measurements of basal melting and did not perform relevant numerical modelling of the evolution of a sub-ice ocean cavity or coupling to a cavity ocean circulation model, so it is still uncertain whether the enhanced basal melting driven by ocean warming is the only or best explanation for the recent changes in the FG. A positive feedback between basal sliding and basal water pressure (through friction heating) upstream of the grounding line could be another possible factor in the glacier acceleration and grounding line retreat (Iken and Bindschadler 1986, Bartholomaus et al. 2008, Schoof 2010). The possibility of such a feedback, is not ruled out by Friedl et al. (2018), and is discussed further in Sec. 4.5.2 and Sec. 4.6.

In this study, we employ the Elmer/Ice code (Gagliardini et al. 2013), a three-dimensional (3D) Stokes ice sheet model, to solve the Stokes equations over the whole WIS-FG catchment. Our implementation of the model solves the ice flow equations and the steady-state heat equation (Gagliardini et al. 2013, Gladstone et al. 2014). We also infer the basal shear stress using an inverse method (e.g., Gillet-Chaulet et al. (2016), Gong et al. (2017)).

In Chapter 3, we explored the sensitivity of the inversion for basal shear stress to: enhancement of ice deformation rates, bedrock elevation data, the ice front boundary condition, and initial model assumptions about englacial temperatures. In the current paper, we adopt the three-cycle spin-up scheme of Chapter 3 to derive the distributions of basal shear stress in 2008 and 2015. We present the observational data in Sec. 4.3 and our methods in Sec. 4.4. We compare the resulting basal shear distributions for 2008 and 2015 and their connections with driving stress and basal friction heating in Sec. 4.5.1 and Sec. 4.5.2. The height above buoyancy for the two epochs is computed in Sec. 4.5.3 as an independent indication of grounding line

changes. Through comparison of basal shear stress and height above buoyancy estimates from 2008 and 2015, we analyze the stability of the grounding line in this period and discuss the potential for ongoing marine ice sheet instability and direct oceanic forcing as possible reasons for the speed-up of the FG in Sec. 4.6.

4.3 Observational Data

4.3.1 Surface elevation data in 2008 and 2015

The surface elevation dataset for 2008 (DEM2008; Fig. 4.2a) from Chapter 3 plays a central role here. To estimate the surface topography in 2015 (DEM2015; Fig. 4.2a), we calculated the average surface-lowering rate during 2008-2015 for the fast flow regions (surface velocity in 2008 $\geq$ 20 m yr^{-1}) using the hypsometric model for elevation change described in Zhao et al. (2017) for the same period. The DEM2015 was then generated from DEM2008 by applying these ice thinning rates from 2008 to 2015. For the area with velocities < 20 m yr^{-1}, we assume the DEM in 2015 remains the same as that in 2008.

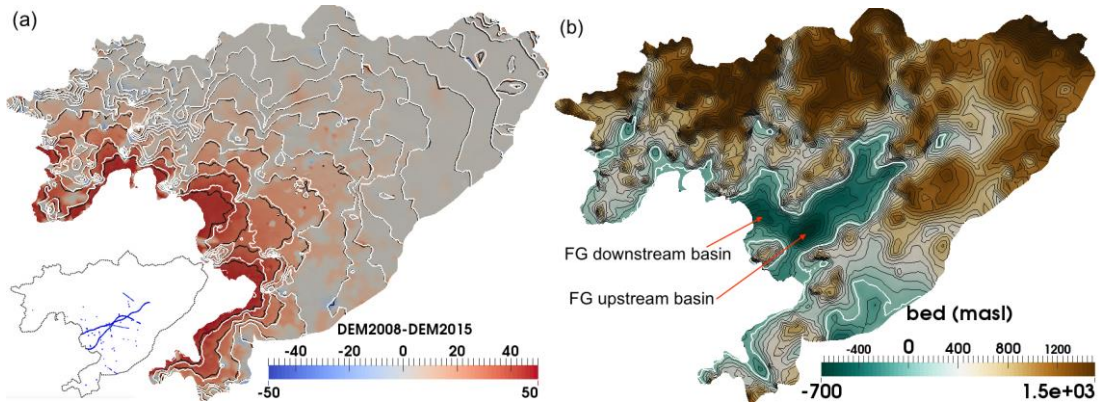

Figure 4.2. (a) Surface elevation difference between 2008 and 2015 (2008 minus 2015) with black and white contours (interval: 200 m) representing the surface elevation in 2008 and 2015, respectively. Inset map shows the location in the research domain with blue points showing the available elevation data points used to extract the hypsometric model of elevation change from 2008 to 2015 (Zhao et al. 2017). (b) Bed elevation data "bed_zc" (metres above sea level, masl) with two basins "FG downstream basin" and "FG upstream basin" from Chapter 3. The black contours show the bed elevation with an interval of 100 m. The white contour represents the sea level used in this study.

4.3.2 Bed elevation data

The bed topography plays a significant role in simulation of basal sliding and ice flow distribution for fast-flowing glaciers (see Chapter 3), and also in interpreting the grounding line movement precisely (Durand et al. 2011, De Rydt et al. 2013, Rignot et al. 2014). Chapter 3 investigated the sensitivity of the basal shear stress distribution to three bedrock topography datasets. The bedrock dataset, bed_zc (Fig. 4.2b), with higher accuracy and resolution, was suggested as the most suitable for modelling the WIS-FG system. Recall that bed_zc is computed by:

$$bed\_zc = S_{2008} - H_{mc} \quad (4.1)$$

where S_{2008} is the surface elevation in 2008 combined from two DEM products as discussed in Chapter 3, and H_{mc} is the ice thickness data with a resolution of 450 m combined from the ice thickness data computed using a mass conservation method for the regions of faster flow (Morlighem et al. 2011, Morlighem et al. 2013), and ice thickness from Bedmap2 for other regions (Fretwell et al. 2013). A complete description is given in Chapter 3.

4.3.3 Surface velocity data in 2008 and 2015

We use the same velocity data for 2008 as in Chapter 3, which is from the InSAR-based Antarctic ice velocity dataset MEaSUREs (version 1.0) produced by Rignot et al. (2011c) from fall 2007 and/or 2008 measurements over the study area. The 2008 velocity dataset has a resolution of 900 m and the uncertainties over the study region range from 4 m yr^{-1} to 8 m yr^{-1}. For 2015, we adopt the velocity data extracted from Landsat 8 imagery with a resolution of 240 m and errors ranging from 5 m yr^{-1} to 20 m yr^{-1} (Gardner et al. 2018). The velocity dataset for 2015 has a full coverage over the WIS-FG domain, while the velocity in 2008 has no data in the gray area in Fig. 4.1b. Comparison between the velocity dataset in 2008 and 2015 shows some slowing down margins along the 100 m yr^{-1} contour in Fig. 4.1b. It may be caused by some geocoding issues between the SAR velocity in 2008 (Rignot et al. 2011c) and Landsat velocity in 2015 (Gardner et al. 2018), which are most likely due to errors in the elevation model used to convert from radar slant range coordinates to a location on the Earth surface (Gardner et al. 2018).

4.3.4 Other datasets

The steady state temperature field is simulated from an initial temperature field, linearly interpolated between upper and lower ice surfaces, which leads to robust inversion results as demonstrated in Chapter 3. The surface temperature is constrained throughout the simulations by yearly averaged surface temperature over 1979-2014 computed from RACMO2.3/ANT27 (van Wessem et al., 2014) while the basal temperature is initialized to pressure melting temperature. The temperature simulations use the spatial distribution of geothermal heat flux estimated by Fox Maule et al. (2005) and the simulated basal frictional heating.

Our DEM is based on ellipsoidal WGS84 system and hence a height of 0 m does not refer to sea level. An observed sea level height of 15 m (WGS84 ellipsoidal height) in Marguerite Bay (see Chapter 3) was taken to compute the sea pressure on the ice front.

4.4 Methods

The modelling methods using Elmer/Ice presented in Chapter 3 are adopted here, including the mesh generation, mesh refinement, model parameter choices and boundary conditions. The simulations for both 2008 and 2015 retain the same assumptions about the ice-covered domain, namely a common spatial extent with

fixed ice front location, and the assumption that all the ice is grounded. The ice front position is assumed to coincide with the 1996 grounding line position (Rignot et al. 2011a). This assumption might be incorrect for the main branch of the FG, and we evaluate it based on the deduced floating area where the inferred basal shear stress is lower than a threshold, which is discussed in Sec. 4.5.1. It is very clear from satellite imagery that in 2008 a small ice shelf is still present in front of the southern FG and the Prospect Glacier (hereafter PG) (Fig. 4.1c). In 2015 the ice shelf in front of the southern FG has disappeared, while the floating part of the PG has retreated in the east and re-advanced in the west (Fig. 4.1c). However, we don't include the floating parts of the southern FG and PG in either epoch in this study, owing to the lack of ice shelf thickness data.

We follow the three-cycle spin-up scheme (see Chapter 3) and simulate the basal shear stress $\boldsymbol{\tau_b}$ in 2008 and 2015 with the linear sliding law:

$$\boldsymbol{\tau_b} = -C\boldsymbol{u_b} \tag{4.2}$$

Here C is the basal friction coefficient, a variational parameter in the inversion procedure, and $\boldsymbol{u_b}$ is the modelled basal sliding velocity.

There are two key differences between the data used for the 2008 and 2015 inversions: increased surface velocity and changed ice geometry, namely a thinner glacier in 2015 compared to 2008 due to dynamic thinning. To explore their relative impacts, we carry out an additional inversion with the geometry from 2008 but the surface velocity from 2015 (see Sec. C1 in Appendix C). We find that both geometry variations and velocity changes are important to the inverted basal stress condition.

To explore the relationship between the basal shear stress and local gravitational driving stress τ_d, the magnitude of the gravitational driving stress is also computed for both epochs:

$$\tau_d = \rho_i g H \left|\vec{\nabla} z_s\right| \tag{4.3}$$

where ρ_i is the ice density, g is the gravitational constant, H is the ice thickness, and $\left|\vec{\nabla} z_s\right|$ is the magnitude of the gradient of the ice surface elevation. Considering the snow and firn on the ice surface, we apply a relatively low ice density of 900 kg m^{-3} following Berthier et al. (2012).

Hoffman and Price (2014) found a positive feedback between the basal melt and basal sliding through the frictional heating for an idealized mountain glacier using coupled subglacial hydrology and ice dynamics models. To explore possible effects of changes of basal frictional heating between 2008 and 2015, we compute the friction heating (q_f) generated at the bed:

$$q_f = \tau_b u_b \tag{4.4}$$

To explore the possible flow path of subglacial water beneath the FG, we calculate hydraulic potential at the bed, since its negative gradient determines subglacial flow

direction. The hydraulic potential, Φ, expressed in equivalent metres of water, is given by:

$$\Phi = (z_s - z_b)\frac{\rho_i}{\rho_{fw}} + z_b \quad (4.5)$$

where ρ_{fw} is the fresh water density (1000 kg m^{-3}), and z_s and z_b are the surface and bed elevations, respectively. Here we assume that the water pressure in the subglacial hydrologic system is given by the ice overburden pressure, which is equivalent to assuming that the effective pressure at the bed, *N*, is zero (Shreve 1972).

Height above buoyancy (Z_*) is an indicator of how close to floatation a marine-based glacier is, which is relevant to the glacier's evolution and additionally helps identify likely floating regions. Here, we assume that Z_* is related to the effective pressure *N* at the bed by the relationship:

$$N = \rho_i g Z_* \quad (4.6)$$

In this study, we use a simpler hydrostatic balance based on sea level with the relationship:

$$Z_* = \begin{cases} H, & if\ z_b >= z_{sl} \\ H + (z_b - z_{sl})\frac{\rho_w}{\rho_i}, & if\ z_b < z_{sl} \end{cases} \quad (4.7)$$

where ρ_w is the density of ocean water and z_{sl} is the sea level. This expression for Z_* assumes a perfect connectivity of the basal hydrology system with the ocean. This is appropriate for the present study where we are exploring the degree of grounding of the fast-flowing regions of the FG over the downstream basin.

4.5 Results

4.5.1 Comparison of basal shear stress and driving stress in 2008 and 2015

We obtain the spatial distributions for basal shear stress, τ_b (Figs. 4.3a, 4.3b), and basal velocity of the WIS-FG system for 2008 and 2015 using an inverse method to determine the basal friction coefficient, *C*, with the geometry and velocity data described above. Although low-resolution estimation of basal shear stress has been carried out for the whole Antarctic Ice Sheet (Morlighem et al. 2013, Sergienko et al. 2014, Fürst et al. 2015), this is the first application of inverse methods to estimate the basal friction pattern of the Fleming system at a high resolution and use the Stokes equations.

In 2008 the main FG shows some sticky spots of high basal shear stress close to the ice front (Fig. 4.3a). The backstress exerted by these sticky spots with τ_b>0.01 MPa (shown in Fig. C3) is ~3.42×10^{11} N, while immediately upstream a region of low basal stress covers most of the downstream bedrock basin, returning to more typical values (~0.05-0.53 MPa) ~9 km from the ice front. In contrast, the basal friction at the front of the southern FG is low, with more typical values (~0.05-0.53 MPa) ~2 km upstream. By 2015, the high friction spots near the FG ice front have disappeared while in the downstream basin the region of low basal shear stress already seen in

2008 is more extensive and even lower in value (Fig. 4.3b). This is consistent with the observed speed-up from 2008 to 2015. Further upstream in this basin, and over the ridge between the downstream and upstream basins, the basal shear stress does not change much between the two epochs (Fig. 4.3c).

To explore the ice dynamics evolution from 2008 to 2015, we present the ratio of basal shear stress τ_b to driving stress τ_d (hereafter referred as "RBD") in Figs. 4.3d, 4.3e, which can provide insight into the dynamical regime (Morlighem et al. 2013, Sergienko et al. 2014). In particular, it provides an indication whether the driving stress is locally balanced by the basal shear or whether there is a significant role for membrane stresses and a non-local momentum balance. We designate the region with τ_b < 0.01 MPa or RBD < 0.1 as a "low friction" area, potentially indicative of flotation, i.e. ungrounded ice.

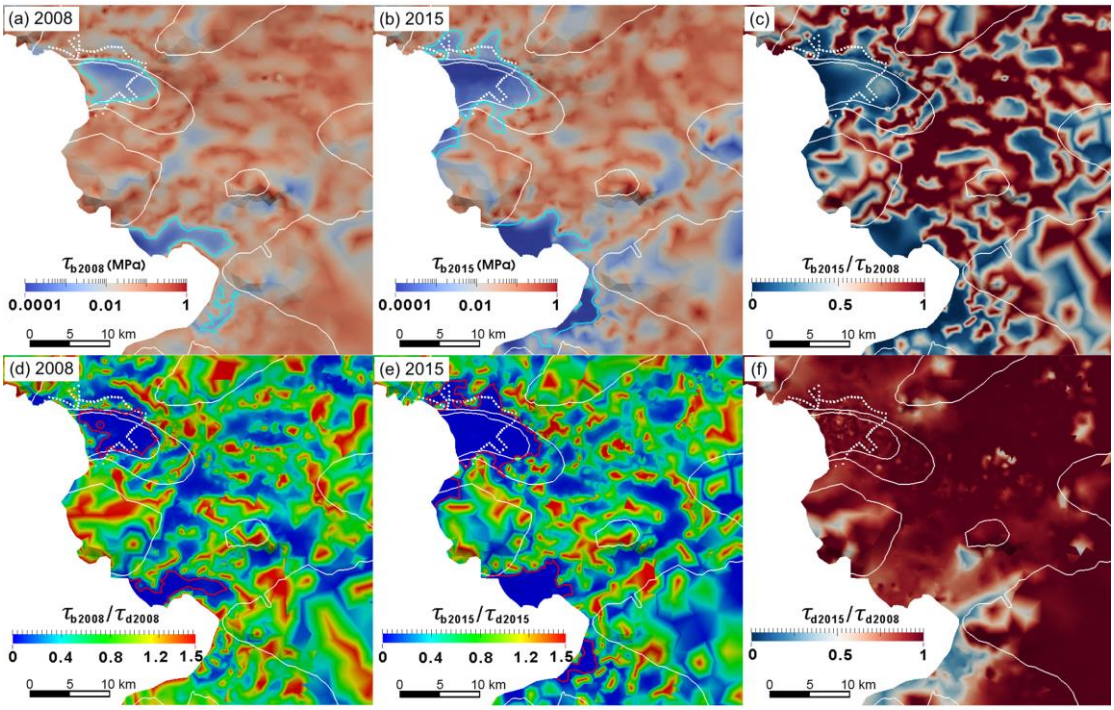

Figure 4.3. (a,b) Basal shear stress τ_b, (d, e) the ratio of τ_b to τ_d, of the Fleming Glacier and the Prospect Glacier in 2008 (left) and 2015 (middle). (c) the ratio of basal shear stress τ_{b2015} to τ_{b2008}, and (f) the ratio of driving stress τ_{d2015} to τ_{d2008}. The white dotted line represents the deduced grounding line in 2014 from Friedl et al. (2018). The cyan lines in (a) and (b) show the τ_b=0.01 MPa contour. The red lines in (d) and (e) show the RBD = 0.1 contour in the current study. The white solid lines represent the 2008 surface speed contours of 100 m yr^{-1}, 1000 m yr^{-1}, and 1500 m yr^{-1}, respectively, to aid visual comparison across subplots.

The high basal shear stress spots inferred by the inversion at the front of the main branch of the FG in 2008 (Fig. 4.3a) may be artefacts due to uncertainties from the ice thickness, local bed topography, local sea level, ice mélange backstress, and the ice front position (as discussed in Chapter 3). Sensitivity to such uncertainties was explored in Chapter 3, and the adjustments of ice front boundary condition with a higher sea level of 25 m or an advanced ice front position showed a decrease in the

basal friction coefficients near the ice front, but did not completely remove these high basal friction spots. This implies that the front of the FG in 2008 might still be partly grounded on the 1996 grounding line due to the presence of real pinning points.

As expected, the gravitational driving stress of this system shows no significant changes from 2008 to 2015, except for the front of PG (Fig. 4.3f). In 2015, the boundaries of the zone in the main FG with τ_{b2015} < 0.01 MPa (blue lines in Fig. 4.3b) or RBD_{2015} < 0.1 (red lines in Fig. 4.3e) have some similarity to the deduced grounding line position of the FG in 2014 from Friedl et al. (2018) (white dots in Figs. 4.3 and 4.4). The differences with that study are around the southern and eastern parts, but the blue and red boundaries fit the bedrock ridges in the present study (Figs. C2b), while the white points fit the corresponding bedrock topography data used by Friedl et al. (2018). This comparison confirms the significant role of bedrock topography in determining the grounding line position. Around the eastern part of the region, within which velocities > 1500 m yr^{-1} (Fig. 4.3b), the low basal friction area in this study extends ~1-3 km further upstream than the estimated grounding line in 2014 (Friedl et al. 2018).

Comparison of basal shear stress between 2008 and 2015 (Fig. 4.3c) shows a significant decrease from 2008 to 2015 in fast-flowing regions (velocity > 1500 m yr^{-1}) at the front of the FG. A similar pattern occurred at front of the PG and the southern FG. For the northern section of the southern FG, the grounding line has retreated by ~2 km in 2008 from the last known grounding line position in 1996 (Rignot et al. 2011a) (Fig. 4.3a), which is reasonable considering that the northern section of the ice front has retreated ~2 km behind the 1996 grounding line position (Fig. 4.1c). However, it is not clear whether the southern section of the southern FG has also retreated in 2008 as indicated in Fig. 4.3a, and whether the floating area has expanded ~3 km further inland in 2015 based on the decreased basal shear stress from 2008 (Fig. 4.3a) to 2015 (Fig. 4.3b). Similarly, it is also hard to estimate the possible grounding line positions of the PG based from the inferred basal shear stress in both epochs. That is because we did not account for the normal stress of the remnant small ice shelf at the front of the southern FG and the PG (Fig. 4.1c) in the inverse modelling. The surface lowering in DEM2015 for the PG could also be an artefact since no observations were available for the PG when building the hypsometric model that generates the DEM2015 (see inset map in Fig. 2a; Zhao et al. (2017)).

4.5.2 Basal melting and subglacial hydrology

Increases in subglacial water pressure could contribute to lower basal shear stress and higher basal sliding at the base of the FG, potentially through the positive hydrology feedback mentioned earlier. That feedback mechanism can be summarized simply: a general acceleration of glacier flow (for example due to a backstress reduction from ice shelf collapse or unpinning from a sticky spot) can lead to increased basal sliding in regions where the basal shear stress almost remains unchanged (for example in the FG trunk above the downstream basin (Figs. 4.3a-c). This increases friction heating and basal melt water generation, which - as suggested by Hoffman and Price (2014) -

may increase the effective basal water pressure downstream, thereby increasing sliding speeds (Gladstone et al. 2014, Hoffman and Price 2014). Since the reduction of effective pressure is the key process to enhance sliding, this positive feedback is dependent on a positive feedback of melt water generation to water pressure. This dependence can break down when there is sufficient basal water to generate efficient drainage channels (Schoof 2010). However, such efficient channelization in the subglacial hydrologic system is typically associated with seasonal surface meltwater pulses reaching the bed (Dunse et al. 2012), a process that is not expected to occur for Fleming Glacier (Rignot et al. 2005).

Basal melt water arises from two main sources in polar regions: either surface melt water draining into the subglacial hydrologic system via crevasses or moulins or in-situ melting at the bed (Hoffman and Price 2014, Dunse et al. 2015, Banwell et al. 2016). However, the amount of surface melt water in the WIS-FG region is not thought to be sufficient to percolate to the base (Rignot et al. 2005), so we take basal melting due to the friction heat and geothermal heat flux as the only source of subglacial water. The geothermal heat flux in the fast-flowing regions of our study area (Fox Maule et al. 2005) is two orders of magnitude smaller than the friction heating at the base, leaving friction heating as the dominant factor in generating basal melt water.

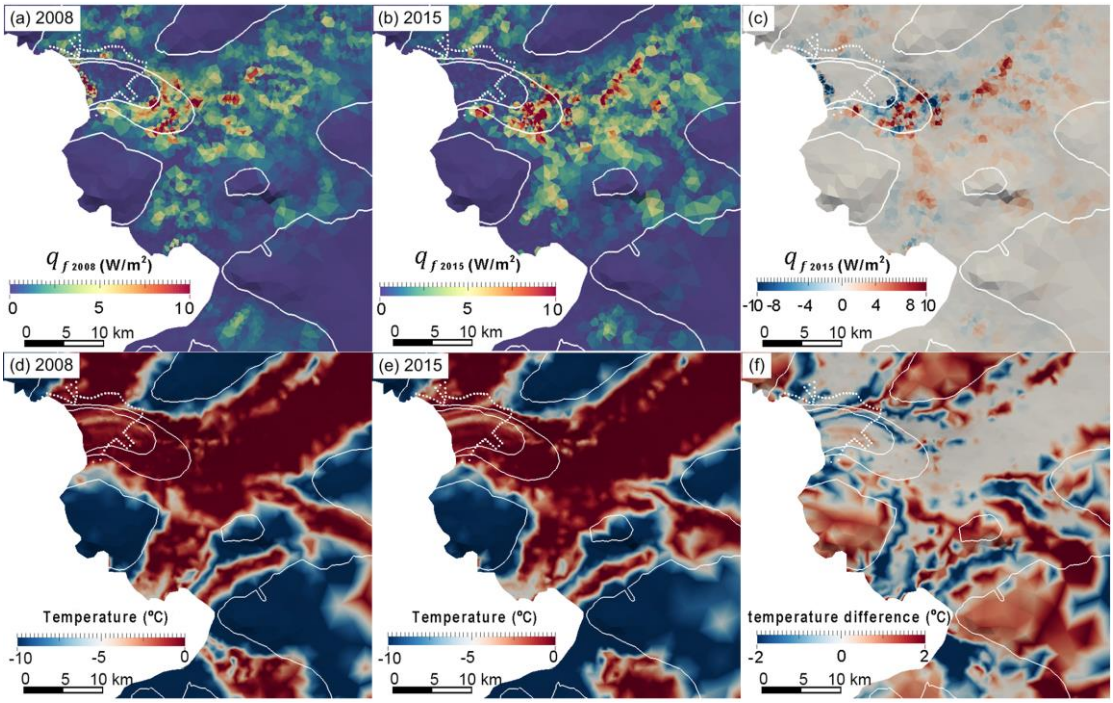

Figure 4.4. (a, b) The basal friction heating, and (d, e) the simulated temperature relative to the pressure melting point at the base of the Fleming Glacier and the Prospect Glacier in 2008 (a, d) and 2015 (b, e). The differences of (c) basal friction heating and (f) simulated basal temperature between 2008 and 2015 (2015 minus 2008). The white dotted line represents the deduced grounding line in 2014 from Friedl et al. (2018). The white solid lines represent the 2008 surface speed contours of 100 m yr^{-1}, 1000 m yr^{-1}, and 1500 m yr^{-1}.

To explore the potential subglacial water sources and the likely flow directions, we plot the frictional heating in both 2008 and 2015 (Figs. 4.4a, 4.4b), the basal temperature relative to the pressure melting point for both epochs (Figs. 4.4d, 4.4e), and the contours of hydraulic potential in 2008 (Φ; Fig. 4.5). Friction heating due to sliding at the bed (Figs. 4.4a, 4.4b) provides a basal melt water source where ice is at pressure melting point, which is the case for the fast flow regions of the FG (see the basal temperature relative to the pressure melting point in Figs. 4.4d, 4.4e), while the gradient of the hydraulic potential (Fig. 4.5) indicates likely water flow paths at the ice-bed interface. The hydraulic potential evolves between 2008 and 2015 due to the changes in surface elevation (Fig. 4.2a) in Eq. 4.5, but this does not appreciably change the pattern of subglacial water flow. The frictional heat generated at the base is high where both basal shear stress and basal sliding velocities are high. The modelled friction heating in both 2008 and 2015 (Figs. 4.4a, 4.4b) extends as far as the upstream basin under the FG, indicating high basal melt rates in this region (a heat flux of 1 W m^{-2} could melt ice at the rate of 0.1 m yr^{-1} in regions at the pressure melting temperature). The highest friction heating is generated over the bedrock rise between the FG upstream and downstream basins, where the most melt water will be produced, and this will be routed towards the downstream basin given the gradient of hydraulic potential in this region (Fig. 4.5). Hence it is a major source of basal water for the downstream basin. This could explain the low basal friction downstream, while the increase in heating between 2008 and 2015 (Fig. 4.4c) could further enhance the basal sliding in the fast-flowing regions, contributing to the observed accelerations. Both the hydraulic potential and frictional heating could help to understand the mechanism behind the rapid acceleration and surface draw-down of the FG, which is further discussed in Sec. 4.6.

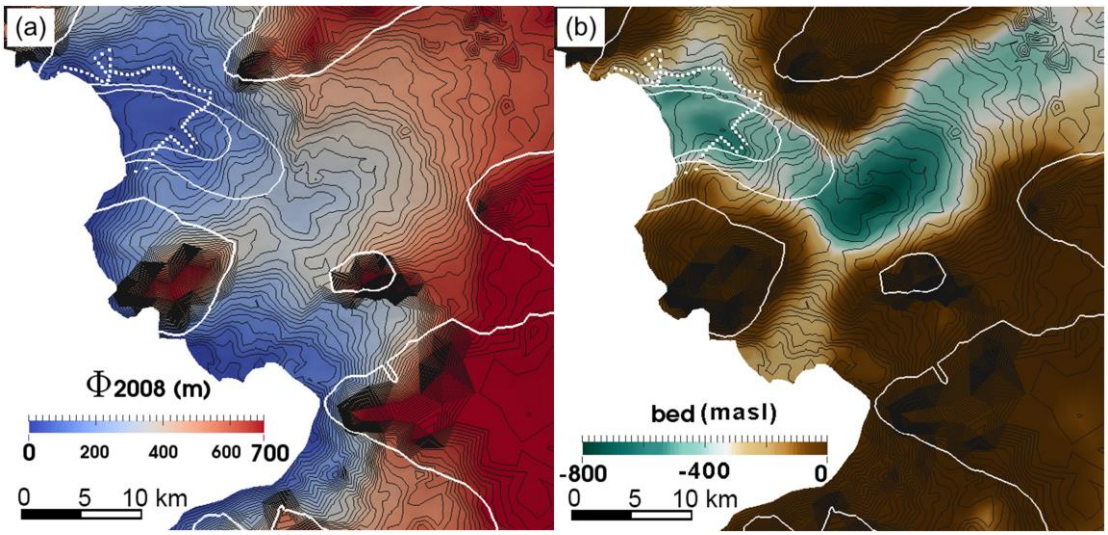

Figure 4.5. (a) The hydraulic potential in 2008 and (b) the submarine bedrock elevation (m a.s.l.). In both figures the dense contours represent the hydraulic potential with a spacing of 20m (black solid lines). The white dotted line represents the deduced grounding line in 2014 from Friedl et al. (2018). The white solid lines represent the 2008 surface speed contours of 100, 1000, and 1500m yr^{-1}.

4.5.3 Height above buoyancy

We compute the height above buoyancy, Z_*, for 2008 and 2015 for the FG based on Eq. (4.7) with a sea level of 15 m (Figs. 4.6a, 4.6b). To allow for the over- or under-estimation of Z_* owing to uncertainties from the topography data, ice thickness, ice density and the sea level applied above, we suggest that the areas where $Z_* < 20$ m might be floating, while including areas where $Z_* > -20$ m in Fig. 4.6.

In 2008 a low height above buoyancy (Fig. 4.6a) is only found near the 1996 grounding line position in the downstream basin, which indicates that ungrounding of the main FG may not have started or only just commenced in 2008. In 2015, the area close to flotation with $Z_* < 20$ m (taken as an upper limit) has expanded, reaching about 9 km upstream (magenta lines in Fig. 4.6b), which broadly coincides with the estimated grounding line in 2014 (Friedl et al. 2018) except for an almost encircled patch with slightly higher Z_* (20-30 m). The implications of the different Z_* from 2008 and 2015 are a small FG grounding line retreat from 1996 to 2008 but significant retreat from 2008 to 2015. Uncertainty in the predicted grounding line in 2015 is significant, but a new position ~9 km upstream is likely.

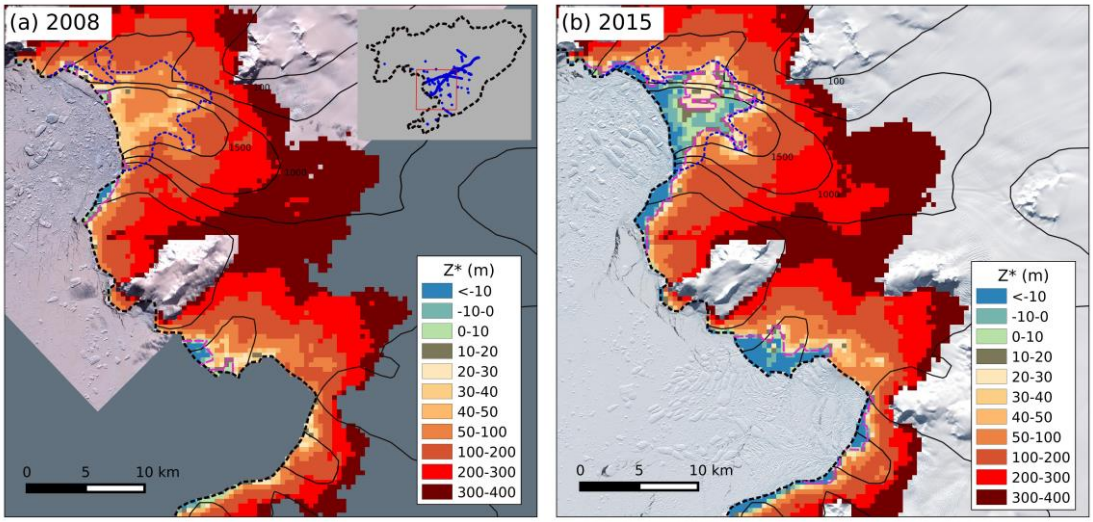

Figure 4.6. The height above buoyancy Z_* in (a) 2008 and (b) 2015 of the Fleming Glacier and Prospect Glacier. The background images are from (a) ASTER L1T data in Feb 2nd, 2009, and (b) Landsat-8 in Jan 13th 2016, respectively. The black lines represent velocity contours in 2008 (Rignot et al. 2011c). The dashed black and blue lines show the grounding line in 1996 (Rignot et al. 2011a) and 2014 (Friedl et al. 2018), respectively. The dashed magenta line shows the possible grounding line with $Z_* < 20$ m. Inset map shows the location in the research domain with blue points showing the available elevation data points used to extract the hypsometric model of elevation change from 2008 to 2015 (Zhao et al. 2017).

In addition to the main branch of the FG, its southern branch and the PG also show an expansion of the region in which Z_* is close to zero, which indicates possible grounding line retreat. However, the DEM2015 used to compute Z_* has large uncertainties in the southern branch of FG and PG, since the surface lowering in DEM2015 for those regions could be artefacts due to the lack of observations as

mentioned above (see inset map in Fig. 4.2a; Zhao et al. (2017)). Therefore, it is hard to determine the current grounding line locations for those two glaciers.

Changes in Z_* from 2008 to 2015 suggest the creation of an ungrounded area consistent with the area of very low modelled basal shear stress shown in Figs. 4.3a and 4.3b. This change in area close to floating, defined by $Z_* < 20$ m, constitutes additional evidence supporting the hypothesis of rapid grounding line retreat over 2008 to 2015 and the likely grounding line positions of the FG in both epochs.

4.6 Discussion

The sticky spots of high basal shear stress near the terminus of the FG in 2008 might be artefacts, but the possibility that this high friction area is a real feature due to some pinning points is not excluded. If the high basal resistance spots are artefacts, ungrounding of this region in early 2008 would not have caused a significant reduction in backstress, and would be less viable as an explanation for an abrupt increase in ice flow speed. In this case, positive feedbacks, such as the marine ice sheet instability or the basal melt feedback, are even more likely to explain the FG's recent behavior. If the sticky spots are real features, the implication is that the ice front was at least partly grounded in early 2008. This interpretation is consistent with the relatively high bedrock topography near the ice front compared to upstream (Fig. 4.1c). Friedl et al. (2018) proposed that the grounding line of the FG after Jan-Apr 2008 must have been located upstream of the 1996 grounding line from their interpretation of abrupt surface acceleration detected around the same period. This is also confirmed by the fact that the glacier front had retreated behind the 1996 grounding line during the acceleration phase (Friedl et al. 2018). However, it is possible that this grounding line retreat occurred after Jan 2008, when our DEM2008 was acquired. The analysis of height above buoyancy for DEM2008 and inferred basal shear stress in 2008 support the main FG being grounded close to the ice front and hence near the 1996 grounding line location. Given the uncertainties of grounding line position in 1996 (several kilometres) (Rignot et al. 2011a) and uncertainty about interpreting the frontal high basal friction area in this study, the exact grounding line position in January 2008 is somewhat uncertain. Improved bed topography/ice thickness data and accurate historic ice front position are necessary to interpret the precise grounding line position in 2008. Detailed bathymetry of the relevant location might become available if the ice front of the FG retreats in future.

The disappearance of the inferred high basal shear region (possible physical pinning points) near the FG front between 2008 and 2015 is a possible trigger for the sudden acceleration and increased surface lowering of the FG during this period. The increased flux of ice, combined with the changed glacier geometry, suggests the substantial grounding line retreat, which agrees with two recent studies (Walker and Gardner 2017, Friedl et al. 2018). The timing of the acceleration, which occurred in Jan-Apr 2008 (Friedl et al. 2018), suggests that the loss of this basal resistance occurred shortly after the first epoch we analyzed (Jan 2008). Given the low basal friction already present over most of the downstream basin (a possible cavity

proposed by Friedl et al. (2018)), one would expect the loss of the localized friction near the ice front to promptly result in an increase in velocity over the entire low-friction region. This is consistent with the near uniform increase in velocity in Apr 2008 for a region 4-10 km upstream of the 1996 grounding line reported by Friedl et al. (2018).

For a glacier lying on a retrograde slope in a deep trough, the grounding line may be vulnerable to rapid retreat without any further change in external forcing, once its geometry crosses a critical threshold, which is the marine ice sheet instability hypothesis (e.g., Weertman (1974), Mercer (1978), Thomas and Bentley (1978)). A similar theory has been proposed for the expected rapid retreat of Jakobshavn Isbræ in West Greenland without any external climate forcing) after detaching from a pinning point (Steiger et al. 2017). The FG grounding line in early 2008 may have experienced a retreat after moving across the geometric pinning points near the front, and then retreated further to the position about 9 km upstream in the FG downstream basin by 2015. This has been proven by Friedl et al. (2018), and they also suggested that a further stage of grounding line retreat of the FG may have happened between Mar 2010 and early 2011. A similar ungrounding process has been detected in the Thwaites, Smith and Pine Island Glaciers from 1996 to 2011 (Rignot et al. 2014).

The current grounding line of the FG (Friedl et al. 2018) appears to be on the prograde slope of the bedrock high between the FG downstream and upstream basins. With the establishment of an ocean cavity under the new ice shelf we can expect that ocean-warming driven basal melting will further modify the thickness of the recently ungrounded ice. If the system remains out of balance and continues to thin, the grounding line could eventually move beyond this bed obstacle. If this occurs, the grounding line is then likely to retreat rapidly down the retrograde face of the FG upstream basin, to be accompanied by further glacier speed up and dynamic thinning.

Walker and Gardner (2017) attribute the significant increase in observed ice velocity and drop in surface elevation from 2008 to 2015 to increased calving front melting caused by incursion of relatively warm Circumpolar Deep Water (CDW). The CDW flows onto the continental shelf within the Bellingshausen Sea, penetrating into Marguerite Bay, driven by changes in regional wind patterns resulting from global atmospheric circulation changes (Walker and Gardner 2017). Friedl et al. (2018) also explain both the unpinning from the 1996 grounding line position in 2008 and further landward migration of the grounding line in 2010-2011 with the same mechanism, namely the increased basal melting due to ocean warming. This explanation appears consistent with the finding that the acceleration, retreat, and thinning of outlet glaciers in the Amundsen Sea Embayment (ASE) are triggered by the inflow of warm CDW onto its continental shelf and into sub-ice-shelf cavities (Turner et al. 2017). However, the floating parts of the FG remained negligible in 2008 as indicated in Sec. 4.5.3 (Fig. 4.6a). The speedup and ungrounding occurring in the ASE glaciers was a direct response to significant loss of buttressing caused by ice shelf thinning and grounding-line retreat (Turner et al. 2017). When the CDW incursions started in the ASE, the

floating parts of ASE glacier systems were much larger than the residual ice shelf of the Fleming system in 2008. After the recent changes the newly floating region of the FG has an area of ~60 km^2, based on the estimated 2014 grounding line from Friedl et al. (2018) and the 2016 ice front position in this study, which is consistent with our height above buoyancy analysis for 2015 (Fig. 4.6b). So, significant buttressing reduction is not likely to have occurred on the FG during the rapid acceleration of 2008, but further changes to the FG after 2015 may more closely resemble ASE glacier and ice shelf systems. No direct measurements are available to confirm the direct effect of the frontal or basal melting on the FG grounding zone over this period, nor have previous studies attempted to quantify the amount of melting required to drive significant FG grounding line retreat. The ocean-driven basal melting at the ice shelf front or base may have contributed to grounding line retreat, or the reduction of the frontal high basal shear zone but establishing this as the main cause would require further quantification of the cause-effect link.

Ongoing thinning as a result of backstress reduction following the collapse of the WIS is another possible cause for the recent ungrounding. The WIS evolved from an embayment-wide ice shelf in 1966 to smaller individual remnant ice shelves in 1997 (Fig. 4.1b) (Cook and Vaughan 2010, Wendt et al. 2010). The floating part of the FG in particular was in the form of an ice tongue in 1997 (Cook and Vaughan 2010), and as such would likely have imposed much lower backstress on the grounded part. Point measurements indicate that the FG accelerated by 40-50% between 1974 and 1996 (Doake 1975, Rignot et al. 2005). If this acceleration was a response to loss of buttressing, the FG system may have been out of equilibrium, and losing mass, since before 1996. If the increased velocity in response to shelf collapse was maintained over time, maintaining persistent thinning, eventual ungrounding of the bedrock high where the 1996 grounding line was located would occur independently of ocean-induced increased shelf melt. The recent accelerations and enhanced thinning (Walker and Gardner 2017, Friedl et al. 2018, Gardner et al. 2018) may indicate an ongoing response to the WIS collapse, amplified by positive feedbacks within the FG system.

Rapid sliding at the base is dependent on the presence of a sub-glacial hydrologic system. Evidence suggests that increased basal water supply could accelerate basal motion of both mountain glaciers (Bartholomaus et al. 2008) and ice sheets (Hoffman et al. 2011), presumably by changing the subglacial water pressure or bed contact, and further contribute to grounding line retreat of marine-based glaciers. Jenkins (2011) has also suggested that subglacial water emerging at the grounding line can enhance local ice shelf basal melt rates by driving buoyancy driven plumes in the ocean cavity. The modelled rapid sliding and high friction heating in the upstream FG (Figs. 4.4a, 4.4b), together with the direction of the hydraulic potential gradient (Fig. 4.5), suggest an extensive active hydrologic system beneath the FG, which might already have been enhanced by the previous significant WIS collapse that occurred before 2008.

We hypothesize that high basal friction heating in the fast-flowing regions of the FG is the main source of meltwater flowing into the FG downstream basin. It is also clear

that the modelled friction heating in 2015 was greater than in 2008 in the upstream basin (Fig. 4.4c), with the increase in basal meltwater production peaking over the bedrock rise between the downstream and upstream basins (see Sec. C2 and Fig. C4). The plateaus in hydraulic potential in both downstream and upstream basins of the FG (Fig. 4.5b) suggest the possibility that basal water may accumulate in those regions, or at least show a low throughput. The downstream plateau appears to be fed by a large frictional heat source over the ridge between the downstream and upstream basins in addition to flow from further inland, while the upstream plateau appears to be fed by an extensive upstream region of basal melting. There might be some pooling of water in those plateaus in 2008, but the inferred basal shear stress (Fig. 4.3a) and the height above buoyancy (Fig. 4.6a) indicate that those regions should still remain grounded. According to our hydraulic potential calculations (Fig. 4.5b), outflow from the upstream plateau region is likely to be predominantly in the direction of the downstream basin, but future outflow across the shallow saddle in hydraulic potential towards the southern branch of the FG cannot be ruled out, since the evolution of the potential responds to the changing elevation (Fig. 4.2a) as discussed above.

The further abrupt speed-up events that occurred in 2010-2011 reported by Friedl et al. (2018) could have several potential causes in addition to the previously proposed mechanism of a direct response to ocean-induced melting (Walker and Gardner 2017). One possibility is an outburst of subglacial water from the upstream basin after building up over years to decades in response to increased sliding and friction heating and progressive lowering of the ice surface. Another possibility is local unpinning near the retreating grounding line: ungrounding from pinning points may cause a step reduction in basal resistance. This unpinning could be a feature of ongoing thinning in response to WIS collapse, as discussed above. Another possible cause could be a positive feedback in the subglacial hydrologic system – rapid change may result from the direct feedback between changes in sliding speed, friction heat and basal water production, as discussed in Sec. 4.5.2.

The height above buoyancy is an indicator for the vulnerability of marine-based grounded ice to dynamic thinning and acceleration. The area with $Z_* < 20$ m in 2015 has shown that the downstream basin is currently ungrounding and this may continue until the grounding line finds a stable position on the prograde slope separating the two major basins. More thinning would be needed to destabilise the upstream basin, and it is hard to estimate how much forcing would be needed to push the grounding line into the upstream basin boundary. If the retrograde slope of the upstream basin is reached, further rapid and extensive grounding line retreat would be expected. A clear decrease can be seen in Z_* from 2008 (red in Fig. 4.6a) to 2015 (dark red in Fig. 4.6b) in the upstream basin (around the 2008 velocity contour of 1000 m yr^{-1}), indicating the potential vulnerability of the FG to continued ice mass loss. The surface lowering rate between 2008 and 2015 in this region is ~4.6 m yr^{-1} (Zhao et al. 2017). If this thinning rate continues, the ice in regions with Z_* of 200-300 m would be expected to unground in ~45-65 years. This could take a longer or shorter period since the future thinning rate cannot be expected to remain constant.

In the absence of precise and accurate knowledge of bed topography and ice shelf/stream basal processes, the cause of the recent FG ungrounding cannot be determined. Further research is necessary to better understand the interplay of a range of possible mechanisms.

4.7 Conclusion

We used a Stokes ice dynamics model (Elmer/Ice) at high spatial resolution to estimate the basal shear stress, temperature and friction heating of the Wordie Ice Shelf-Fleming Glacier system in 2008 and 2015. Both increased surface velocity and surface lowering during this period are important for the calculation of basal shear stress.

Decreased basal friction from 2008 to 2015 in the Fleming Glacier downstream basin indicates significant grounding line retreat, consistent with change in the suggested floating area based on the geometry in 2015 and the deduced grounding line in 2014 from Friedl et al. (2018). Grounding line retreat also occurred on the southern branch of the FG. Our height above buoyancy calculations also indicate the FG downstream basin was close to flotation in 2015 and is vulnerable to continued ice thinning and acceleration.

Pronounced basal melting driven by oceanic warming in Marguerite Bay may have triggered the ungrounding of the Fleming Glacier front in early 2008, as previously suggested by Walker and Gardner (2017) and Friedl et al. (2018), but ongoing thinning following the collapse of Wordie Ice Shelf may also provide an explanation. In either case, feedbacks in the subglacial hydrologic system may be a significant factor in reducing basal shear stress, leading to rapid increases in basal sliding and ongoing ungrounding. The derived basal shear stress distributions suggest a major influence could have been the ungrounding of some sticky spots of higher basal shear near the ice front of the main Fleming Glacier, as basal friction under most of the region considered afloat by 2015 was already low in 2008 (a possible subglacial cavity).

The marine-based portion of the Fleming Glacier extends far inland. It is not clear whether grounding line retreat into the Fleming Glacier upstream basin will occur without further forcing. Transient simulations with improved knowledge of bed topography are necessary to predict the movement of the grounding line and how long it will take to achieve a new stable state. Coupled ice sheet ocean modelling will be required to explore the evolution of the ice shelf melting and impact of buttressing from the remaining and new ice shelf on the grounded glacier. Future studies of the dynamic evolution of the Fleming Glacier system will enhance our understanding of its vulnerability to marine ice sheet instability and provide projections of its future behavior.

Chapter 5

Discussion and conclusion

5.1 Main Findings

With rapid regional oceanic and atmospheric warming, the WIS has experienced continuous retreat and disintegration in the past 50 years. High-resolution elevation data over 2002 to 2014 reveals an increase in surface lowering rate of the glaciers of the Fleming system over this period and since 1966. With the high-resolution quantification of ice mass change since the ice shelf breakup in 1966, the solid Earth deformation has been simulated at three GPS sites near the Fleming Glacier. Comparison between simulated and observed bedrock deformation suggests a 1-2 orders of magnitude greater upper mantle viscosity in the southern AP than the region 500 km further north.

The observed surface lowering of the Fleming system over the past five decades represents an opportunity to further understand glacier responses to ice shelf disintegration. A Stokes ice sheet model Elmer/Ice was used to simulate the basal shear stress of the WIS-FG system with an inverse method and a multi-cycle spin-up scheme. The basal shear stress of the Fleming system in both 2008 and 2015 was inferred from the observed surface velocities and surface elevations at both epochs. Sensitivity tests exploring the response of the inverse modelling to various parameters and boundary conditions have been discussed. A multi-cycle temperature spin-up procedure was developed to minimize the influence of initial assumptions about the englacial temperature distribution. Comparison of basal shear stresses between 2008 and 2015 suggested migration of the grounding line by ~9 km upstream by 2015, with the 2008 grounding line position being similar to the 1996 position. This was consistent with calculated height above buoyancy changes during this period. The positive feedback at the bed between the basal sliding and the increases in subglacial water pressure through increased frictional heating is suspected as the reason behind the rapid acceleration, increased thinning, and ungrounding processes.

This study shows that the Fleming system is still far from reaching a new equilibrium state since the floating ice shelf retreat and collapse started in the 1960s. Further transient simulation coupled with ocean modelling and basal hydrological modelling would be required to accurately simulate the past behavior and predict the future movement of the Fleming system and understand better the ice dynamics and its future contribution to sea level. However, the work of this thesis has developed the observational record and modelling framework that could underpin such transient simulations.

Each of the thesis objectives outlined in Chapter 1 has been achieved, as summarized:

Objective 1: Quantify the ice unloading history from 1966 to 2015 and explore the viscoelastic properties of the southern Antarctic Peninsula by comparing the simulated and observed bedrock deformation.

- The elevation change rate of glaciers feeding the WIS was quantified over 1966-2015. A DEM in 1966 was generated using historical airborne photography from 1966. Comparison of surface DEM between 1966 and 2008 identified a surface lowering of more than 60 m near the grounding line, which equals to a thinning rate of 1.5 m yr^{-1}. Analysis of IceBridge and ICESat-1/GLAS data spanning from 2002 to 2015 reveals increased ice thinning rates, and the thinning rates of 2008-2015 are more than twice those of 2002-2008 and nearly 4 times those of 1966-2008.
- The viscoelastic bedrock deformation has been simulated at three GPS sites close to the WIS-FG system using a new high-resolution ice unloading dataset from 1966 to 2015 from this study.
- Comparison between the GPS observations and the model predictions revealed a higher viscosity Earth rheology in the southern AP compared to that previously proposed ~500 km further north in the AP, suggesting a north-south gradient in viscosity of 1-2 orders of magnitude. The horizontal velocities, after removal of plate rotation and recent viscoelastic effects, point away from Marguerite Bay. This suggests a continued response to Holocene deglaciation and hence provides further evidence of a relatively strong upper mantle compared with the northern AP, where a near-instantaneous viscous response has been observed.

Objective 2: simulate the basal shear stress of the WIS-FG system and test the sensitivity of inverse modelling to bedrock datasets, ice front position, and ocean-pressure boundary conditions.

- The basal friction coefficients of the WIS-FG system in 2008 was simulated using the Stokes Elmer/Ice model with an inverse method.
- A multi-cycle spin-up scheme was developed to reduce the sensitivity of the inversion to the initial temperature assumption.
- Sensitivity of inverse modelling to various bedrock elevation datasets, ice front positions, ocean-pressure boundary conditions was investigated.

Objective 3: simulate the basal shear stress of the WIS-FG system in 2008 and 2015 and explore the mechanism behind the rapid dynamic changes that occurred during this period.

- The basal shear stress of the WIS-FG system in 2008 and 2015 was simulated using the same model set-up and spin-up scheme as in the previous chapter.
- Comparison of the inversions for basal shear stresses for 2008 and 2015 suggests the grounding line in 2015 has migrated by ~9 km upstream of the 2008 position (similar to the 1996 position).

- The computed height above buoyancy in both 2008 and 2015 indicated changes in floating area that are consistent with the inferred changes in basal friction.
- The retrograde bed underneath the Fleming Glacier has likely promoted the significant migration of its grounding line. The increase in basal sliding and grounding line retreat might be caused by increased subglacial water volume and/or pressure through greater frictional heating at the bed further upstream in the fast-flowing region.

5.2 Future directions

Several potential areas of future research emerge from this thesis:

- Time series of basal shear-stress:

  The inverse modelling for the fast-flowing regions shows sensitivity to the accuracy of bedrock elevation datasets, ice front positions, and ocean-pressure boundary conditions. The results show that more accurate bedrock topography data and grounding line/ice front positions can be expected to improve the inferred basal shear stress of this system.

  With recent time-series of surface velocities of Fleming Glacier for the past two decades, time-series of basal shear stress of the Fleming system could be simulated using the model set-up and spin-up scheme of this study. This would provide additional details about the changing ice dynamics and help to better constrain the grounding line movement from 1996 position to the present location.

- Coupled ice sheet-ocean modelling for the Fleming Glacier system:

  The relationship between ocean-driven basal melting and the dynamic changes of the feeding glaciers is still uncertain. To understand the mechanism behind the rapid dynamic changes from 2008 to 2015, a transient simulation with a coupled ice sheet-ocean model will be required to explore the buttressing effect of the remnant ice shelf, the evolution of the new ice shelf, and the effect of the sub-shelf melting driven by the ocean-warming.

  To quantify the subglacial water pressure at the ice-bed interaction region, a transient simulation with a coupled ice sheet-hydrological model could be used to model the subglacial water flow and changes in basal water volume and pressure resulting from the changing frictional heating from 2008 and 2015.

  The thickness of the remnant ice shelf in this system is necessary to simulate the sub-shelf melting and the buttressing on the calving front. The effect of the changes in subglacial water pressure on the basal motion and grounding line movement should be explored.

  With a comprehensive set of observations and constraints on the decadal dynamic changes of the Fleming Glacier system, a forward transient

simulation starting from 2008 or 2015 with a coupled ice sheet ocean model could be conducted to explore the recent history and predict the future motion of the WIS-FG system. The question about the time required for the glaciers to reestablish a new equilibrium may be answered. This could also be a good setting for validation exercises for coupled ice sheet-ocean modelling, and exploration of the many processes involved in marine ice sheet retreat that would be beneficial to projections of future sea level contributions from the West and East Antarctic Ice Sheets from large-scale coupled ice sheet ocean models.

- Transient simulation of the past history of the Fleming Glacier system in order to infer quantitative viscoelastic properties of the bedrock in the southern Antarctic Peninsula:

  Based on the ice front positions and hydrostatic equilibrium, the domain of the WIS-FG system could be established with a 3D estimate of the ice shelf in 1966. A transient simulation starting from 1966 could then be implemented to simulate the velocity changes since 1966. The transient simulation could be evaluated by comparing the predicted and observed surface velocity and elevation changes in recent decades. The mechanism behind the ice dynamics changes since the commencement of ice shelf collapse could be explored. The response time of the feeding glaciers to the ice shelf disintegration could then be quantified.

  To better understand the response of the solid Earth to the ice mass changes in the southern AP, the specific viscoelastic properties of this region still need to be identified quantitatively. The transient simulation starting from 2008 or 2015 could provide the ongoing and future glacier loading changes. Combining this with the improved Holocene ice loading history, solid Earth modelling could be conducted to provide more constraints on its viscoelastic deformation with longer and better constraints. High-accuracy and longer GPS time series would help to resolve the remaining uncertainty in the GIA modelling in this region.

5.3 Final Conclusions and Implications

The WIS-FG system now represents one of the best-observed examples of multi-decadal glacier change following ice shelf disintegration. The observed acceleration, increased dynamic thinning, and grounding line retreat indicate that it is currently showing no signs of achieving a new equilibrium state. If the Fleming Glacier continues to accelerate and thin, its grounding line could move across the high bed between the downstream and upstream basins unless the buttressing from the newly formed ice shelf is large enough to restore its stability. The combination of various observational datasets with the new Stokes model provides a much-improved ability to understand the future of this glacier system.

Appendix A

A1. Elevation change rate computation using altimetry data during 2002-2015

We collected elevation data from Airborne Topographic Mapper (ATM/ILAM2, Version 2, 2002, 2004, 2008-2011, 2014) (Krabill 2014, updated 2016) and Land, Vegetation, and Ice Sensor (LVIS/LVIS2, Version 1, 2010-2011) (Blair 2010, updated 2016) laser altimetry from Operation IceBridge and pre-IceBridge campaigns, and the level-2 altimetry product GLA12 (Version 34) from Geoscience Laser Altimeter System/Ice, Cloud, and land Elevation Satellite (GLAS/ICESat, Feb 2003 to Oct 2009) (Zwally et al. 2014). The total dataset covers November 2002 to November 2014. All these data (127,8510 points in total; see the flight tracks in Fig. S2) were transformed to the same height datum (ITRF2014, WGS 84 ellipsoid) and the same coordinate system (WGS 84/Antarctic Polar Stereographic).

The airborne sensors (ATM and LVIS) were positioned by differential GPS with instrument calibrations performed each flight (Krabill et al. 2002, Hofton et al. 2008, Blair 2010, updated 2016, Krabill 2014, updated 2016). We estimated the typical relative accuracy of ATM to be better than 15 cm based on crossover points within 10 m each other. Comparison between the near-coincident LVIS footprints along flight lines and the comparison between LVIS and ICESat data has shown elevation differences smaller than 20 cm (Hofton et al. 2008). The precision of ICESat/GLAS data is ~2.1 cm and its absolute accuracy is about 10cm (Kohler et al. 2013).

To extract the elevation change rate, we applied a linear regression to all measurements in each grid cell of 250 m. Here, only grid cells with at least 3 available measurements were used. From these data, we determined elevation change rates (dh/dt) for each grid cell with the fitting error as the rate uncertainty.

We computed the topography variation in the individual cells based on the ASTER 100m DEM product (Cook et al. 2012). For the fast-flowing ice, the median slope across half a cell (125m) is 0.89 degrees equivalent to 1.94 m. We tested estimating a planar slope for each cell but our results were not changed substantially and hence we used the results from the solution without accounting for slope.

For our loading computations we need complete coverage of the three main feeding glacier regions and so we adopted an interpolation approach based on glacier hypsometry, dividing the grid cells into different height bands of 100 m based on their absolute heights above datum. All points with elevation less than 100 m were removed, as they are likely located on the ice shelf or in large crevasses. To each height band we assigned the median dh/dt from the corresponding height band in the altimeter dh/dt dataset. To define the lower bound of dh/dt for the upper reaches of the glacier, we define the dh/dt to be 0 at the height of 1900 m (and above), as indicated by ICESat crossovers in this region.

We evaluated the fit of the hypsometric model to the data for chosen grid cells (those with at least 3 measurements) using a weighted root mean square error (RMSE) statistic by computing the residuals between the interpolated dh/dt from the

hypsometric model and the extracted dh/dt of each grid cell with the weight from the fitting error. In the computation, we also excluded the grid cells with residuals greater than 3 times the RMSE (red points in Fig. 2.3). So 2048 grid cells out of 2199 cells were chosen for the period over 2002-2008 (black points in Fig. 2.3c), and 1089 grid cells out of 1402 cells were chosen for the period over 2008-2015 (black points in Fig. 2.3d). The RMSEs before and after 2008 are 0.89 m/yr and 0.20 m/yr, respectively.

A2. Elevation changes during 1966-2008

To generate the 1966 DEM, we used both vertical and oblique (left and right) imagery from the trimetrogon camera scanned at 100 dots-per-inch by United States Geological Survey (USGS). We used imagery from flight CA1834 flown on 28th November 1966, captured at elevations between 5000 and 6000 m above sea level. The photographic scans were corrected to reduce noise and balance exposure and contrast between the three sets of concurrently acquired photos. The DEMs were generated using Agisoft PhotoScan Professional. The Photoscan processing involves point detection and alignment of the photographic data sets using structure from motion algorithms (Ullman 1979). Once aligned, a sparse set of stable control points (well-defined non-snow-covered mountain peaks) was located within the photographs. The coordinates for these control points were derived from the SPOT DEM for January 10th 2008 (Korona et al. 2009). Once registered the sparse point cloud is enhanced through dense multi-view stereo algorithms to produce a detailed surface geometry, from which a DEM and associated orthophotography were produced (Verhoeven 2011).

To compare the 1966 DEM with the 2008 SPOT DEM (Korona et al. 2009), the SPOT DEM data was cropped to the same region as the 1966 DEM, and masked for regions of poor correlation using the supplied SPOT mask. The 1966 DEM was then registered to the SPOT DEM data using areas of stable terrain (defined by slow-flowing ice) and surface matching routines in CloudCompare software version 2.6.3 (http://www.cloudcompare.org). RMSE across the stable terrain is <15 m. Given the relative steepness of the stable terrain compared to the glacier, we regard this as an upper bound on the likely accuracy of glacier elevation change estimates.

A3. Conversion from volume to mass

To convert from elevation change to mass change, we consider the effects of firn compaction and SMB anomalies based on the RACMO2.3/ANT5.5 SMB and firn densification models (FDM). We subtracted the firn thickness change rates from the observed dh/dt to get the elevation rates solely due to ice dynamics, which were converted to mass changes by applying the density of pure ice (917 kg/m^3). To obtain the total mass changes, we added back the yearly cumulative SMB anomalies. The firn column thickness rates from 1980 to 2013 were computed using the monthly output of the 1-dimensinal FDM forced by the RACMO2.3/ANT5.5 model (Ligtenberg et al. 2014). The SMB anomaly data over 1979 to 2013 was summed from the anomalies computed using monthly SMB data simulated by the RACMO2.3/ANT5.5 model over 1979-2013 (van Wessem et al. 2016). Considering

that those data do not fully cover our study period from 1966 to 2015, we needed to extrapolate to the most recent few years and before 1979. Examining the time series of SMB and firn thickness change showed that both remained stable over the past few decades (Fig. A3). We validated the uncertainty of the FDM and SMB anomalies for the years before 1979 by using the maximum or minimum value for this period, which resulted in changes of up to ± 0.40 m/yr, which are small compared with the observed total elevation changes. Consequently, for the firn correction rate we extrapolated using the 1979-2013 mean and, for SMB anomalies, we used the 1979-2013 mean for years prior to 1979 and the 2013 values for 2014 and 2015.

Elastic and viscoelastic deformations were computed via an array of circular disks, each with radius of 0.5 km. So we convert the water equivalent ice height of each disc based on the requirement that mass must be conserved in each cell.

To explore uncertainty in this model-based approach we follow Wouters et al. (2015) and Berthier et al. (2012) and assume mass loss is completely due to changes in ice dynamics and adopt a column-averaged density of 900 kg/m^3. We also test the effect of adopting a much lower column-averaged density (700 kg/m^3). For the former, the background uplift rate at the TRVE site suggested that the UMV should be greater than 4×10^{19} Pa s (Fig. A5a). Using an extremely low value of 700 kg/m^3 suggests an UMV lower bound of 2×10^{19} Pa s (Fig. A5b).

We found little sensitivity to changes in the adopted 1966-2008 elevation lowering. Using a value of 100 m, instead of 60 m, for the front of Fleming Glacier (Fig. 2.5) we found a preference for a slightly higher UMV of $> 1\times10^{20}$ Pa s (Fig. A6).

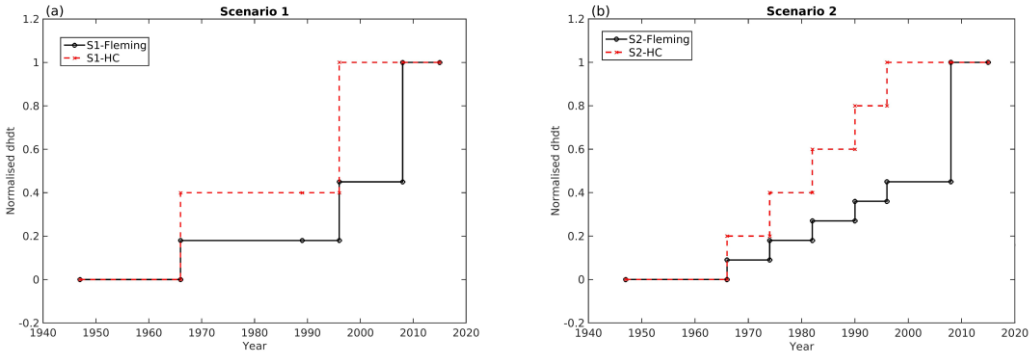

Figure A1. Two scenarios of normalized surface elevation change since 1947. The black solid line is for the Fleming system, and the red dashed line is for the HC system. The glacier-thinning rate has been normalized to a value between 0 and 1, where 1 refers to the ice surface elevation change rate after 2008.

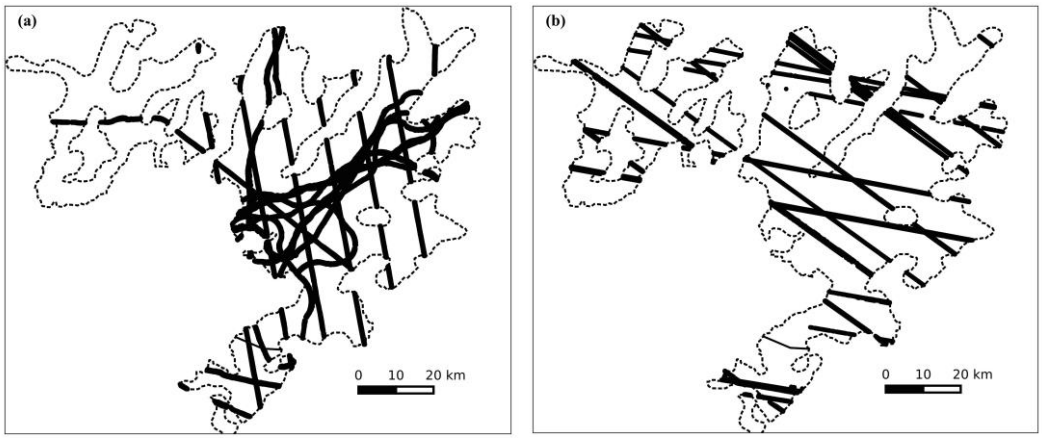

Figure A2. Flight track points of the (a) ATM2, ILVIS2 from 2002 to 2014 and (b) GLAS/ICEsat data from 2002 to 2009.

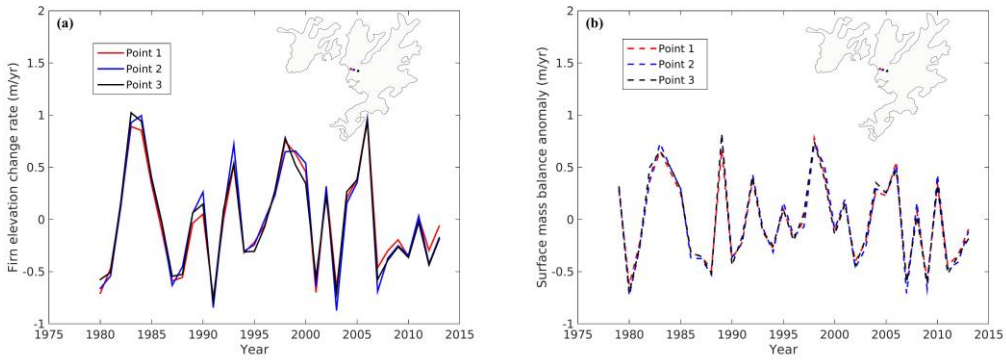

Figure A3. (a) Firn elevation change rate (metres water equivalent per year) from 1980 to 2013 and (b) surface mass balance anomalies (metres water equivalent per year) from 1979 to 2013 at three points near the front of Fleming Glacier (inset shows location of three points)

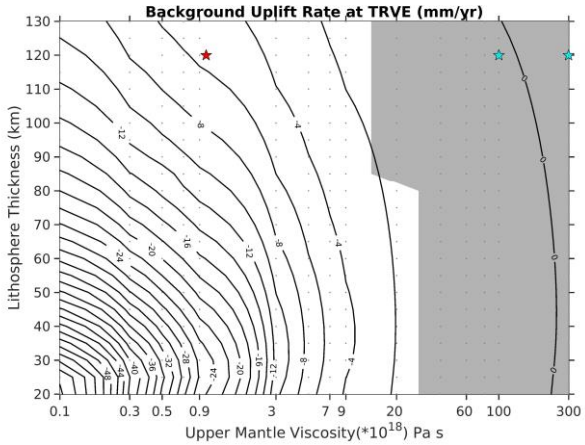

Figure A4. Background uplift rate at TRVE with the ice loading history in Scenario 1. The red star is the best fit model for the northern AP from Nield et al. (2014), and the cyan stars span the range of upper mantle viscosities preferred by Wolstencroft et al. (2015). The black lines are contours of the implied vertical background rate. The gray shading areas indicate the Earth models with background rate greater than or equal to zero while considering measurement uncertainty (i.e., > $-2\sigma_V$).

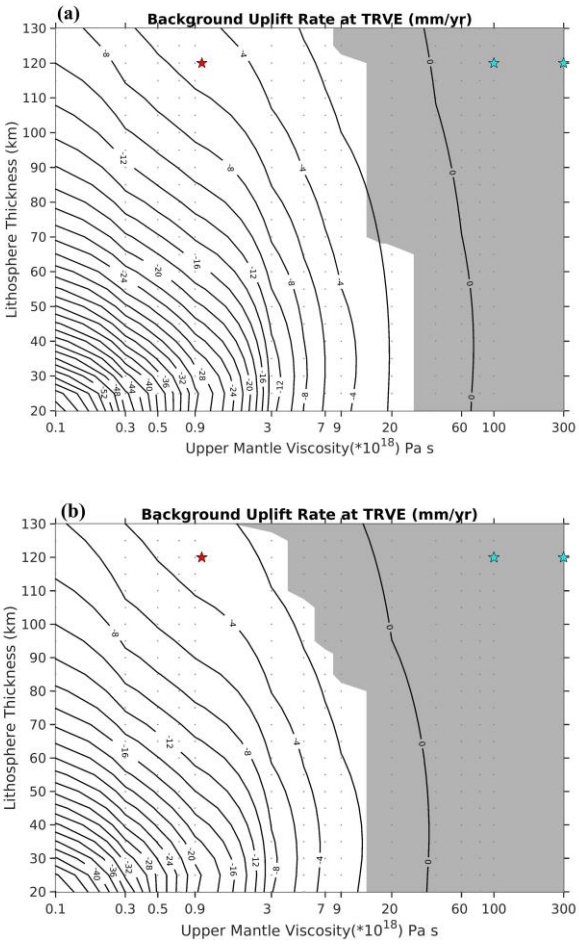

Figure A5. Estimated pre-1966 background uplift rates as a function of viscoelastic model setup at TRVE with average density of (a) 900 kg/m^3 and (b) 700 kg/m^3 by assuming the steady state surface mass balance in the past decades. The other parts are the same as Fig. A4.

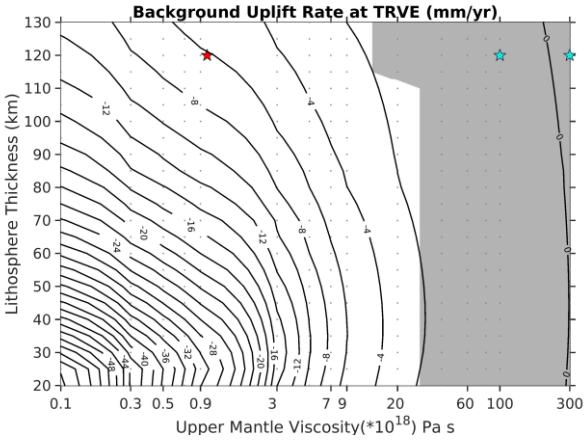

Figure A6. Estimated pre-1966 background uplift rates as a function of viscoelastic model setup at TRVE assuming a surface lowering of 100 m over 1966-2008. The other parts are the same as Fig. A4.

Appendix B

Table B1. The Root Mean Square Deviation (RMSD) between the observed and relaxed surface elevation for the fast-flowing region of the Fleming Glacier (>1500 m yr^{-1}) in each cycle of Experiment TEMP1, CTRL, TEMP2, TEMP3.

Experiment	RMSD (m)		
	Cycle1	Cycle2	Cycle3
CTRL	19.35	13.64	13.09
TEMP1	15.39	13.66	13.05
TEMP2	21.15	13.32	12.57
TEMP3	15.39	13.88	13.53

Table B2. The RMSD of the simulated basal friction coefficients *C* between Experiments TEMP1-3 and CTRL for each cycle for the fast-flowing region of the Fleming Glacier (>1500 m yr^{-1}).

RMSD (MPa m^{-1} yr)	CTRL		
	Cycle1	Cycle2	Cycle3
TEMP1	1.00e-2	1.55e-4	9.16e-5
TEMP2	6.30e-3	6.97e-5	1.56e-5
TEMP3	3.40e-3	4.86e-5	2.94e-5

Table B3. The RMSD of the magnitude of the simulated basal velocity between Experiments TEMP1-3 and CTRL for each cycle for the fast-flowing region of the Fleming Glacier (>1500 m yr^{-1}).

RMSD (m yr^{-1})	CTRL		
	Cycle1	Cycle2	Cycle3
TEMP1	438.50	196.65	118.36
TEMP2	244.21	68.70	18.99
TEMP3	230.54	62.91	30.68

Table B4. The RMSD between the simulated temperature and the initial temperature assumption for each cycle for the fast-flowing region of the Fleming Glacier (>1500 m yr^{-1}). For TEMP3, we took the linear temperature profile as the initial temperature assumption.

Experiment	RMSD (℃)		
	Cycle1	Cycle2	Cycle3
CTRL	5.05	6.69	7.20
TEMP1	7.91	8.21	8.29
TEMP2	8.25	9.27	9.49
TEMP3	4.50	6.88	7.24

Table B5. The RMSD between the observed and simulated surface speed for the fast-flowing region of the Fleming Glacier (>1500 m yr^{-1}).

Experiment	RMSD (m yr^{-1})		
	Cycle1	Cycle2	Cycle3
CTRL	86.49	75.75	75.12
TEMP1	88.52	80.78	80.65
TEMP2	86.03	79.27	78.07
TEMP3	87.16	79.10	78.48
EF1	x	x	86.35
EF2	x	x	89.38
EF3	x	x	993.20
BEDMC	x	x	62.60
BEDZC	x	x	61.78
IFBC1	x	x	79.38
IFBC2	x	x	72.68
IFBC3	x	x	249.64

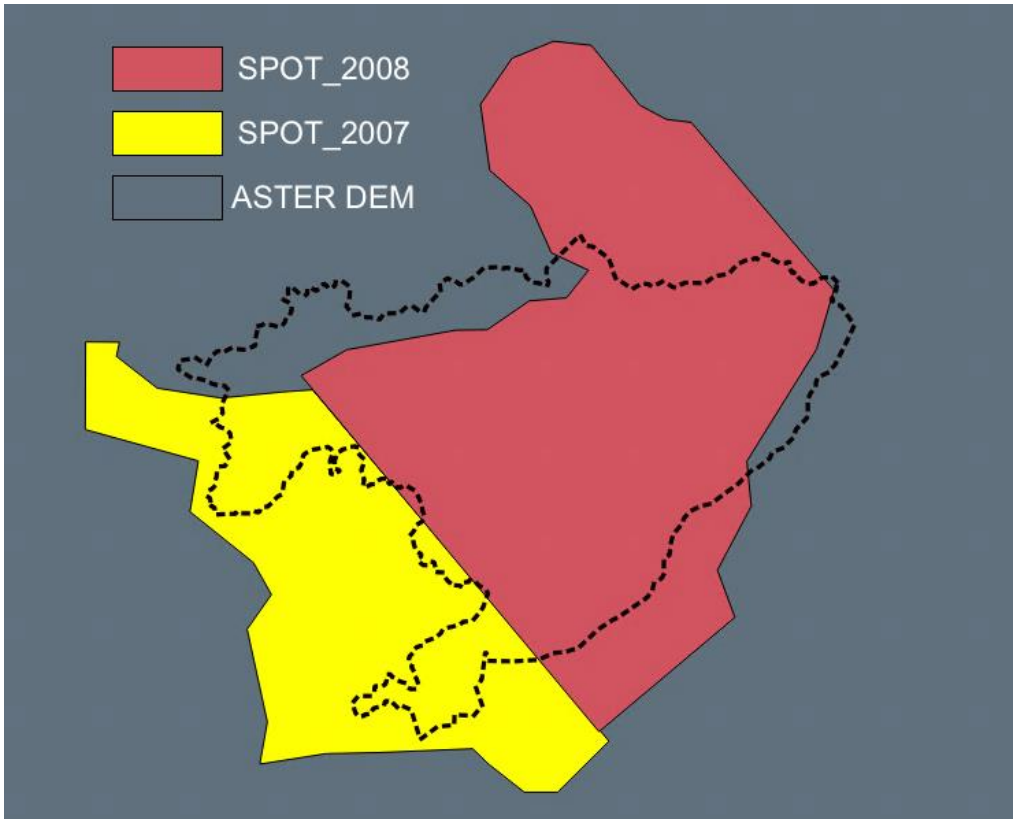

Figure B1. The masks of DEM products used to generate the surface topography in 2008. The polygons represent the SPOT DEM product acquired on 21st Feb, 2007 (yellow) and 10th Jan, 2008 (red) and an ASTER DEM product ranging from 2000 to 2009 (grey), respectively.

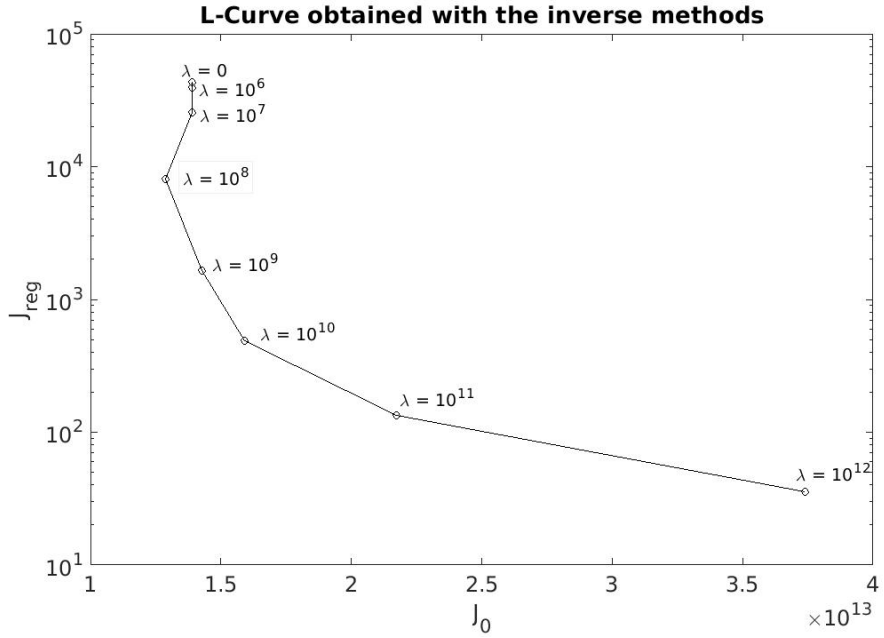

Figure B2. L-curve obtained with the inverse method of Experiment CTRL.

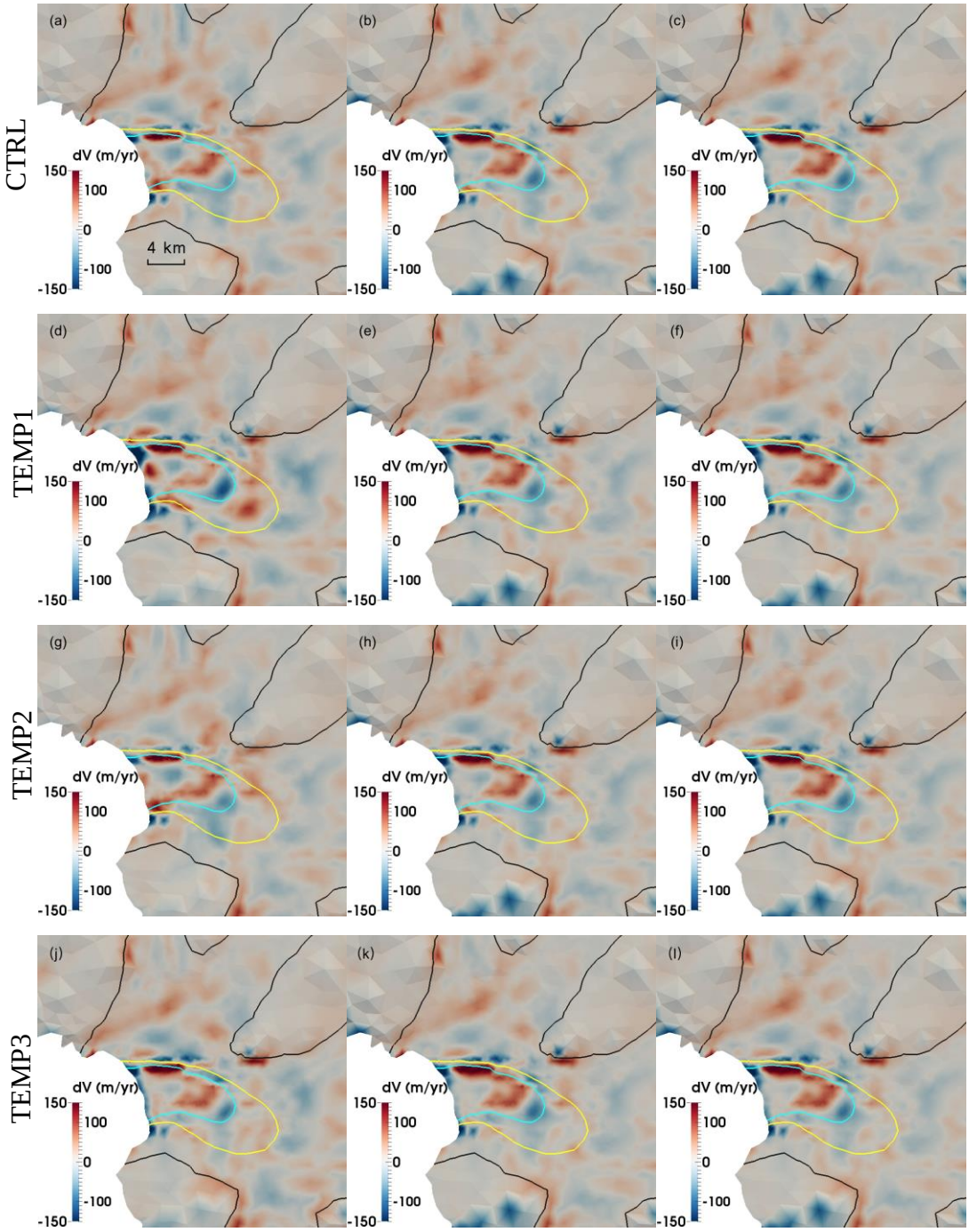

Figure B3. Mismatch between the observed and simulated surface speed in 2008 (observed minus simulated) from experiments: (a-c) CTRL, (d-f) TEMP1, (g-i) TEMP2, and (j-l) TEMP3. The left (a, d, g, j), middle (b, e, h, k) and right columns (c, f, i, l) are from Cycle 1, Cycle 2 and Cycle 3, respectively. The black, yellow and cyan solid lines represent observed surface speed contours of 100 m yr^{-1}, 1000 m yr^{-1}, and 1500 m yr^{-1}, respectively.

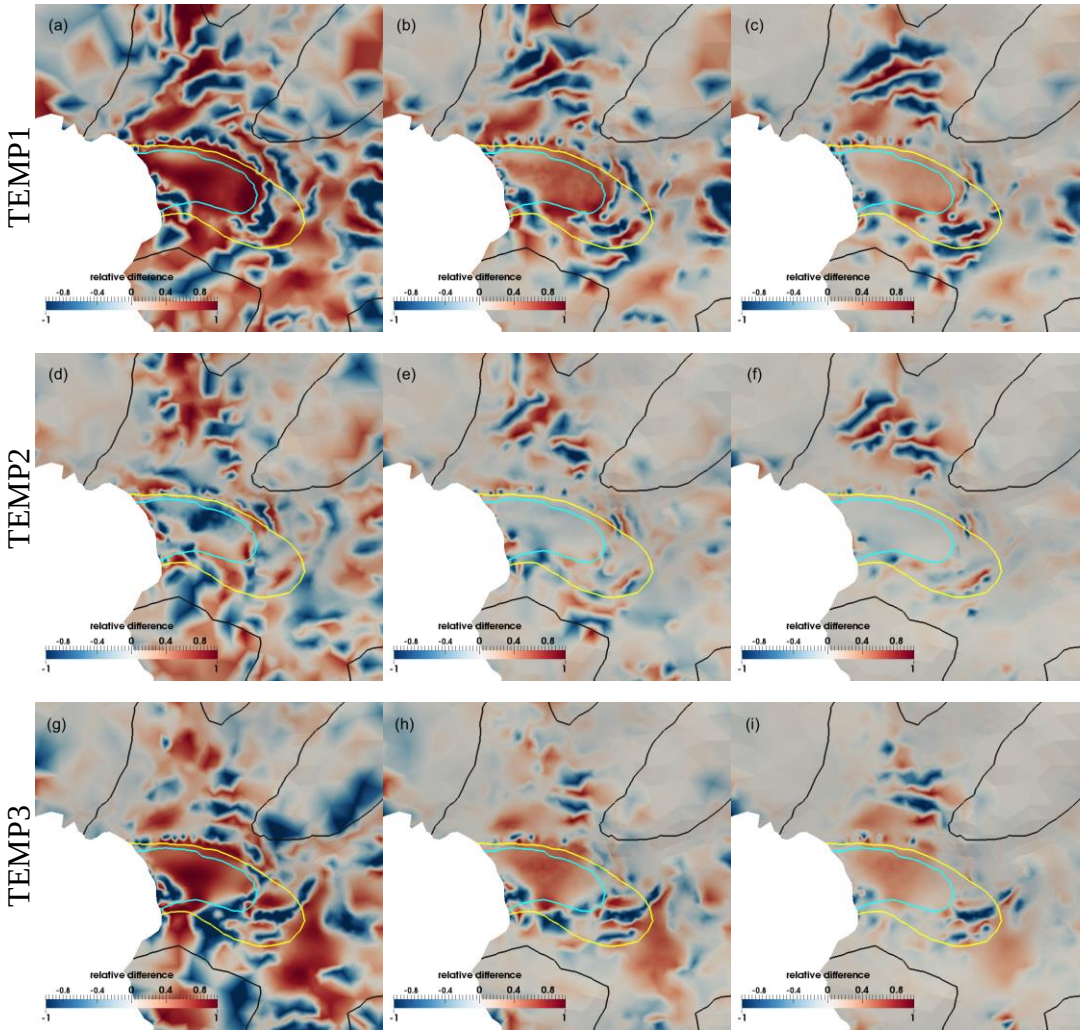

Figure B4. Normalised relative differences of basal drag coefficients C between experiments (a-c) TEMP1 (first row), (d-f) TEMP2 (second row), (g-i) TEMP3 (third row), and CTRL after Cycle 1 (left column), Cycle 2 (middle column), and Cycle 3 (right column). Taking (a) for example, the plot is the result of $(C_{CTRL}-C_{TEMP1})/C_{CTRL}$. The black, yellow and cyan solid lines represent observed surface speed contours of 100 m yr^{-1}, 1000 m yr^{-1}, and 1500 m yr^{-1}, respectively.

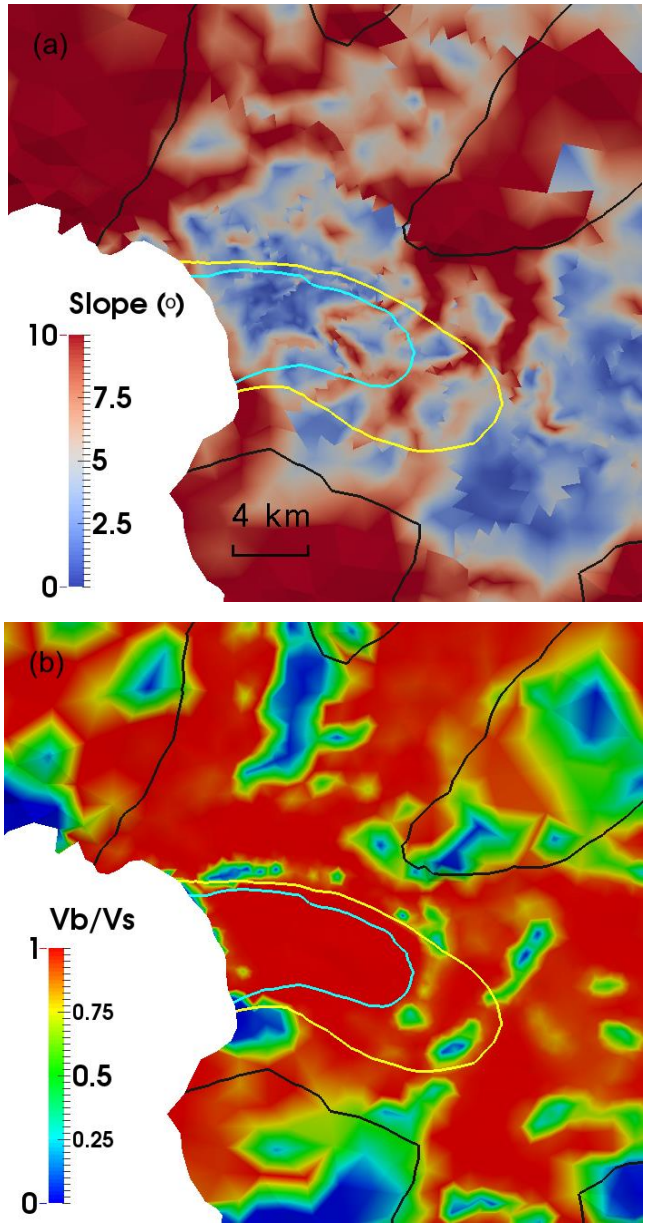

Figure B5. (a) The slope (in degrees) of the relaxed surface and (b) the ratio of magnitude of the modeled basal and surface velocity (basal over surface) after three-cycle spin-up scheme from experiment: CTRL. The maximum difference around the ice front is ~2240 m yr^{-1}. The zigzag discontinuities in (a) are artefacts of the post-processing at partition boundaries only, and do not affect the simulations. The black, yellow, and cyan solid lines represent surface speed contours of 100 m yr^{-1}, 1000 m yr^{-1}, and 1500 m yr^{-1} respectively.

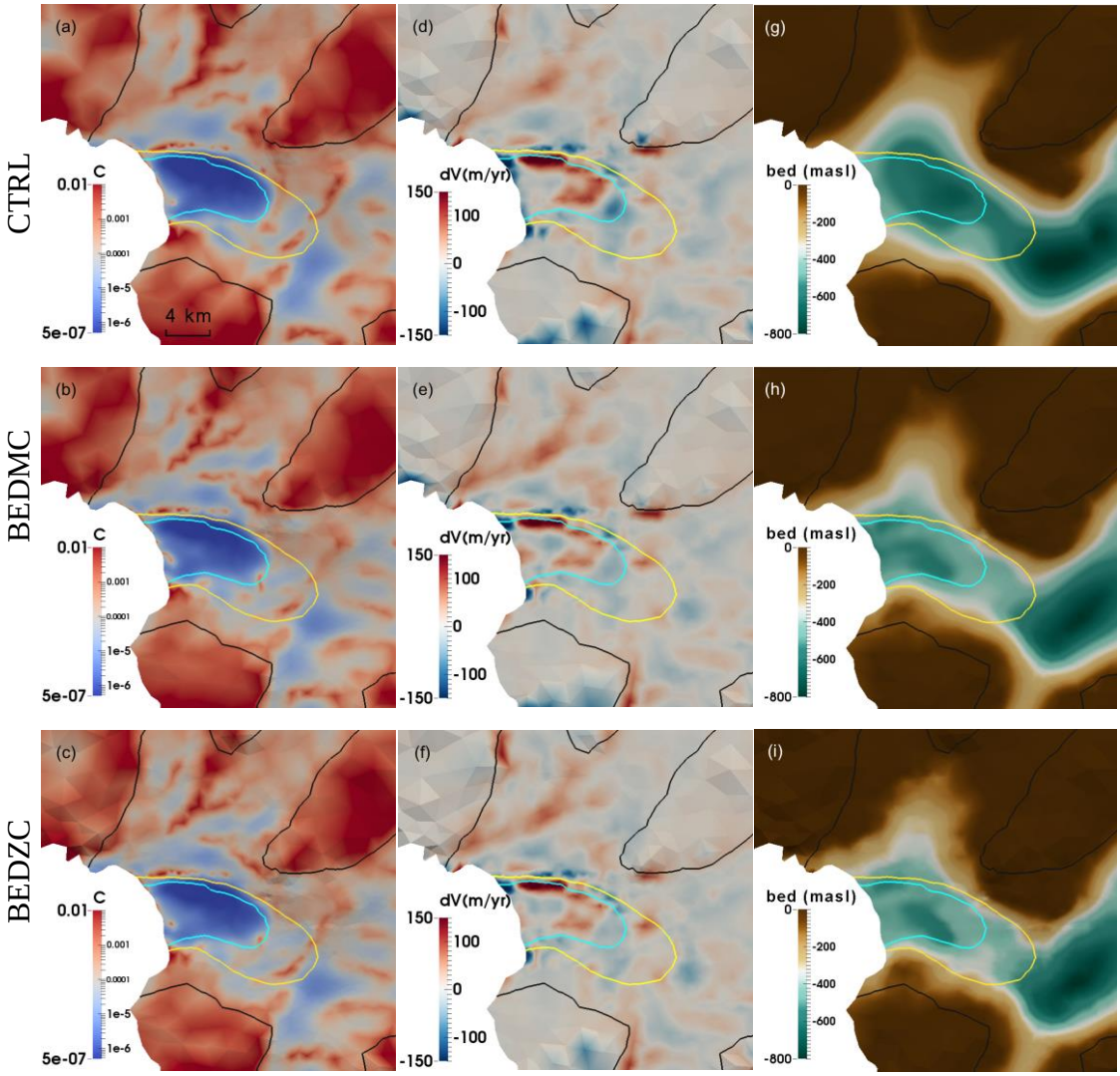

Figure B6. Distribution of basal friction coefficient C (MPa m^{-1} yr) (left column) and mismatch between the observed and modeled surface velocity (observed minus simulated; middle column) from experiments: (a, d) CTRL (first row), (b, e) BEDMC (second row), and (c, f) BEDZC (third row) with bedrock data (meters above sea level, masl) from (g) bed_bm; (h) bed_mc; (i) bed_zc, respectively. The black, yellow, and cyan solid lines represent observed surface speed contours of 100 m yr^{-1}, 1000 m yr^{-1} and 1500 m yr^{-1}, respectively.

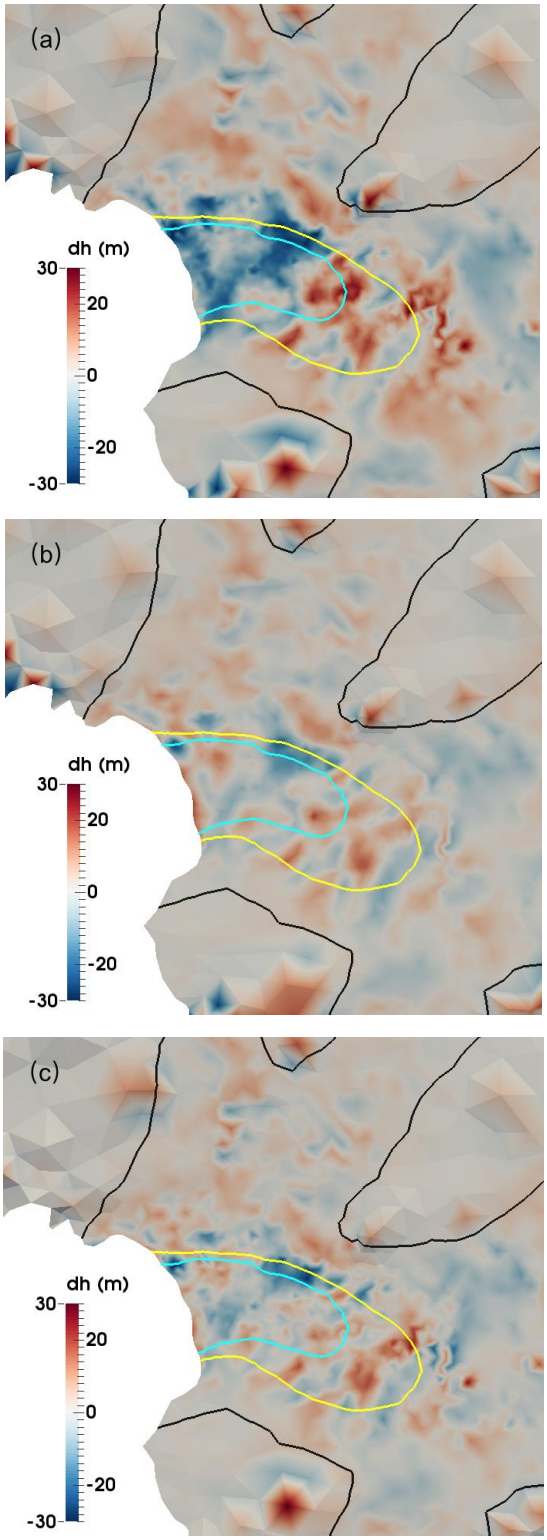

Figure B7. The mismatch between the observed and relaxed surface elevation (observed-relaxed) after the third cycle from experiments (a) CTRL, (b) BEDMC, and (c) BEDZC. The black, yellow, and cyan solid lines represent surface speed contours of 100 m yr^{-1}, 1000 m yr^{-1}, and 1500 m yr^{-1}, respectively.

Appendix C

C1. Sensitivity to velocity changes

Figure C1 shows the results from the inversion for basal shear stress in 2008 (Fig. C1a), 2015 (Fig. C1b), and from another additional inversion with the geometry from 2008 but using surface velocity from 2015 (Fig. C1c). The basal shear stress of this hybrid simulation shows patterns and magnitudes between those of the standard 2008 and 2015 simulations. This suggests that changes in both ice geometry and velocities have comparable impact on the inferred basal shear stress distribution, with the implication that an inversion study based on a change in either velocity or geometry alone would underestimate the change in basal drag.

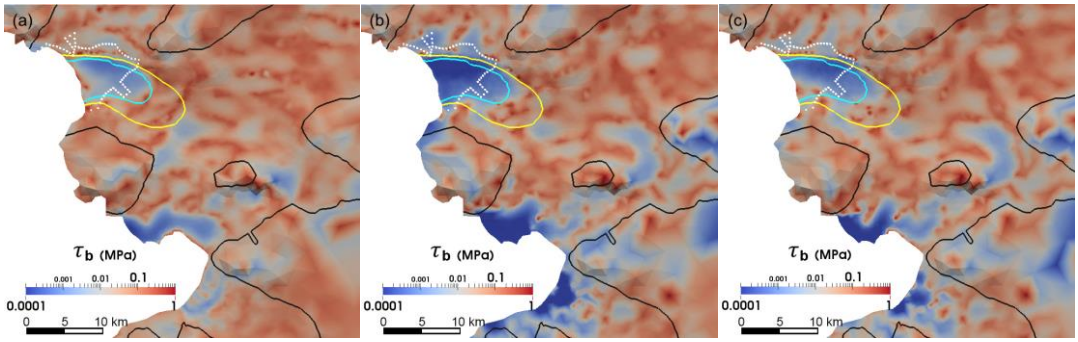

Figure C1. Basal shear stress, τ_b, for (a) 2008, (b) 2015, and (c) a simulation using topography from 2008 and velocity from 2015. The white dotted line represents the grounding line in 2014 estimated by Friedl et al. (2018). The black, yellow and cyan solid lines represent the 2008 surface speed contours of 100 m yr^{-1}, 1000 m yr^{-1}, and 1500 m yr^{-1}, respectively.

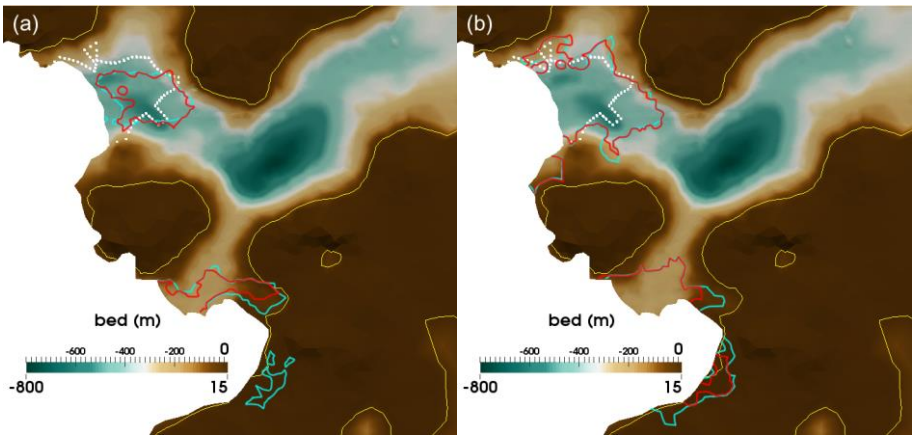

Figure C2. The boundaries of area with τ_b<0.01 MPa (blue lines) and RBD < 0.1 (red lines) in (a) 2008 and (b) 2015. The background image is the bed elevation data in this study. The white dotted line represents the deduced grounding line in 2014 from Friedl et al. (2018). The yellow contour is the sea level of 15 m.

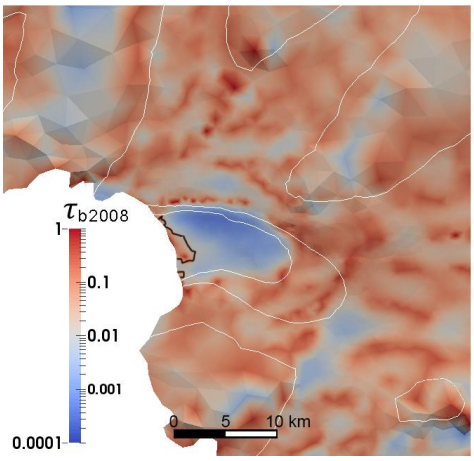

Figure C3. The basal shear stress of the fast-flowing region of the Fleming Glacier in 2008. The black solid line represents the boundary of are with τ_b>0.01 MPa and surface speed higher than 1500 m yr^{-1}. The white solid lines represent the 2008 surface speed contours of 100 m yr^{-1}, 1000 m yr^{-1}, and 1500 m yr^{-1}, respectively.

C2. Basal meltwater calculation

The basal meltwater rate, m_b, is calculated for 2008 and 2015 with equation:

$$m_b = \frac{-Q_r}{LS\rho_{pw}} \quad \text{(C1)}$$

where Q_r is the residual of the heat transfer equation at each basal node, which represents the amount of energy extraction per node per year given that node temperature is at pressure melting point, L is the latent heat of fusion of ice (~33400 J kg^{-1}), S is the area of each mesh element, and ρ_{pw} is the pure water density (1000 kg m^{-3}). The basal friction heating provides the dominant heat source, being orders of magnitude higher than geothermal heating or diffusion through the ice for the fast-flowing regions.

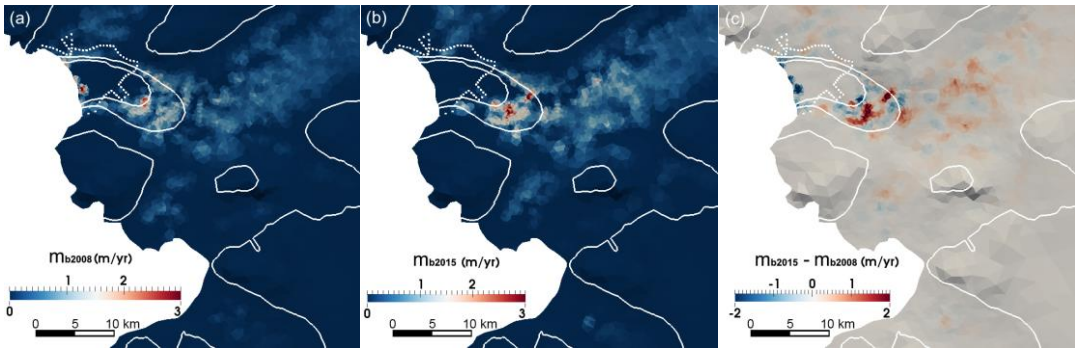

Figure C4. The simulated basal melt water (metres per year) in (a) 2008 and (b) 2015, respectively. (c) The difference of basal melt water between 2008 and 2015 (2015 minus 2008). The white dotted line represents the grounding line in 2014 estimated by Friedl et al. (2018). The white solid lines represent the 2008 surface speed contours of 100 m yr^{-1}, 1000 m yr^{-1}, and 1500 m yr^{-1}, respectively.

Bibliography

A, G., J. Wahr and S. Zhong (2013). "Computations of the viscoelastic response of a 3-D compressible Earth to surface loading: an application to Glacial Isostatic Adjustment in Antarctica and Canada." Geophysical Journal International **192**(2): 557-572.

Altamimi, Z., X. Collilieux and L. Métivier (2011). "ITRF2008: an improved solution of the international terrestrial reference frame." Journal of Geodesy **85**(8): 457-473.

Amundson, J. M., M. Fahnestock, M. Truffer, J. Brown, M. P. Lüthi and R. J. Motyka (2010). "Ice mélange dynamics and implications for terminus stability, Jakobshavn Isbræ, Greenland." Journal of Geophysical Research: Earth Surface **115**(F1): n/a-n/a.

An, M., D. A.Wiens, Y. Zhao, M. Feng, A. A. Nyblade, M. Kanao, Y. Li, A. Maggi and J. J. Lévêque (2015). "S ‐ velocity model and inferred Moho topography beneath the Antarctic Plate from Rayleigh waves." Journal of Geophysical Research: Solid Earth **120**(1): 359-383.

Argus, D. F., W. Peltier, R. Drummond and A. W. Moore (2014). "The Antarctica component of postglacial rebound model ICE-6G_C (VM5a) based on GPS positioning, exposure age dating of ice thicknesses, and relative sea level histories." Geophysical Journal International **198**: 537-563.

Arthern, R. J. and C. R. Williams (2017). "The sensitivity of West Antarctica to the submarine melting feedback." Geophysical Research Letters **44**(5): 2352-2359.

Banwell, A., I. Hewitt, I. Willis and N. Arnold (2016). "Moulin density controls drainage development beneath the Greenland ice sheet." Journal of Geophysical Research: Earth Surface **121**(12): 2248-2269.

Barletta, V. R., M. Bevis, B. E. Smith, T. Wilson, A. Brown, A. Bordoni, M. Willis, S. A. Khan, M. Rovira-Navarro, I. Dalziel, R. Smalley, E. Kendrick, S. Konfal, D. J. Caccamise, R. C. Aster, A. Nyblade and D. A. Wiens (2018). "Observed rapid bedrock uplift in Amundsen Sea Embayment promotes ice-sheet stability." Science **360**(6395): 1335-1339.

Barletta, V. R., C. Ferrari, G. Diolaiuti, T. Carnielli, R. Sabadini and C. Smiraglia (2006). "Glacier shrinkage and modeled uplift of the Alps." Geophysical research letters **33**(14).

Barletta, V. R., L. S. Sørensen and R. Forsberg (2013). "Scatter of mass changes estimates at basin scale for Greenland and Antarctica." The Cryosphere **7**(5): 1411-1432.

Bartholomaus, T. C., R. S. Anderson and S. P. Anderson (2008). "Response of glacier basal motion to transient water storage." Nature Geosci **1**(1): 33-37.

Bentley, M. J., J. S. Johnson, D. A. Hodgson, T. Dunai, S. P. H. T. Freeman and C. Ó Cofaigh (2011). "Rapid deglaciation of Marguerite Bay, western Antarctic Peninsula in the Early Holocene." Quaternary Science Reviews **30**(23–24): 3338-3349.

Berthier, E., T. A. Scambos and C. A. Shuman (2012). "Mass loss of Larsen B tributary glaciers (Antarctic Peninsula) unabated since 2002." Geophysical Research Letters **39**(13).

Blair, B. M. H. (2010, updated 2016). "IceBridge LVIS L2 Geolocated Surface Elevation Product." Boulder, Colorado USA: NASA DAAC at the National Snow and Ice Data Center. .

Borstad, C. P., E. Rignot, J. Mouginot and M. P. Schodlok (2013). "Creep deformation and buttressing capacity of damaged ice shelves: theory and application to Larsen C ice shelf." The Cryosphere **7**(6): 1931-1947.

Carrasco, J. F. (2013). "Decadal Changes in the Near-Surface Air Temperature in the Western Side of the Antarctic Peninsula." Atmospheric and Climate Sciences **Vol.03No.03**: 7.

Christie, F. D. W., R. G. Bingham, N. Gourmelen, S. F. B. Tett and A. Muto (2016). "Four-decade record of pervasive grounding line retreat along the Bellingshausen margin of West Antarctica." Geophysical Research Letters **43**(11): 5741-5749.

Church, J. A., Clark, P. U., Cazenave, A., Gregory, J. M., Jevrejeva, S., Levermann, A., Merrifield, M. A., Milne, G. A., Nerem, R. S., Nunn, P. D., Payne, A. J., Pfeffer, W. T., Stammer, D. and Unnikrishnan, A. S. (2013). "Sea level change." Climate Change 2013: The Physical Science Basis. Contribution of Working Group I to the Fifth Assessment Report of the Intergovernmental Panel on Climate Change [Stocker, T.F., D. Qin, G.-K. Plattner, M. Tignor, S.K. Allen, J. Boschung, A. Nauels, Y. Xia, V. Bex and P.M. Midgley (eds.)].

Cook, A. J., A. J. Fox, D. G. Vaughan and J. G. Ferrigno (2005). "Retreating Glacier Fronts on the Antarctic Peninsula over the Past Half-Century." Science **308**(5721): 541-544.

Cook, A. J., P. R. Holland, M. P. Meredith, T. Murray, A. Luckman and D. G. Vaughan (2016). "Ocean forcing of glacier retreat in the western Antarctic Peninsula." Science **353**(6296): 283-286.

Cook, A. J., T. Murray, A. Luckman, D. E. Vaughan and N. E. Barrand (2012). "A new 100-m Digital Elevation Model of the Antarctic Peninsula derived from ASTER Global DEM: methods and accuracy assessment." Earth System Science Data **4**(1): 129-142.

Cook, A. J., D. Vaughan, A. Luckman and T. Murray (2014). "A new Antarctic Peninsula glacier basin inventory and observed area changes since the 1940s." Antarctic Science **26**(06): 614.

Cook, A. J. and D. G. Vaughan (2010). "Overview of areal changes of the ice shelves on the Antarctic Peninsula over the past 50 years." The Cryosphere **4**(1): 77-98.

De Rydt, J., G. H. Gudmundsson, H. F. J. Corr and P. Christoffersen (2013). "Surface undulations of Antarctic ice streams tightly controlled by bedrock topography." The Cryosphere **7**(2): 407-417.

Depoorter, M. A., J. L. Bamber, J. A. Griggs, J. T. M. Lenaerts, S. R. M. Ligtenberg, M. R. van den Broeke and G. Moholdt (2013). "Calving fluxes and basal melt rates of Antarctic ice shelves." Nature **502**(7469): 89-92.

Doake, C. S. M. (1975). "Bottom sliding of a glacier measured from the surface." Nature **257**(5529): 780-782.

Doake, C. S. M. and D. G. Vaughan (1991a). "Breakup of Wordie Ice Shelf, Antarctica." Glaciers-ocean-atmosphere interactions. Proc. symposium, St. Petersburg, 1990: 161-165.

Doake, C. S. M. and D. G. Vaughan (1991b). "Rapid disintegration of the Wordie Ice Shelf in response to atmospheric warming." Nature **350**(6316): 328-330.

Dunse, T., T. Schellenberger, J. O. Hagen, A. Kääb, T. V. Schuler and C. H. Reijmer (2015). "Glacier-surge mechanisms promoted by a hydro-thermodynamic feedback to summer melt." The Cryosphere **9**(1): 197-215.

Dunse, T., T. V. Schuler, J. O. Hagen and C. H. Reijmer (2012). "Seasonal speed-up of two outlet glaciers of Austfonna, Svalbard, inferred from continuous GPS measurements." The Cryosphere **6**(2): 453-466.

Durand, G., O. Gagliardini, L. Favier, T. Zwinger and E. le Meur (2011). "Impact of bedrock description on modeling ice sheet dynamics." Geophysical Research Letters **38**(20): n/a-n/a.

Dziewonski, A. M. and D. L. Anderson (1981). "Preliminary reference Earth model." Physics of the Earth and Planetary Interiors **25**(4): 297-356.

Favier, L., G. Durand, S. L. Cornford, G. H. Gudmundsson, O. Gagliardini, F. Gillet-Chaulet, T. Zwinger, A. J. Payne and A. M. Le Brocq (2014). "Retreat of Pine Island Glacier controlled by marine ice-sheet instability." Nature Climate Change **4**: 117.

Fieber, K. D., J. P. Mills, P. E. Miller, L. Clarke, L. Ireland and A. J. Fox (2017). "Rigorous 3D change determination in Antarctic Peninsula glaciers from stereo WorldView-2 and archival aerial imagery." Remote Sensing of Environment **205**: 18-31.

Förste, C., R. Schmidt, R. Stubenvoll, F. Flechtner, U. Meyer, R. König, H. Neumayer, R. Biancale, J.-M. Lemoine, S. Bruinsma, S. Loyer, F. Barthelmes and S. Esselborn (2008). "The GeoForschungsZentrum Potsdam/Groupe de Recherche de Gèodésie Spatiale satellite-only and combined gravity field models: EIGEN-GL04S1 and EIGEN-GL04C." Journal of Geodesy **82**(6): 331-346.

Fox Maule, C., M. E. Purucker, N. Olsen and K. Mosegaard (2005). "Heat Flux Anomalies in Antarctica Revealed by Satellite Magnetic Data." Science **309**(5733): 464-467.

Fretwell, P., H. D. Pritchard, D. G. Vaughan, J. L. Bamber, N. E. Barrand, R. Bell, C. Bianchi, R. G. Bingham, D. D. Blankenship, G. Casassa, G. Catania, D. Callens, H. Conway, A. J. Cook, H. F. J. Corr, D. Damaske, V. Damm, F. Ferraccioli, R. Forsberg, S. Fujita, Y. Gim, P. Gogineni, J. A. Griggs, R. C. A. Hindmarsh, P. Holmlund, J. W. Holt, R. W. Jacobel, A. Jenkins, W. Jokat, T. Jordan, E. C. King, J. Kohler, W. Krabill, M. Riger-Kusk, K. A. Langley, G. Leitchenkov, C. Leuschen, B. P. Luyendyk, K. Matsuoka, J. Mouginot, F. O. Nitsche, Y. Nogi, O. A. Nost, S. V. Popov, E. Rignot, D. M. Rippin, A. Rivera, J. Roberts, N. Ross, M. J. Siegert, A. M. Smith, D. Steinhage, M. Studinger, B. Sun, B. K. Tinto, B. C. Welch, D. Wilson, D. A. Young, C. Xiangbin and A.

Zirizzotti (2013). "Bedmap2: improved ice bed, surface and thickness datasets for Antarctica." The Cryosphere **7**(1): 375-393.

Frey, P.-J. and F. Alauzet (2005). "Anisotropic mesh adaptation for CFD computations." Computer methods in applied mechanics and engineering **194**(48): 5068-5082.

Fricker, H. A. and L. Padman (2012). "Thirty years of elevation change on Antarctic Peninsula ice shelves from multimission satellite radar altimetry." Journal of Geophysical Research: Oceans **117**(C2): C02026.

Friedl, P., T. C. Seehaus, A. Wendt, M. H. Braun and K. Höppner (2018). "Recent dynamic changes on Fleming Glacier after the disintegration of Wordie Ice Shelf, Antarctic Peninsula." The Cryosphere **12**(4): 1-19.

Fürst, J. J., G. Durand, F. Gillet-Chaulet, N. Merino, L. Tavard, J. Mouginot, N. Gourmelen and O. Gagliardini (2015). "Assimilation of Antarctic velocity observations provides evidence for uncharted pinning points." The Cryosphere **9**(4): 1427-1443.

Furst, J. J., G. Durand, F. Gillet-Chaulet, L. Tavard, M. Rankl, M. Braun and O. Gagliardini (2016). "The safety band of Antarctic ice shelves." Nature Clim. Change **advance online publication**.

Gagliardini, O., F. Gillel-Chaulet and M. Montagnat (2009). "A Review of Anisotropic Polar Ice Models : from Crystal to Ice-Sheet Flow Models." Physics of Ice Core Records II, Institute of Low Temperature Science, Hokkaido University, Sapporo, 25 Japan.

Gagliardini, O., T. Zwinger, F. Gillet-Chaulet, G. Durand, L. Favier, B. de Fleurian, R. Greve, M. Malinen, C. Martín, P. Råback, J. Ruokolainen, M. Sacchettini, M. Schäfer, H. Seddik and J. Thies (2013). "Capabilities and performance of Elmer/Ice, a new-generation ice sheet model." Geosci. Model Dev. **6**(4): 1299-1318.

Gardner, A. S., G. Moholdt, T. Scambos, M. Fahnstock, S. Ligtenberg, M. van den Broeke and J. Nilsson (2017). "Increased West Antarctic ice discharge and East Antarctic stability over the last seven years." The Cryosphere Discuss. **2017**: 1-39.

Gardner, A. S., G. Moholdt, T. Scambos, M. Fahnstock, S. Ligtenberg, M. van den Broeke and J. Nilsson (2018). "Increased West Antarctic and unchanged East Antarctic ice discharge over the last 7 years." The Cryosphere **12**(2): 521-547.

Geuzaine, C. and J. F. Remacle (2009). "Gmsh: A 3 ‐ D finite element mesh generator with built ‐ in pre ‐ and post ‐ processing facilities." International Journal for Numerical Methods in Engineering **79**(11): 1309-1331.

Gillet-Chaulet, F., G. Durand, O. Gagliardini, C. Mosbeux, J. Mouginot, F. Rémy and C. Ritz (2016). "Assimilation of surface velocities acquired between 1996 and 2010 to constrain the form of the basal friction law under Pine Island Glacier." Geophysical Research Letters: n/a-n/a.

Gillet-Chaulet, F., O. Gagliardini, H. Seddik, M. Nodet, G. Durand, C. Ritz, T. Zwinger, R. Greve and D. G. Vaughan (2012). "Greenland ice sheet contribution to sea-level rise from a new-generation ice-sheet model." The Cryosphere **6**(6): 1561-1576.

Gladstone, R., M. Schäfer, T. Zwinger, Y. Gong, T. Strozzi, R. Mottram, F. Boberg and J. C. Moore (2014). "Importance of basal processes in simulations of a surging Svalbard outlet glacier." The Cryosphere **8**(4): 1393-1405.

Glen, J. W. (1955). The creep of polycrystalline ice. Proceedings of the Royal Society of London A: Mathematical, Physical and Engineering Sciences, The Royal Society.

Gong, Y., T. Zwinger, S. Cornford, R. Gladstone, M. Schäfer and J. C. Moore (2017). "Importance of basal boundary conditions in transient simulations: case study of a surging marine-terminating glacier on Austfonna, Svalbard." Journal of Glaciology **63**(237): 12.

Gudmundsson, G. H. (2013). "Ice-shelf buttressing and the stability of marine ice sheets." The Cryosphere **7**(2): 647-655.

Gudmundsson, G. H., J. Krug, G. Durand, L. Favier and O. Gagliardini (2012). "The stability of grounding lines on retrograde slopes." The Cryosphere **6**(6): 1497-1505.

Gunter, B. C., O. Didova, R. E. M. Riva, S. R. M. Ligtenberg, J. T. M. Lenaerts, M. A. King, M. R. Van den Broeke and T. Urban (2014). "Empirical estimation of present-day Antarctic glacial isostatic adjustment and ice mass change." The Cryosphere **8**(2): 743-760.

Hansen, P. C. (2001). "The L-curve and its use in the numerical treatment of

inverse problems." Computational inverse problems in electrocardiology **5**.

Harig, C. and F. J. Simons (2015). "Accelerated West Antarctic ice mass loss continues to outpace East Antarctic gains." Earth and Planetary Science Letters **415**(Supplement C): 134-141.

Hoffman, M. and S. Price (2014). "Feedbacks between coupled subglacial hydrology and glacier dynamics." Journal of Geophysical Research: Earth Surface **119**(3): 414-436.

Hoffman, M. J., G. A. Catania, T. A. Neumann, L. C. Andrews and J. A. Rumrill (2011). "Links between acceleration, melting, and supraglacial lake drainage of the western Greenland Ice Sheet." Journal of Geophysical Research: Earth Surface **116**(F4): n/a-n/a.

Hofton, M. A., J. B. Blair, S. B. Luthcke and D. L. Rabine (2008). "Assessing the performance of 20–25 m footprint waveform lidar data collected in ICESat data corridors in Greenland." Geophysical Research Letters **35**(24).

Hogg, A. E. and G. H. Gudmundsson (2017b). "Impacts of the Larsen-C Ice Shelf calving event." Nature Climate Change **7**: 540.

Hogg, A. E., A. Shepherd, S. L. Cornford, K. H. Briggs, N. Gourmelen, J. A. Graham, I. Joughin, J. Mouginot, T. Nagler, A. J. Payne, E. Rignot and J. Wuite (2017a). "Increased ice flow in Western Palmer Land linked to ocean melting." Geophysical Research Letters **44**(9): 4159-4167.

Holland, P. R., A. Jenkins and D. M. Holland (2010). "Ice and ocean processes in the Bellingshausen Sea, Antarctica." Journal of Geophysical Research: Oceans **115**(C5): n/a-n/a.

Iken, A. and R. A. Bindschadler (1986). "Combined measurements of Subglacial Water Pressure and Surface Velocity of Findelengletscher, Switzerland: Conclusions about Drainage System and Sliding Mechanism." Journal of Glaciology **32**(110): 101-119.

Ivins, E. R., T. S. James, J. Wahr, E. J. O. Schrama, F. W. Landerer and K. M. Simon (2013). "Antarctic contribution to sea level rise observed by GRACE with improved GIA correction." Journal of Geophysical Research: Solid Earth **118**(6): 3126-3141.

Ivins, E. R., C. A. Raymond and T. S. James (2000). "The influence of 5000 year-old and younger glacial mass variability on present-day crustal rebound in the Antarctic Peninsula." Earth, planets and space **52**(11): 1023-1029.

Ivins, E. R., M. M. Watkins, D.-N. Yuan, R. Dietrich, G. Casassa and A. Rülke (2011). "On-land ice loss and glacial isostatic adjustment at the Drake Passage: 2003–2009." Journal of Geophysical Research: Solid Earth **116**(B2).

Jenkins, A. (2011). "Convection-Driven Melting near the Grounding Lines of Ice Shelves and Tidewater Glaciers." Journal of Physical Oceanography **41**(12): 2279-2294.

Kaufmann, G., P. Wu and E. R. Ivins (2005). "Lateral viscosity variations beneath Antarctica and their implications on regional rebound motions and seismotectonics." Journal of Geodynamics **39**(2): 165-181.

King, M. A. (2013). "Progress in modelling and observing Antarctic glacial isostatic adjustment." Astronomy & Geophysics **54**(4): 4.33-34.38.

King, M. A., R. J. Bingham, P. Moore, P. L. Whitehouse, M. J. Bentley and G. A. Milne (2012). "Lower satellite-gravimetry estimates of Antarctic sea-level contribution." Nature **491**(7425): 586-589.

King, M. A. and A. Santamaría-Gómez (2016a). "Ongoing deformation of Antarctica following recent Great Earthquakes." Geophysical Research Letters **43**(5): 1918-1927.

King, M. A. and A. Santamaría-Gómez (2016a). "Ongoing deformation of Antarctica following recent Great Earthquakes." Geophysical Research Letters: n/a-n/a.

King, M. A., P. L. Whitehouse and W. van der Wal (2016b). "Incomplete separability of Antarctic plate rotation from glacial isostatic adjustment deformation within geodetic observations." Geophysical Journal International **204**(1): 324-330.

Kohler, J., T. A. Neumann, J. W. Robbins, S. Tronstad and G. Melland (2013). "ICESat Elevations in Antarctica Along the 2007–09 Norway–USA Traverse: Validation With Ground-Based GPS." IEEE Transactions on Geoscience and Remote Sensing **51**(3): 1578-1587.

Korona, J., E. Berthier, M. Bernard, F. Rémy and E. Thouvenot (2009). "SPIRIT. SPOT 5 stereoscopic survey of Polar Ice: Reference Images and Topographies during the fourth International Polar Year (2007–2009)." ISPRS Journal of Photogrammetry and Remote Sensing **64**(2): 204-212.

Krabill, W. B. (2014, updated 2016). "IceBridge ATM L2 Icessn Elevation, Slope, and Roughness. Version 2. ." NASA DAAC at the National Snow and Ice Data Center., Boulder, CO, USA.

Krabill, W. B., W. Abdalati, E. B. Frederick, S. S. Manizade, C. F. Martin, J. G. Sonntag, R. N. Swift, R. H. Thomas and J. G. Yungel (2002). "Aircraft laser altimetry measurement of elevation changes of the greenland ice sheet: technique and accuracy assessment." Journal of Geodynamics **34**(3–4): 357-376.

Krug, J., G. Durand, O. Gagliardini and J. Weiss (2015). "Modelling the impact of submarine frontal melting and ice malange on glacier dynamics." The Cryosphere **9**(3): 989-1003.

Lemoine, F. G., S. C. Kenyon, J. K. Factor, R. G. Trimmer, N. K. Pavlis, D. S. Chinn, C. M. Cox, S. M. Klosko, S. B. Luthcke and M. H. Torrence (1998). "The development of the joint NASA GSFC and the National Imagery and Mapping Agency (NIMA) geopotential model EGM96." NASA Goddard Space Flight Center, Greenbelt, Maryland, 20771 USA.

Li, X., D. M. Holland, E. P. Gerber and C. Yoo (2014). "Impacts of the north and tropical Atlantic Ocean on the Antarctic Peninsula and sea ice." Nature **505**: 538.

Ligtenberg, S. R. M., P. Kuipers Munneke and M. R. van den Broeke (2014). "Present and future variations in Antarctic firn air content." The Cryosphere **8**(5): 1711-1723.

Liu, Y., J. C. Moore, X. Cheng, R. M. Gladstone, J. N. Bassis, H. Liu, J. Wen and F. Hui (2015). "Ocean-driven thinning enhances iceberg calving and retreat of Antarctic ice shelves." Proceedings of the National Academy of Sciences: 201415137.

Ma, Y., O. Gagliardini, C. Ritz, F. Gillet-Chaulet, G. Durand and M. Montagnat (2010). "Enhancement factors for grounded ice and ice shelves inferred from an anisotropic ice-flow model." Journal of Glaciology **56**(199): 805-812.

MacAyeal, D. R. (1993). "A tutorial on the use of control methods in ice-sheet modeling." Journal of Glaciology **39**(131): 91-98.

Martín-Español, A., M. A. King, A. Zammit-Mangion, S. B. Andrews, P. Moore and J. L. Bamber (2016b). "An assessment of forward and inverse GIA solutions for Antarctica." Journal of Geophysical Research: Solid Earth **121**(9): 6947-6965.

Martín-Español, A., A. Zammit-Mangion, P. J. Clarke, T. Flament, V. Helm, M. A. King, S. B. Luthcke, E. Petrie, F. Rémy, N. Schön, B. Wouters and J. L. Bamber (2016a). "Spatial and temporal Antarctic Ice Sheet mass trends, glacio-isostatic adjustment, and surface processes from a joint inversion of satellite altimeter, gravity, and GPS data." Journal of Geophysical Research: Earth Surface **121**(2): 182-200.

McMillan, M., A. Shepherd, A. Sundal, K. Briggs, A. Muir, A. Ridout, A. Hogg and D. Wingham (2014). "Increased ice losses from Antarctica detected by CryoSat-2." Geophysical Research Letters **41**(11): 2014GL060111.

Mercer, J. H. (1978). "West Antarctic ice sheet and CO2 greenhouse effect: a threat of disaster." Nature **271**: 321.

Morlighem, M., E. Rignot, H. Seroussi, E. Larour, H. Ben Dhia and D. Aubry (2010). "Spatial patterns of basal drag inferred using control methods from a full -

Stokes and simpler models for Pine Island Glacier, West Antarctica." Geophysical Research Letters **37**(14).

Morlighem, M., E. Rignot, H. Seroussi, E. Larour, H. Ben Dhia and D. Aubry (2011). "A mass conservation approach for mapping glacier ice thickness." Geophysical Research Letters **38**(19): n/a-n/a.

Morlighem, M., H. Seroussi, E. Larour and E. Rignot (2013). "Inversion of basal friction in Antarctica using exact and incomplete adjoints of a higher-order model." Journal of Geophysical Research: Earth Surface **118**(3): 1746-1753.

Mouginot, J., E. Rignot and B. Scheuchl (2014). "Sustained increase in ice discharge from the Amundsen Sea Embayment, West Antarctica, from 1973 to 2013." Geophysical Research Letters **41**(5): 1576-1584.

Nield, G. A., V. R. Barletta, A. Bordoni, M. A. King, P. L. Whitehouse, P. J. Clarke, E. Domack, T. A. Scambos and E. Berthier (2014). "Rapid bedrock uplift in the Antarctic Peninsula explained by viscoelastic response to recent ice unloading." Earth and Planetary Science Letters **397**: 32-41.

Nield, G. A., P. L. Whitehouse, M. A. King, P. J. Clarke and M. J. Bentley (2012). "Increased ice loading in the Antarctic Peninsula since the 1850s and its effect on glacial isostatic adjustment." Geophysical Research Letters **39**(17).

Ó Cofaigh, C., B. J. Davies, S. J. Livingstone, J. A. Smith, J. S. Johnson, E. P. Hocking, D. A. Hodgson, J. B. Anderson, M. J. Bentley, M. Canals, E. Domack, J. A. Dowdeswell, J. Evans, N. F. Glasser, C.-D. Hillenbrand, R. D. Larter, S. J. Roberts and A. R. Simms (2014). "Reconstruction of ice-sheet changes in the Antarctic Peninsula since the Last Glacial Maximum." Quaternary Science Reviews **100**: 87-110.

Paolo, F. S., H. A. Fricker and L. Padman (2015). "Volume loss from Antarctic ice shelves is accelerating." Science.

Peltier, W. (2004). "Global glacial isostasy and the surface of the ice-age Earth: the ICE-5G (VM2) model and GRACE." Annu. Rev. Earth Planet. Sci. **32**: 111-149.

Peltier, W., D. Argus and R. Drummond (2015). "Space geodesy constrains ice age terminal deglaciation: The global ICE‐6G_C (VM5a) model." Journal of Geophysical Research: Solid Earth **120**(1): 450-487.

Petrov, L. (2015). "The international mass loading service." International Association of Geodesy Symposia **146**.

Pritchard, H., S. Ligtenberg, H. Fricker, D. Vaughan, M. Van den Broeke and L. Padman (2012). "Antarctic ice-sheet loss driven by basal melting of ice shelves." Nature **484**(7395): 502-505.

Pritchard, H. D., R. J. Arthern, D. G. Vaughan and L. A. Edwards (2009). "Extensive dynamic thinning on the margins of the Greenland and Antarctic ice sheets." Nature **461**(7266): 971-975.

Rack, W. and H. Rott (2004). "Pattern of retreat and disintegration of the Larsen B ice shelf, Antarctic Peninsula." Annals of Glaciology **39**: 505-510.

Reese, R., G. H. Gudmundsson, A. Levermann and R. Winkelmann (2017). "The far reach of ice-shelf thinning in Antarctica." Nature Climate Change **8**(1): 53-57.

Reynolds, J. M. (1988). "The structure of Wordie ice shelf, Antarctic peninsula." British Antarctic Survey Bulletin **80**: 57-64.

Rignot, E., J. L. Bamber, M. R. Van Den Broeke, C. Davis, Y. Li, W. J. Van De Berg and E. Van Meijgaard (2008). "Recent Antarctic ice mass loss from radar interferometry and regional climate modelling." Nature Geoscience **1**(2): 106-110.

Rignot, E., G. Casassa, P. Gogineni, W. Krabill, A. u. Rivera and R. Thomas (2004). "Accelerated ice discharge from the Antarctic Peninsula following the collapse of Larsen B ice shelf." Geophysical Research Letters **31**(18).

Rignot, E., G. Casassa, S. Gogineni, P. Kanagaratnam, W. Krabill, H. Pritchard, A. Rivera, R. Thomas, J. Turner and D. Vaughan (2005). "Recent ice loss from the Fleming and other glaciers, Wordie Bay, West Antarctic Peninsula." Geophysical Research Letters **32**(7).

Rignot, E., J. Mouginot, M. Morlighem, H. Seroussi and B. Scheuchl (2014). "Widespread, rapid grounding line retreat of Pine Island, Thwaites, Smith, and Kohler glaciers, West Antarctica, from 1992 to 2011." Geophysical Research Letters **41**(10): 3502-3509.

Rignot, E., J. Mouginot and B. Scheuchl (2011). "Ice Flow of the Antarctic Ice Sheet." Science **333**(6048): 1427-1430.

Rignot, E., J. Mouginot and B. Scheuchl (2011a). "Antarctic grounding line mapping from differential satellite radar interferometry." Geophysical Research Letters **38**(10): L10504.

Rignot, E., J. Mouginot and B. Scheuchl (2011b). "Ice Flow of the Antarctic Ice Sheet." Science **333**(6048): 1427-1430.

Rignot, E., J. Mouginot and B. Scheuchl (2011c). "MEaSUREs InSAR-Based Antarctica Ice Velocity Map [Version1.0]." Boulder, Colorado USA: NASA DAAC at the National Snow and Ice Data Center.

Riva, R. E. M., B. C. Gunter, T. J. Urban, B. L. A. Vermeersen, R. C. Lindenbergh, M. M. Helsen, J. L. Bamber, R. S. W. van de Wal, M. R. van den Broeke and B. E. Schutz (2009). "Glacial Isostatic Adjustment over Antarctica from combined ICESat and GRACE satellite data." Earth and Planetary Science Letters **288**(3–4): 516-523.

Robel, A. A. (2017). "Thinning sea ice weakens buttressing force of iceberg mélange and promotes calving." Nature Communications **8**: 14596.

Rott, H., P. Skvarca and T. Nagler (1996). "Rapid Collapse of Northern Larsen Ice Shelf, Antarctica." Science **271**(5250): 788-792.

Santamaría-Gómez, A. and A. Mémin (2015). "Geodetic secular velocity errors due to interannual surface loading deformation." Geophysical Journal International **202**(2): 763-767.

Sasgen, I., H. Konrad, E. R. Ivins, M. R. Van den Broeke, J. L. Bamber, Z. Martinec and V. Klemann (2013). "Antarctic ice-mass balance 2003 to 2012: regional reanalysis of GRACE satellite gravimetry measurements with improved estimate of glacial-isostatic adjustment based on GPS uplift rates." The Cryosphere **7**(5): 1499-1512.

Sasgen, I., A. Martín-Español, A. Horvath, V. Klemann, E. J. Petrie, B. Wouters, M. Horwath, R. Pail, J. L. Bamber, P. J. Clarke, H. Konrad and M. R. Drinkwater (2017). "Joint inversion estimate of regional glacial isostatic adjustment in Antarctica considering a lateral varying Earth structure (ESA STSE Project REGINA)." Geophysical Journal International **211**(3): 1534-1553.

Scambos, T., H. A. Fricker, C.-C. Liu, J. Bohlander, J. Fastook, A. Sargent, R. Massom and A.-M. Wu (2009). "Ice shelf disintegration by plate bending and hydro-fracture: Satellite observations and model results of the 2008 Wilkins ice shelf break-ups." Earth and Planetary Science Letters **280**(1): 51-60.

Scambos, T. A., E. Berthier, T. Haran, C. A. Shuman, A. J. Cook, S. R. M. Ligtenberg and J. Bohlander (2014). "Detailed ice loss pattern in the northern Antarctic Peninsula: widespread decline driven by ice front retreats." The Cryosphere **8**(6): 2135-2145.

Scambos, T. A., J. A. Bohlander, C. A. u. Shuman and P. Skvarca (2004). "Glacier acceleration and thinning after ice shelf collapse in the Larsen B embayment, Antarctica." Geophysical Research Letters **31**(18).

Scambos, T. A., C. Hulbe, M. Fahnestock and J. Bohlander (2000). "The link between climate warming and break-up of ice shelves in the Antarctic Peninsula." Journal of Glaciology **46**(154): 516-530.

Schäfer, M., F. Gillet-Chaulet, R. Gladstone, R. Pettersson, V. A. Pohjola, T. Strozzi and T. Zwinger (2014). "Assessment of heat sources on the control of fast flow of Vestfonna ice cap, Svalbard." The Cryosphere **8**(5): 1951-1973.

Schäfer, M., T. Zwinger, P. Christoffersen, F. Gillet-Chaulet, K. Laakso, R. Pettersson, V. A. Pohjola, T. Strozzi and J. C. Moore (2012). "Sensitivity of basal conditions in an inverse model: Vestfonna ice cap, Nordaustlandet/Svalbard." The Cryosphere **6**(4): 771-783.

Schannwell, C., N. E. Barrand and V. Radić (2016). "Future sea-level rise from tidewater and ice-shelf tributary glaciers of the Antarctic Peninsula." Earth and Planetary Science Letters **453**: 161-170.

Schmidtko, S., K. J. Heywood, A. F. Thompson and S. Aoki (2014). "Multidecadal warming of Antarctic waters." Science **346**(6214): 1227-1231.

Schoof, C. (2007). "Ice sheet grounding line dynamics: Steady states, stability, and hysteresis." Journal of Geophysical Research: Earth Surface **112**(F3): n/a-n/a.

Schoof, C. (2010). "Ice-sheet acceleration driven by melt supply variability." Nature **468**(7325): 803-806.

Schoof, C. (2012). "Marine ice sheet stability." Journal of Fluid Mechanics **698**: 62-72.

Seehaus, T. C., S. Marinsek, P. Skvarca, J. M. van Wessem, C. H. Reijmer, J. L. Seco and M. H. Braun (2016). "Dynamic Response of Sjögren Inlet Glaciers, Antarctic Peninsula, to Ice Shelf Breakup Derived from Multi-Mission Remote Sensing Time Series." Frontiers in Earth Science **4**(66).

Sergienko, O., T. T. Creyts and R. Hindmarsh (2014). "Similarity of organized patterns in driving and basal stresses of Antarctic and Greenland ice sheets

beneath extensive areas of basal sliding." Geophysical Research Letters **41**(11): 3925-3932.

Seroussi, H., M. Morlighem, E. Rignot, A. Khazendar, E. Larour and J. Mouginot (2013). Dependence of century-scale projections of the Greenland ice sheet on its thermal regime.

Shepherd, A., E. Ivins, E. Rignot, B. Smith, M. van den Broeke, I. Velicogna, P. Whitehouse, K. Briggs, I. Joughin, G. Krinner, S. Nowicki, T. Payne, T. Scambos, N. Schlegel, G. A, C. Agosta, A. Ahlstrøm, G. Babonis, V. Barletta, A. Blazquez, J. Bonin, B. Csatho, R. Cullather, D. Felikson, X. Fettweis, R. Forsberg, H. Gallee, A. Gardner, L. Gilbert, A. Groh, B. Gunter, E. Hanna, C. Harig, V. Helm, A. Horvath, M. Horwath, S. Khan, K. K. Kjeldsen, H. Konrad, P. Langen, B. Lecavalier, B. Loomis, S. Luthcke, M. McMillan, D. Melini, S. Mernild, Y. Mohajerani, P. Moore, J. Mouginot, G. Moyano, A. Muir, T. Nagler, G. Nield, J. Nilsson, B. Noel, I. Otosaka, M. E. Pattle, W. R. Peltier, N. Pie, R. Rietbroek, H. Rott, L. Sandberg-Sørensen, I. Sasgen, H. Save, B. Scheuchl, E. Schrama, L. Schröder, K.-W. Seo, S. Simonsen, T. Slater, G. Spada, T. Sutterley, M. Talpe, L. Tarasov, W. J. van de Berg, W. van der Wal, M. van Wessem, B. D. Vishwakarma, D. Wiese, B. Wouters and I. t. The (2018). "Mass balance of the Antarctic Ice Sheet from 1992 to 2017." Nature **558**(7709): 219-222.

Shepherd, A., E. R. Ivins, G. A, V. R. Barletta, M. J. Bentley, S. Bettadpur, K. H. Briggs, D. H. Bromwich, R. Forsberg, N. Galin, M. Horwath, S. Jacobs, I. Joughin, M. A. King, J. T. M. Lenaerts, J. Li, S. R. M. Ligtenberg, A. Luckman, S. B. Luthcke, M. McMillan, R. Meister, G. Milne, J. Mouginot, A. Muir, J. P. Nicolas, J. Paden, A. J. Payne, H. Pritchard, E. Rignot, H. Rott, L. S. Sørensen, T. A. Scambos, B. Scheuchl, E. J. O. Schrama, B. Smith, A. V. Sundal, J. H. van Angelen, W. J. van de Berg, M. R. van den Broeke, D. G. Vaughan, I. Velicogna, J. Wahr, P. L. Whitehouse, D. J. Wingham, D. Yi, D. Young and H. J. Zwally (2012). "A Reconciled Estimate of Ice-Sheet Mass Balance." Science **338**(6111): 1183-1189.

Shepherd, A., D. Wingham, T. Payne and P. Skvarca (2003). "Larsen ice shelf has progressively thinned." Science **302**(5646): 856-859.

Shreve, R. (1972). "Movement of water in glaciers." Journal of Glaciology **11**(62): 205-214.

Simkins, L. M., A. R. Simms and R. DeWitt (2013). "Relative sea-level history of Marguerite Bay, Antarctic Peninsula derived from optically stimulated luminescence-dated beach cobbles." Quaternary Science Reviews **77**: 141-155.

Steiger, N., K. H. Nisancioglu, H. Åkesson, B. de Fleurian and F. M. Nick (2017). "Non-linear retreat of Jakobshavn Isbræ since the Little Ice Age controlled by geometry." The Cryosphere Discuss. **2017**: 1-27.

Sutterley, T. C., I. Velicogna, E. Rignot, J. Mouginot, T. Flament, M. R. van den Broeke, J. M. van Wessem and C. H. Reijmer (2014). "Mass loss of the Amundsen Sea Embayment of West Antarctica from four independent techniques." Geophysical Research Letters **41**(23): 8421-8428.

Tapley, B. D., S. Bettadpur, J. C. Ries, P. F. Thompson and M. M. Watkins (2004). "GRACE measurements of mass variability in the Earth system." Science **305**(5683): 503-505.

Thomas, E. R., G. J. Marshall and J. R. McConnell (2008). "A doubling in snow accumulation in the western Antarctic Peninsula since 1850." Geophysical research letters **35**(1).

Thomas, I. D., M. A. King, M. J. Bentley, P. L. Whitehouse, N. T. Penna, S. D. Williams, R. E. Riva, D. A. Lavallee, P. J. Clarke and E. C. King (2011). "Widespread low rates of Antarctic glacial isostatic adjustment revealed by GPS observations." Geophysical Research Letters **38**(22).

Thomas, I. D., M. A. King, M. J. Bentley, P. L. Whitehouse, N. T. Penna, S. D. P. Williams, R. E. M. Riva, D. A. Lavallee, P. J. Clarke and E. C. King (2011). "Widespread low rates of Antarctic glacial isostatic adjustment revealed by GPS observations." Geophysical Research Letters **38**(22).

Thomas, R. H. and C. R. Bentley (1978). "A model for Holocene retreat of the West Antarctic Ice Sheet." Quaternary Research **10**(2): 150-170.

Todd, J. and P. Christoffersen (2014). "Are seasonal calving dynamics forced by buttressing from ice mélange or undercutting by melting? Outcomes from full-Stokes simulations of Store Glacier, West Greenland." The Cryosphere **8**(6): 2353-2365.

Turner, J., S. R. Colwell, G. J. Marshall, T. A. Lachlan‐Cope, A. M. Carleton, P. D. Jones, V. Lagun, P. A. Reid and S. Iagovkina (2005). "Antarctic climate change during the last 50 years." International journal of Climatology **25**(3): 279-294.

Turner, J., H. Lu, I. White, J. C. King, T. Phillips, J. S. Hosking, T. J. Bracegirdle, G. J. Marshall, R. Mulvaney and P. Deb (2016). "Absence of 21st century warming on Antarctic Peninsula consistent with natural variability." Nature **535**: 411.

Turner, J., A. Orr, G. H. Gudmundsson, A. Jenkins, R. G. Bingham, C.-D. Hillenbrand and T. J. Bracegirdle (2017). "Atmosphere-ocean-ice interactions in the Amundsen Sea Embayment, West Antarctica." Reviews of Geophysics **55**(1): 235-276.

Ullman, S. (1979). "The Interpretation of Structure from Motion." Proceedings of the Royal Society of London. Series B. Biological Sciences **203**(1153): 405-426.

van der Wal, W., P. L. Whitehouse and E. J. O. Schrama (2015). "Effect of GIA models with 3D composite mantle viscosity on GRACE mass balance estimates for Antarctica." Earth and Planetary Science Letters **414**: 134-143.

van Wessem, J. M., C. H. Reijmer, J. T. M. Lenaerts, W. J. van de Berg, M. R. van den Broeke and E. van Meijgaard (2014). "Updated cloud physics in a regional atmospheric climate model improves the modelled surface energy balance of Antarctica." The Cryosphere **8**(1): 125-135.

van Wessem, J. M., S. R. M. Ligtenberg, C. H. Reijmer, W. J. van de Berg, M. R. van den Broeke, N. E. Barrand, E. R. Thomas, J. Turner, J. Wuite, T. A. Scambos and E. van Meijgaard (2016). "The modelled surface mass balance of the Antarctic Peninsula at 5.5 km horizontal resolution." The Cryosphere **10**(1): 271-285.

Vaughan, D. G. (1993). "Implications of the break-up of Wordie Ice Shelf, Antarctica for sea level." Antarctic Science **5**(04): 403-408.

Vaughan, D. G. and R. Arthern (2007). "Why Is It Hard to Predict the Future of Ice Sheets?" Science **315**(5818): 1503-1504.

Vaughan, D. G. and C. S. M. Doake (1996). "Recent atmospheric warming and retreat of ice shelves on the Antarctic Peninsula."

Vaughan, D. G., G. J. Marshall, W. M. Connolley, J. C. King and R. Mulvaney (2001). "Devil in the detail." Science-new york then washington-: 1777-1778.

Velicogna, I. and J. Wahr (2006). "Acceleration of Greenland ice mass loss in spring 2004." Nature **443**(7109): 329-331.

Verhoeven, G. (2011). "Taking computer vision aloft – archaeological three-dimensional reconstructions from aerial photographs with photoscan." Archaeological Prospection **18**(1): 67-73.

Walker, C. C. and A. S. Gardner (2017). "Rapid drawdown of Antarctica's Wordie Ice Shelf glaciers in response to ENSO/Southern Annular Mode-driven warming in the Southern Ocean." Earth and Planetary Science Letters **476**(Supplement C): 100-110.

Walter, J. I., J. E. Box, S. Tulaczyk, E. E. Brodsky, I. M. Howat, Y. Ahn and A. Brown (2017). "Oceanic mechanical forcing of a marine-terminating Greenland glacier." Annals of Glaciology **53**(60): 181-192.

Weertman, J. (1974). "Stability of the Junction of an Ice Sheet and an Ice Shelf." Journal of Glaciology **13**(67): 3-11.

Wendt, J., A. Rivera, A. Wendt, F. Bown, R. Zamora, G. Casassa and C. Bravo (2010). "Recent ice-surface-elevation changes of Fleming Glacier in response to the removal of the Wordie Ice Shelf, Antarctic Peninsula." Annals of Glaciology **51**(55): 97-102.

Whitehouse, P. (2009). "Glacial isostatic adjustment and sea-level change." State of the art report.

Whitehouse, P. L., M. J. Bentley and A. M. Le Brocq (2012b). "A deglacial model for Antarctica: geological constraints and glaciological modelling as a basis for a new model of Antarctic glacial isostatic adjustment." Quaternary Science Reviews **32**: 1-24.

Whitehouse, P. L., M. J. Bentley, G. A. Milne, M. A. King and I. D. Thomas (2012a). "A new glacial isostatic adjustment model for Antarctica: calibrated and tested using observations of relative sea-level change and present-day uplift rates." Geophysical Journal International **190**(3): 1464-1482.

Williams, S. D. P. (2008). "CATS: GPS coordinate time series analysis software." GPS Solutions **12**(2): 147-153.

Wolstencroft, M., M. A. King, P. Whitehouse, M. J. Bentley, G. A. Nield, E. C. King, M. McMillan, A. Shepherd, V. R. Barletta, A. Bordoni, R. E. M. Riva, O. Didova and B. C. Gunter (2015). "Uplift rates from a new high-density GPS network in Palmer Land indicate significant late Holocene ice loss in the south-western Weddell Sea." Geophysical Journal International.

Wolstencroft, M., M. A. King, P. L. Whitehouse, M. J. Bentley, G. A. Nield, E. C. King, M. McMillan, A. Shepherd, V. Barletta, A. Bordoni, R. E. M. Riva, O. Didova and B. C. Gunter (2015). "Uplift rates from a new high-density GPS network in Palmer Land indicate significant late Holocene ice loss in the southwestern Weddell Sea." Geophysical Journal International **203**(1): 737-754.

Wouters, B., A. Martin-Español, V. Helm, T. Flament, J. M. van Wessem, S. R. M. Ligtenberg, M. R. van den Broeke and J. L. Bamber (2015). "Dynamic thinning of glaciers on the Southern Antarctic Peninsula." Science **348**(6237): 899-903.

Zhao, C., R. M. Gladstone, R. C. Warner, M. A. King, T. Zwinger and M. Morlighem (2018). "Basal friction of Fleming Glacier, Antarctica - Part 1: Sensitivity of inversion to temperature and bedrock uncertainty." The Cryosphere **12**(8): 2637-2652.

Zhao, C., R. M. Gladstone, R. C. Warner, M. A. King, T. Zwinger and M. Morlighem (2018). "Basal friction of Fleming Glacier, Antarctica - Part 2: Evolution from 2008 to 2015." The Cryosphere **12**(8): 2653-2666.

Zhao, C., M. A. King, C. S. Watson, V. R. Barletta, A. Bordoni, M. Dell and P. L. Whitehouse (2017). "Rapid ice unloading in the Fleming Glacier region, southern Antarctic Peninsula, and its effect on bedrock uplift rates." Earth and Planetary Science Letters **473**: 164-176.

Zwally, H., R. SCHUTZ, C. BENTLEY, J. BUFTON, T. HERRING, J. MINSTER, J. SPINHIRNE and R. THOMAS (2014). GLAS/ICESat L2 Antarctic and Greenland Ice Sheet Altimetry Data Version 34. Boulder, Colorado USA. , NASA National Snow and Ice Data Center Distributed Active Archive Center.